The Role of Cellular Architecture in Vascular Smooth Muscle Function and Mechanics

A DISSERTATION

SUBMITTED TO THE FACULTY OF

UNIVERSITY OF MINNESOTA

BY

Zaw Win

IN PARTIAL FULFILLMENT OF THE REQUIREMENTS

FOR THE DEGREE OF

DOCTOR OF PHILOSOPHY

Dr. Patrick W. Alford, Advisor

August 2017

Acknowledgements

While this work encompasses the last six years of my life, it would not have been possible without the support from my family, friends, colleagues, and acquaintances throughout my life that has led to this point. I will have fond memories of the University of Florida, University of Minnesota, and Minneapolis.

First, I want to thank my advisor, Dr. Patrick Alford. I could not have asked for a more understanding and supportive advisor. I am truly grateful to have been your student. There is no doubt your training and guidance have been and will continue to be instrumental to my success during my graduate studies and my future career. Thank you for your leadership and mentorship for the last six years. I also want to thank my thesis committee members for providing guidance over the years: Dr. Victor Barocas, Dr. GW Gant Luxton, and Dr. Paolo Provenzano. It was a pleasure collaborating with you all and this thesis is better from your efforts.

I would like to thank my lab family: Eric, Kerianne, and Nick. I consider you friends first and co-workers second. Part of the fun of working in the lab was getting to know each of you over the years and the many conversations we had on Friday afternoons. Eric: you are one of the kindest people I know and I look up to your character in my personal and professional life. Kerianne: we joined and leave the lab together, we've sat back to back for the past six years, our bond is something that will never be repeated. Nick: Be humble and bless up. I also want to thank the students I have had the pleasure of mentoring over the years, particularly Emily Sevcik and Justin Buksa. I learned as much working with you and helping you with your projects.

I would also thank my mentors from the University of Florida, Dr. Dinesh Shah and Dr. Tanmay Lele. My path to graduate school started under both your mentorship. I was first introduced to the field of mechanobiology through Dr. Lele's class and working with David in the lab the summer before my last year

cemented my passion and interest in the field which led to me deciding to pursue it for graduate school. I will cherish the times I spent with Paul and Dr. Shah in your home and the conversations we had over many dinners.

I would like to thank all my classmates for sharing this journey with each other: Avijit, Ben, Bryan, Cory, David, Katia, Katie, Kerianne, Jeremy, Laura, Pantea, Simeng, Stephen, and Yizi. I should also thank my friends who have influenced me in my life and shared memories during this stage in my life: Abigail, Alex, Clay, Gan, Kathryn, Kirsten, Madalyn, Mitchell, Ted, Lucy, Jolene, Nancy, Supriya, Ted, Xinran, and Viann.

Finally, my family including my sister, mom, dad, and grandparents have made me the person I am and thank you for all of your support and love. Without all your hard work and sacrifices, I would not be where I am today.

Abstract

Recently, there has been a push towards clinical translation of biomechanical models of tissues by developing patient-specific models to predict disease outcomes. To accomplish this, it is necessary to understand the functional and mechanical properties of all the tissue components, including individual cells. In vasculature, tissues and cells have different structures based on their functional role. The principle goal of this work is to determine how cellular architecture influences function and mechanical properties. To test our hypotheses, we have developed *in vitro* models to study the relationship between structure and function at the tissue and cellular scale.

We have developed microfluidic capture array device (MCAD) technology to study cell structure and function in 2D engineered vascular smooth muscle tissue and have developed cellular micro-biaxial stretching (CμBS) microscopy to determine single cell mechanical properties. First, using MCAD technology we were able to vary initial cell-cell contact during seeding to bias the cellular architecture in confluent vascular smooth muscle tissues. We found that tissues seeded using initially higher cell–cell contact conditions yielded tissues with more elongated cellular architecture which lead to greater contractile function in engineered tissues.

We then used CμBS microscopy to determine the elastic anisotropic mechanical properties of individual cells, given by the strain energy density (SED) function. We found that smooth muscle cells (VSMCs) with native-like architectures are highly anisotropic and can be described by a SED based on the actin cytoskeletal organization. Then, we utilized CμBS microscopy to characterize loading and unloading mechanics of VSMCs. We found that VSMCs exhibit architecture-dependent anisotropic hysteresis where highly structured VSMCs exhibit typical hysteresis associated with viscous loss when stretched in the direction of actin fiber alignment but exhibit reverse hysteresis when stretched in the direction orthogonal to actin fiber alignment. We then modeled

the observed hysteresis using two models: a quasi-linear (QLV) model and a Hill-type active fiber model and found that the QLV model was insufficient to characterize the anisotropic hysteresis but the Hill-type active fiber model was able to predict the anisotropic hysteresis in highly-organized VSMCs.

Table of Contents

List of Figures

Chapter 2

Chapter 3

Chapter 4

List of Tables

Chapter 1. Introduction

Advances in 3D imaging techniques (1, 2) and the rise of computing power have allowed researchers to develop patient-specific models of cardiovascular mechanics (3, 4). Currently, disease progression in aortic and cerebral aneurysms are tracked simply by measuring a parameter such as aneurysm diameter (5). However, advances in non-invasive 3D imaging have improved disease progression tracking by incorporating the 3D geometry of the aneurysm and finite element method (FEM) to create models of the aneurysm. Some current models use a rule-of-mixtures model that incorporates the components of tissues, including stress generating cells and remodeling extracellular matrix (ECM) components, to predict growth and remodeling of vascular tissue (6, 7). Thus, it is important to know the functional and mechanical properties of each component of tissues. Mechanical properties of the ECM component of vascular tissues such as elastin or collagen have been well studied (8, 9) but the current understanding of the cellular component is limited to linear estimations. Since tissues and cells undergo large strains in vasculature, we must be able to determine the large strain mechanical properties of vascular smooth muscle cells to accurately model vascular growth and remodeling. Our work will advance the current understanding of the role of cell architecture on the functional and mechanical properties of vascular smooth muscle and improve models of vascular growth and remodeling.

1.1 Tissue and cellular architecture affects function

In vivo tissues have finely controlled hierarchical structure that is often difficult to mimic *in vitro*. Microfabrication techniques, such as microcontact printing (10), can be used to reproduce tissue structure *in vitro* by controlling cell shape and orientation. Several recent results suggest that cellular organization and structure can influence tissue function in engineered tissues (11-13). For example, using microcontact printing and muscular thin film technology, Alford et al. has shown that engineered vascular tissues whose smooth muscle cells

possessed more elongated spindle-like geometries, similar to *in vivo* structure (14), exhibited more physiological contraction function. Aside from cell shape, cell-cell coupling also plays a significant role in functional contractility. In engineered cardiac microtissues, cooperative coupling of focal adhesions and cell-cell junctions at the cell-cell interface is necessary to regulate efficient force generation (13). These studies suggest that not only cellular geometry, but cell-cell organization, within a tissue is important to reproduce in engineered tissues to mimic *in vivo* function. In recent years, many researchers have studied how cells receive mechanical cues from the environment and convert them into chemical stimuli and thus change their behavior, a process known as mechanotransduction (15). Many components of the cell and ECM across multiple scales have been shown to mediate this process. Researchers have shown using micropatterning that by simply changing the shape of the cell on a 2D substrate where the cell-ECM adhesion process is confined, the fate of the cell can be changed (16-18). Thus, it is important to understand the role of cellular architecture in tissue function. Towards studying this, we have developed a microfluidic capture array device (MCAD) to bias initial cell-cell contact in 2D engineered vascular tissues. Using MCAD seeded tissues, we generated tissues of varying cellular architecture. Muscular thin film (MTF) assay and protein expression were used to investigate the tissues' functional properties. These results are summarized in Chapter 2.

1.2 Current methods of measuring cell mechanical properties and evaluation of cell generated traction force

Cells consist of a cellular membrane, cytoskeleton, nucleus, and numerous organelles (19). Thus, they are highly anisotropic and inhomogeneous. Researchers have studied the mechanical properties of single cells by using methods such as micropipette aspiration (20), magnetic twisting cytometry (21, 22), atomic force microscopy (AFM) (23, 24), and more to determine Young's modulus of a cell. However, these methods are limited in that they estimate linear mechanical properties at small strains and do not capture the anisotropy of a cell.

For example, micropipette aspiration (25) uses a micropipette that is placed near the cell membrane to apply a small vacuum and measure the deformation of the cell membrane. This technique is limited to the cell membrane-air interface and does not capture the mechanical properties of the entire cell. Magnetic twisting cytometry utilizes a ligand-coated magnetic bead that is allowed to attach to cell membrane receptors. A magnetic field is then applied to twist the bead to obtain the storage and loss modulus. This method is limited to the cell membrane-bead interface (26). Researchers have also used AFM to indent individual cells (23) and cell nuclei (27) to probe cell mechanics. By measuring the vertical deflection of the cantilever, Young's modulus can be calculated. However, because cells are highly inhomogeneous, the site of indentation can affect results (28) where the cytoskeleton and cell nuclei are much stiffer than the bulk cytosol and cell membrane. We propose to characterize the mechanical properties of a cell using continuum methods that can capture the anisotropy of a cell. One way researchers have characterized the mechanical properties of tissue is by using biaxial testing. Biaxial testing is the gold standard for nonlinear anisotropic mechanical property measurement (29). In general, soft tissues are mounted to a biaxial device in a trampoline like fashion using sutures or by using a system of clamps. (30) The samples are then strained uniaxially and biaxially. By performing a set of biaxial tests on a tissue sample, one can determine the response of the tissue to mechanical load and develop constitutive models that can predict the mechanical behavior of a tissue under loading. Unfortunately, it is much more technically challenging to perform biaxial testing on a very small sample such as a single cell. A modified technique where biaxial stretching is applied to a cell could yield more useful properties than the methods currently used by researchers (26).

When cells are placed on a 2D substrate such as cell culture polystyrene plastic or glass dishes, they exert a traction force on the surface through integrin-mediated adhesions (31). This mechanical interaction is involved in regulating cell shape and cell migration. Harris et al. studied the traction forces exerted by

chick heart fibroblasts by culturing them on a thin elastic silicon substrate (32). They saw wrinkling of the substrate at the cell-substrate interface. Wang et al. (33) and others have extended the concept of using soft substrates (E = 6.2 kPa) to observe cellular traction by culturing cells on thin polyacrylamide gels doped with fluorescent microbeads. The authors calculated the traction forces exerted by the cell using mechanical properties of the substrate and observing the deformation of the beads at the gel surface. Swiss 3T3 fibroblasts were shown to exert an average traction of 2 kPa over the projected area of the cell and upwards to 10 kPa at the leading edges of the cell. The advantage of this traction force microscopy technique is that it provides spatial and temporal tracking of cell traction and can be applied to calculate traction forces in migrating cells (34, 35).

We combined traditional biaxial stretching and traction force microscopy approaches to develop a cellular micro-biaxial stretching (CμBS) method to determine the mechanical properties of individual VSMCs. First, in Chapter 3, we characterized the elastic mechanical properties of VSMCs and showed that *in vivo*-like VSMCs have anisotropic material properties. We then developed a constitutive relation based on the actin fiber distribution in the cell that was able to predict the effect of cell architecture on the mechanical properties. Lastly, in Chapter 4, we investigated loading and unloading dynamics of individual VSMCs. We found that VSMCs exhibit hysteresis, dependent on stretch direction and cytoskeletal architecture. We modeled the observed hysteresis using a passive relaxation quasi-linear viscoelasticity model and an actively adapting Hill-type active fiber model.

Chapter 2. Smooth muscle architecture within cell-dense vascular tissues influences functional contractility

This chapter contains material published in Integrative Biology and is reproduced with permission. Win Z, Vrla GD, Steucke KE, Sevcik EN, and Alford PW (2014) Smooth muscle architecture within cell-dense vascular tissues influences functional contractility.

Reproduced from Ref. (36) with permission from the Royal Society of Chemistry.

2.1 Summary

The role of vascular smooth muscle architecture in the function of healthy and dysfunctional vessels is poorly understood. We aimed at determining the relationship between vascular smooth muscle architecture and contractile output using engineered vascular tissues. We utilized microcontact printing and a microfluidic cell seeding technique to provide three different initial seeding conditions, with the aim of influencing the cellular architecture within the tissue. Cells seeded in each condition formed confluent and aligned tissues but within the tissues, the cellular architecture varied. Tissues with a more elongated cellular architecture had significantly elevated basal stress and produced more contractile stress in response to endothelin-1 stimulation. We also found a correlation between the contractile phenotype marker expression and the cellular architecture, contrary to our previous findings in non-confluent tissues. Taken with previous results, these data suggest that within cell-dense vascular tissues, smooth muscle contractility is strongly influenced by cell and tissue architectures.

2.2 Introduction

Vascular smooth muscle cells (VSMCs) are the most numerous cells in arteries and primarily function to maintain vascular tone. VSMC architecture varies with the vessel according to the required function. In smaller muscular arteries, which dynamically contract and relax in response to endothelial (37) and mechanical

stimulation (38), VSMCs have a distinct elongated spindle shape (14). In contrast, VSMCs in elastic arteries such as the aorta, whose primary function is maintenance of vessel pressure, do not have as pronounced a spindle shape. Additionally, vessels with complex geometries can contain VSMCs of varying architecture. For example, bifurcations of small muscular arteries like those in the Circle of Willis contain several non-spindle cells at the apex (39). These regions with mixed cell architecture are notable because cerebral saccular aneurysms predominantly occur in these locations(40-42). To date, it has been unclear exactly how VSMC function depends on the structure in healthy and dysfunctional vessels.

VSMCs exhibit phenotypic plasticity, transitioning between two phenotypes: contractile and synthetic (43, 44). In healthy muscular arteries, contractile VSMCs display an elongated architecture as well as an increased contractile protein expression. In response to vascular injury or disease, VSMCs switch to a synthetic phenotype to better repair the injury by increasing extracellular matrix (ECM) production, proliferation and migration (45, 46). VSMC phenotype is normally measured by the expression of contractile protein markers, which are assumed to indicate contractile function (47). However, in our previous studies we found that VSMC function is not always correlated with phenotype expression (11).

We and others have shown, using micropatterning approaches, that regulating the cell architecture can affect a number of cell functions and phenotype (16-18, 48). We have previously shown that engineered *in vitro* vascular tissues exhibited greater contraction force per unit cross-sectional area when VSMCs were forced into exaggerated spindle shapes compared to those with smaller aspect ratios. In that study (11), we controlled the VSMC architecture by using microcontact printing to construct muscle fibrils with varying widths. However, VSMCs *in vivo* exist as concentric confluent lamellar sheets, not fibrils (49, 50). Moreover, it has been shown that the VSMC phenotype is affected by the number of cell–cell contacts (51, 52). Thus, we aimed at developing a method for controlling the microscale VSMC structure within a confluent tissue that mimics a concentric confluent lamellar sheet of an artery.

Many studies have shown that contact guidance imposed by physical constraints of a cell's environment can influence its architecture (53-55). Additionally, initial cell–cell contacts can play an important role in eventual tissue self-organization and phenotype (56-58), suggesting that initial conditions during cell seeding can be used to influence the VSMC architecture within a tissue. There are a number of methods to precisely place the individual cells using microfluidic devices including microwells (59), flow-focusing (60), and hydrodynamic capture in traps (61, 62). Researchers have used these microfluidic methods to capture single cells or clusters of cells for high-throughput single cell analysis (63) and to study biological processes such as cell fusion (64), cellular metabolism (65), and cellular toxicity (66, 67). To date, cell placement has not been used to control cell architecture within a tissue.

We hypothesized that VSMC structure affects vascular tissue contractility in the absence of constraining boundary conditions. To study this hypothesis, we designed a microfluidic capture array device (MCAD) that allows us to control the initial placement of cells and provide guidance cues for cellular organization in engineered tissues. We used this new technology combined with micropatterning techniques to fabricate 2D engineered tissues that mimic the simplest subunit of vascular smooth muscle, a confluent lamella of aligned VSMCs, where the cellular architecture within the tissues was modulated using initial seeding conditions. Using muscular thin film (MTF) technology, we find that there is a correlation between contraction and cellular architecture in engineered tissues.

2.3 Results

2.3.1 Controlling the tissue architecture using initial conditions

Previous studies have used boundary conditions to control the cell architecture by confining VSMCs in strips of various widths to change the tissue level structure (11) or by patterning single cells (68). Here, we aimed at controlling the individual VSMC architecture within a confluent monolayer using initial

conditions. We developed a new method of fabricating engineered confluent vascular tissues using initial seeding conditions to control the tissue structure. We reasoned that by keeping the mesoscale density constant, but changing the microscale density of seeding, we could utilize cell–cell contact guidance, in combination with ECM patterning, to vary cellular organization within our tissues.

To change the seeding conditions, we designed MCADs with vertical pillars protruding from the ceiling of the device, designed to trap cells in specific locations (Fig. 2.1A). The features have a height of 37 μm to trap a single layer of cells. When a cell suspension is flowed through the device, the cells follow the streamlines through and around the features until cells are trapped in the device features (Fig. 2.1B). When the trap is full, additional cells cannot be trapped as the streamlines circumvent the filled traps. This allowed us to specify the precise location of each cell. We designed three MCADs with varied trap depth to bias the cell–cell contact: 15, 100, and 200 μm (Fig. 2.1C). The trap depth dictated the initial cell–cell contact during seeding where the 15 μm traps were designed to trap a single cell with no initial lateral contacts with other cells while the 100 and 200 μm traps were designed to trap multiple cells with one or more initial lateral contacts with other cells. VSMCs were flowed through the device until the majority of the traps were filled. The devices were then incubated for 45 min to allow the cells to attach. The devices were peeled away and tissues self-organized along the direction of the micropattern for 12–24 h in growth medium yielding mesoscopically identical confluent monolayers (Fig. 2.1C).

Tissues were stained for F-actin and nuclei (Fig. 2.2A). F-actin coverage was used to determine the tissue confluence, which was found to be consistent in all tissues. F-actin coverage was approximately 70–80% (Fig. 2.2B), which is within the range of confluent tissues as reported in previous studies (11, 18, 69). The overall seeding density quantified by measuring nuclei per area indicated that tissues were of similar density (non-device: 26 560 ± 3623 nuclei per cm^2; 15 μm: 22 091 ± 702 nuclei per cm^2; 100 μm: 27 074 ± 1673 nuclei per cm^2; 200 μm: 27 788 ± 5127 nuclei per cm^2). Deconvolved stacks of F-actin were used to

construct 3D volumes of tissues. All tissues were found to be consistent in thickness (non-device: 3.84 ± 0.31 μm; 15 μm: 3.51 ± 0.30 μm; 100 μm: 3.41 ± 0.22 μm; 200 μm: 3.69 ± 0.58 μm). Actin fiber and nuclear orientations were characterized by an orientational order parameter (OOP). Actin fiber OOP was over 0.9 for all tissues (Fig. 2.2C) and nuclear orientation was above 0.85 (Fig. 2.2D), demonstrating that the tissues were aligned with consistent actin and nuclear orientations in all tissues. We and others have previously shown that nuclear eccentricity is indicative of cellular shape in VSMCs and other cells (11, 69). Thus, we measured nuclear eccentricity in the tissues constructed using each MCAD and found that eccentricity was elevated in all devices compared to non-device samples, and in the 200 μm MCAD compared to the 15 & 100 μm devices (Fig. 2.2E). The data suggest that our MCAD method for cell organization during seeding allows control of cell architecture within a confluent tissue.

2.3.2 Initial seeding conditions affect the sub-cellular vascular tissue architecture

We asked whether the differences seen in the sub-cellular architecture were due to the cell–cell contact guidance caused by the initial spatial distribution. We reasoned that by changing the microscale density of cells during initial seeding, and thus the density of cell–cell contact, cells would elongate more along the direction of the micropattern due to lateral constraints provided by cells transverse to tissue alignment. We analyzed the distribution of lateral cell constraints in the tissue constructs and their respective cellular shape measured by the aspect ratio immediately after the devices were removed (45 min post-seeding). Cells of interest are outlined in yellow and cells that are in lateral contact are outlined in red (Fig. 2.3A). We found that the cell aspect ratio correlated with the number of lateral cell constraints where cells with one or more lateral constraints had a higher aspect ratio compared to cells with zero lateral constraints (Fig. 2.3B), demonstrating that cells with more lateral constraints were more elongated. The percentage of cells with multiple lateral constraints increased with the depth of the traps. We found the most

one or two cell constraints in the 100 μm and 200 μm MCADs (Fig. 2.3C) and the least one or two cell constraints in the 15 μm MCADs (Fig. 2.3C) as expected from the mesoscale structure of the traps. Additionally, we found that the cellular aspect ratio was higher in the tissues seeded using the 100 μm and 200 μm devices compared to the non-device samples and the 15 μm device (Fig. 2.3D). We found a positive correlation between the cellular aspect ratio in the seeded substrates with nuclear eccentricity in the confluent tissues (Fig. 2.3E), which suggests that the initial seeding condition provided by contact guidance due to lateral cell constraints in the traps leads to differences in the cellular architecture in engineered tissues.

2.3.3 Sub-cellular tissue architecture affects functional contractile output

To determine whether the cellular architecture influences functional output in VSMCs, we utilized a MTF assay to measure contractile stress generation in the tissues constructed with each seeding method. The MTF consists of a two-layer thin beam composed of an active cell layer and a passive PDMS layer (Fig. 2.4A) spincoated on a layer of a thermosensitive polymer PIPAAm. When the construct is cooled briefly below 32 °C, PIPAAm dissolves, releasing the PDMS and cell layers. The stress generated by the cell layer causes bending of the two-layer beam which results in a measurable change in the curvature of the beam (Fig. 2.4B) which was used to calculate tissue stress. We stimulated the tissues with vasoconstrictor endothelin-1 (ET-1, 50 nM) to induce contraction, followed by rho-kinase inhibitor HA-1077 (100 μM) to inhibit contraction (Fig. 2.4C). This protocol yielded two important stresses: the basal tone, which is a measure of the baseline contractile stress of the tissue, and the induced contraction, which is a measure of the additional stress generated following ET-1 stimulation. All stress measurements were normalized to the average non-device tissue. We found that both induced contraction and basal tone were increased nearly two-fold in tissues constructed using the 100 and 200 μm MCADs compared to non-device tissues and 15 μm MCAD tissues (Fig. 2.4D,E). We next asked whether the cellular architecture in the tissues correlated with tissue function. We determined the correlation between

nuclear eccentricity and contractile stress and found a non-significant positive trend for induced contraction with nuclear eccentricity (Fig. 2.4F) and a similar non-significant positive trend for basal tone with nuclear eccentricity (Fig. 2.4G).

2.3.4 Tissue structure and phenotype expression

We asked whether the differences in contraction were due to changes in the VSMC phenotype. We determined the protein expression of contractile phenotype markers smoothelin and smooth muscle-myosin heavy chain (SMMHC) (Fig. 2.5A). While an apparent trend appears, we found that there were no statistically significant differences in the expression of either marker for the MCAD seeding compared to non-device tissues (Fig. 2.5B). However, we correlated contractile protein expression with contractile strength. We found that there was a significant correlation between induced contraction and SMMHC (Fig. 2.5C) and between basal tone and smoothelin (Fig. 2.5D). This suggests that the VSMC phenotype may correlate with vascular tissue contractility.

2.4 Discussion

Recent results suggest cellular architecture affects contractile function in vascular smooth muscle (11, 51). Thus, we hypothesized that the cellular architecture would affect contractile function in confluent engineered vascular smooth muscle. Using a cell placement technique to provide initial conditions, we biased the cellular architecture within confluent vascular tissues and measured the tissues' contractile stress generation. Our results suggest that tissues where the cellular architecture was more elongated yielded higher contractile function (Fig. 2.4D,E). Previous work has shown similar results where we patterned VSMCs into fibrils of varying widths (11). In that study, we found that thinner fibrils, where the cells are thinner and more elongated, exhibit greater contractile stress. In addition, single cell traction force microscopy studies in which VSMCs were patterned into various rectangular aspect ratios show that cells with greater aspect ratios exhibit a greater percent change in contractile stress upon chemical stimulation

n(68). However, in both of those studies artificial ECM boundaries were used to enforce the architecture leading to a lack of complete cell–cell contacts. *In vivo*, VSMCs exist as concentric confluent lamellae (70). The confluence of cell–cell contacts is an important property to mimic *in vitro* because VSMCs switch phenotype based on cell density and thus cell–cell contact (51, 52). At sub-confluence, cells express synthetic markers and proliferate, a behavior distinct to the synthetic phenotype (51, 71). At confluence, VSMCs express markers indicative of natural contractile phenotype (51). Thus, using confluent tissues, as we did, allowed us to study a more physiological behavior of VSMCs.

To construct tissues with differing cell shape within a confluent monolayer, we utilized initial seeding conditions to bias the cellular architecture. Previous work has used physical barriers such as microgrooves or ridges to guide cell and tissue architecture (55, 72-74). Here, we use neighboring cells to guide tissue organization. We have developed a microfluidic capture array device (MCAD) that captures cells into traps of varying depth (Fig. 2.1A) and changes the local density of cell–cell contacts. After flowing the cells into the traps, the cells attach to the substrate and align along the micropattern (Fig. 2.1B). We can vary the depth of the traps within the device to control the microscale density of cell seeding on the substrate while keeping the mesoscale tissue density constant (Fig. 2.1C). Traditional methods of cell seeding *in vitro* are performed by placing a liquid suspension of cells onto a substrate. The fidelity of these techniques varies from user-to-user; but microfluidic seeding can provide a highly repeatable method of seeding. By using a microfluidic cell seeding method, and varying the size of the traps to control the distribution of cell–cell contacts locally, we are able to place cells onto a substrate either as single cells (15 μm traps) with low cell–cell contact, or as multicellular aggregates (100, 200 μm traps) with high cell–cell contact. The neighboring cells in the higher depth traps provide contact guidance which forces the cells to elongate due to lateral contact with neighboring cells. After removing the device, the tissues become confluent overnight regardless of the initial seeding conditions. When we serum starve the VSMCs after tissue confluence (Fig. 2.2A),

they transform into a contractile phenotype (75), halting migration, and maintain the structure imposed by the initial cell–cell boundaries (Fig. 2.2E). Though our data suggest that cell–cell contact guidance at seeding influences the cell shape, it is notable that previous work has shown that increased cell–cell contact can lead to higher proliferation in vascular smooth muscle cells (76). Thus, the tissues constructed using the 100 μm and 200 μm MCADs may have increased rates of proliferation, which may also contribute to increased cell elongation through cell crowding.

Our results suggest that in the absence of other confounding differences, cell architecture alone can influence vascular tissue function. This finding is notable because VSMC structure varies from artery-to-artery and correlates with differences in residual stress and mechano-adaptation rates (77, 78). Notably, bifurcations of cerebral arteries have varying VSMC architecture (39), where they display rhomboid and irregular geometries associated with the synthetic phenotype. The majority of cerebral aneurysms occur in these bifurcations. Our results indicate that the less elongated VSMCs are less dynamically responsive, which could play a role in wall weakening in these regions during early aneurysm formation. In addition, synthetic VSMCs have been shown to produce greater matrix metalloproteinase-2 (MMP-2), which is an enzyme that is responsible for remodelling of the ECM (79, 80). Thus, it is important to study not only VSMC function but also phenotype in the context of vascular diseases.

VSMCs undergo phenotype change during development where they differentiate into a mature contractile phenotype (44). However, upon vascular injury or disease and in culture, VSMCs switch to a synthetic phenotype where they are more proliferative, less contractile, and more migratory (44, 45). The current paradigm in tissue engineering is to use phenotypic markers to determine tissue function(81-83). In our previous work we showed that phenotype does not correlate with function (84). However, in this study, we find that there is a subtle trend in phenotype with tissue architecture (Fig. 2.5A,B) and that the phenotype correlates with contractile function (Fig. 2.5C,D). In our previous work (84), we utilized artificial

boundary conditions with low cell–cell contact, which have been shown to be associated with a synthetic phenotype. In that study, we found that thinner fibrils were more contractile but expressed lower levels of contractile protein markers compared to wider fibrils, which may be due to the low cell–cell contact in the thinner fibrils. In addition, the phenotype differences seen in tissues with differing architectures were almost five-fold in the previous study, while in the current study they were less pronounced. This suggests that cell–cell contact influences phenotype expression more than cell shape but cell shape influences contractile function more than phenotype expression. In this study, we have engineered confluent tissues that are better mimics of confluent lamellae of VSMCs seen *in vivo*. Our results suggest that both VSMC function and phenotype can be influenced by the cellular architecture.

One primary goal in the field of tissue engineering is the development of an engineered small artery for implantation. A wide range of methods using either natural or synthetic scaffolds and even scaffold-free methods have been used to construct arteries (85-92). It has been shown that mechanical stimulation and growth factor stimulation all play important roles in vessel maturation and formation (93, 94). Our results suggest that controlling cellular architecture is another possible mechanism for engineering functional artery implants.

2.5 Methods

2.5.1 Cell culture

Human umbilical artery vascular smooth muscle cells (VSMCs) were purchased from Lonza at passage 3 and cultured at 37 °C and 5% CO_2 in a growth medium consisting of Medium 199 (GenDEPOT, Baker, TX) supplemented with 10% fetal bovine serum (Gibco, Grand Island, NY), 10 mM HEPES (Gibco), 3.5 g L^{-1} glucose (Sigma-Aldrich, St. Louis, MO), 2 mg L^{-1} vitamin B12 (Sigma-Aldrich), 50 U mL^{-1} penicillin–streptomycin (Gibco), 1× MEM non-essential amino acids

(Gibco), and 2 mM L-glutamine (Gibco). All experiments were conducted at passages 5–7.

2.5.2 Sample preparation

2.5.2.1 Device design

Microfluidic capture array devices (MCADs) (Fig. 2.1A) were designed using AutoCAD (Autodesk, San Rafael, CA) and photomasks were printed onto a Mylar film (Fineline Imaging, Colorado Springs, CO). Three device designs were fabricated. For each design, the depth of the cell capture trap (15 μm, 100 μm, 200 μm) was varied to change the initial cell seeding conditions on the substrate. Small 4 μm gaps were added to the bottom of each trap and along the length of the multi-cell traps to allow for streamlines to pass through and increase the efficiency of cell capture (Fig. 2.1B). The rows were staggered to distribute flow evenly through the device (64) and the appropriate column and row spacing were calculated to achieve an equivalent mesoscale cell seeding density for each design (Fig. 2.1C). In the case of the 15 μm MCADs, each trap had a width of 30 μm and a depth of 15 μm designed to trap a single VSMC (~20–40 μm diameter). The column and row spacing were 110 μm and 55 μm, respectively. In the case of the 100 μm MCADs, each trap had a depth of 100 μm and was designed to trap multiple cells along its length. The column and row spacing were increased to 210 and 130 μm, respectively. In the case of the 200 μm MCADs, each trap had a depth of 200 μm. The column and row spacing were 210 and 240 μm, respectively. For the 100 μm and 200 μm MCADs, the trap widths were increased to 45 μm.

2.5.2.2 Device fabrication

MCADs were fabricated using common soft photolithography methods (95) at the Minnesota Nano Center. First, a layer of SU-8 2002 (Microchem Corp., Newton, MA) was spun at 3000 rpm for 30 s onto a silicon wafer (Wafer World Inc., West Palm Beach, FL) to provide a 2 μm gap between the device features and the substrate. The first layer was exposed to UV light using a

photomask containing the channels of the device. After exposure, SU-8 3025 (Microchem Corp.) was spun at 2000 rpm to yield a 37 μm thick second layer. A second photomask, which contains the channels and features of the device, was aligned to the wafer, exposed to UV, and developed in SU-8 developer. Sylgard 184 polydimethylsiloxane (PDMS, Dow Corning) was used to mold devices from the master. The master was silanized overnight in a vacuum desiccator. PDMS at a 10 : 1 ratio of base : catalyst was poured onto the master and allowed to cure overnight at 90 °C.

2.5.2.3 Microcontact printing

Extracellular matrix (ECM) protein fibronectin (FN, BD Biosciences, San Jose, CA) was microcontact printed on a PDMS substrate using standard techniques(10). Briefly, PDMS substrates were prepared by spincoating a thin layer of PDMS onto a 25 mm coverglass, which was cured overnight at 90 °C. The FN solution (50 μg mL^{-1}) was incubated on a PDMS stamp with microscale-raised features (20 μm width lines and 5 μm pitch) for 1 h then blown dry. The PDMS substrate was exposed to UV ozone for 8 m and the stamps were placed in conformal contact with the substrate, transferring the protein. Slight pressure was applied to the stamp then the stamps were peeled away, leaving the micropatterned protein.

2.5.2.4 Cell seeding

MCADs were cleaned by sonication in 70% ethanol for 30 m. After drying, the MCADs were aligned with the FN patterned substrate so that the micropatterned lines were perpendicular to the inlet and the outlet of the device. Slight pressure was used to place the MCADs in conformal contact with the substrate. The MCADs were primed using 10% w/v bovine serum albumin (Hyclone, Logan, Utah) then flushed with phosphate buffered saline. VSMCs were trypsinized using 0.25% trypsin with EDTA (Invitrogen, Carlsbad, CA) and centrifuged at 200 relative centrifugal force for 5 m. After centrifuging the detached cells into a pellet, cells were resuspended to a concentration of 200

000 cells per mL in growth medium. The cell suspension was then flowed through the device at approximately 100 μL min−1 by applying house vacuum at the outlet. 600 μL of cell suspension was drawn through the MCAD and then 400 μL of growth medium was flowed through the device to rinse away cells not trapped in the device features. After 45 min of incubation at 37 °C, the devices were peeled away from the substrate and the constructs were allowed to incubate overnight in growth medium. For non-device samples, cells were seeded onto a micropatterned PDMS substrate in a 6-well dish at a density of 220 000 cells per well. For all imaging and MTF experiments, tissues were serum-starved for 24–48 h to induce a contractile phenotype (75).

2.5.3 Histochemistry

Tissues were fixed using 4% paraformaldehyde (Electron Microscopy Sciences, Hardfield, PA) for 5 m then stained for F-actin (Alexa Fluor 488 Phalloidin, Life Technologies) and nuclei (DAPI, 4′,6-diamidino-2-phenylindole, Life Technologies). Stained tissues were imaged using an Olympus X-81 fluorescent microscope at 20× magnification. F-actin and nuclei images were obtained by capturing ten random fields of view in a single tissue and three tissues per condition. Seeding density was calculated by quantifying the number of nuclei per area. Tissue alignment was analyzed using F-actin and nuclei images. Orientational order parameter for a single tissue was calculated for actin fiber and nuclei orientation (11, 96, 97) where an OOP of 1 indicates anisotropic alignment and an OOP of zero indicates isotropic alignment within the tissue. Nuclear shape was analyzed by fitting an ellipse to each nucleus. Nuclear eccentricity was defined as:

$$\varepsilon=\sqrt{1-\left(\frac{minor\ axis\ length}{major\ axis\ length}\right)^2}.$$

Tissue thicknesses were determined by obtaining confocal stacks (0.2 μm slices, 30 μm stacks) of actin at 40× magnification using an Olympus disk spinning unit. Confocal stacks were deconvolved using Autoquant software

(Media Cybernetics, Rockville, MD). A custom Matlab script was used to determine tissue thickness from the deconvolved stacks.

2.5.4 Cell lateral constraints analysis

Cells were imaged using a Nikon TS100 microscope. The lateral constraint was measured by determining the number of lateral cell constraints transverse to tissue alignment immediately after removal of the MCAD. A lateral constraint was defined as the number of cells in contact with the edge of the cell of interest, transverse to the direction of micropattern alignment. If two cells were both constraining the same transverse edge, we considered this a single lateral constraint. Thus, the number of lateral constraints could be zero, one, or two for a cell of interest. The number of transverse cell contacts (0, 1, 2) was assigned manually. A minimum of 45 cells were measured for each condition. Non-device samples were not analyzed due to the time dependence of cell attachment to the substrate.

2.5.5 Cell shape measurement

Cell shape was measured by determining the aspect ratio of cells immediately after MCAD removal. For non-device samples, cells that were at the surface of the substrate (0 m) were tracked and the aspect ratio was measured at 45 min, corresponding with MCAD removal time. Phase contrast images of the seeded substrates were obtained using a Nikon TS100 microscope. The cell was manually outlined using ImageJ. The aspect ratio was determined by fitting a line through the horizontal axis of the cell parallel to tissue alignment and the vertical axis of the cell transverse to tissue alignment (Fig. 2.3A). The aspect ratio was calculated as the ratio of the horizontal length divided by the vertical length. A minimum of 80 cells were analyzed for each condition.

2.5.6 Muscular thin film assay

Muscular thin films (MTF) were constructed as in previous publications (11, 96-98). Briefly, a 7 mm strip of a thermosensitive polymer poly(*N*-isopropylacrylamide) (PIPAAm, Polysciences) was spin coated onto the center of a 25 mm coverglass. PDMS doped with 0.2 μm fluorospheres (Polysciences) was then spincoated onto the PIPAAm coated coverglass and allowed to cure overnight at 90 °C. The thickness of the PDMS thin film was measured using a Tencor P-10 stylus profilometer at the University of Minnesota Characterization Facility. Tissues were seeded on the MTF constructs as described above. MTF assay was performed using a method described in Grosberg et al (97). Briefly, tissue constructs were removed from the incubator and placed in a petri dish containing Tyrode's buffer at 37 °C. Thin strips of tissue approximately 1 mm × 3 mm were cut from the substrate on three sides. The dish was allowed to cool briefly below 32 °C, dissolving the PIPAAm. The thin strips were then gently peeled from the glass to yield flexible thin beams consisting of a PDMS layer and a cell layer. The construct was then transferred to the experiment dish containing Tyrode's buffer at 37 °C and allowed to equilibrate for 20 m prior to chemical stimulation. The MTFs were stimulated with 50 nM endothelin-1 (ET-1) for 10 m followed by treatment with 100 μM HA-1077 for 30 m. The projection length of the MTFs was measured from images taken using a Lumar V12 stereoscope (Carl Zeiss) under fluorescent illumination sampled at 30 s intervals. The radii of curvature were calculated from the measured projection length. The tissue stress was calculated from the radius of curvature using a custom Matlab program. Mathematical details can be found in Alford et al (98). Tissue stress was normalized to the average of the non-device tissue stress for each day to account for day-to-day variability.

2.5.7 Western blotting

Tissues were lysed with RIPA buffer containing 100 mM Tris (pH 7.4), 4 M urea, 5 mM EDTA, 0.5% SDS, 0.5% Nonidet P-40, and protease inhibitor cocktail (cOmplete Mini, Roche). Samples were run in a 4–15% Tris-HCL gel (Bio-Rad,

Hercules, CA) for 2 h at 120 V and transferred to a 0.2 μm PVDF membrane. The following primary antibodies were used; SMMHC 11 (Abcam, Cambridge, MA), smoothelin (Abcam, Cambridge, MA), and β-actin (Santa Cruz Biotechnology, Dallas, TX). LICOR secondary antibodies were used to visualize the protein on the LICOR Odyssey (LICOR, Lincoln, NE). All samples were quantified using Image Studio Lite Version 3.1 and normalized to their respective β-actin loading control and then normalized to the non-device control sample average signal for each respective gel.

2.5.8 Statistics

Nuclear eccentricity data and cell contact analysis were performed using a Kruskal–Wallis One Way Analysis of Variance (ANOVA) on ranks and pairwise comparison significance was computed using Dunn's method. Tissue contractility data were analyzed using ANOVA and pairwise comparison with significance was computed using the Tukey test. All correlations between pairs of data were analyzed using Pearson Product Moment Correlation.

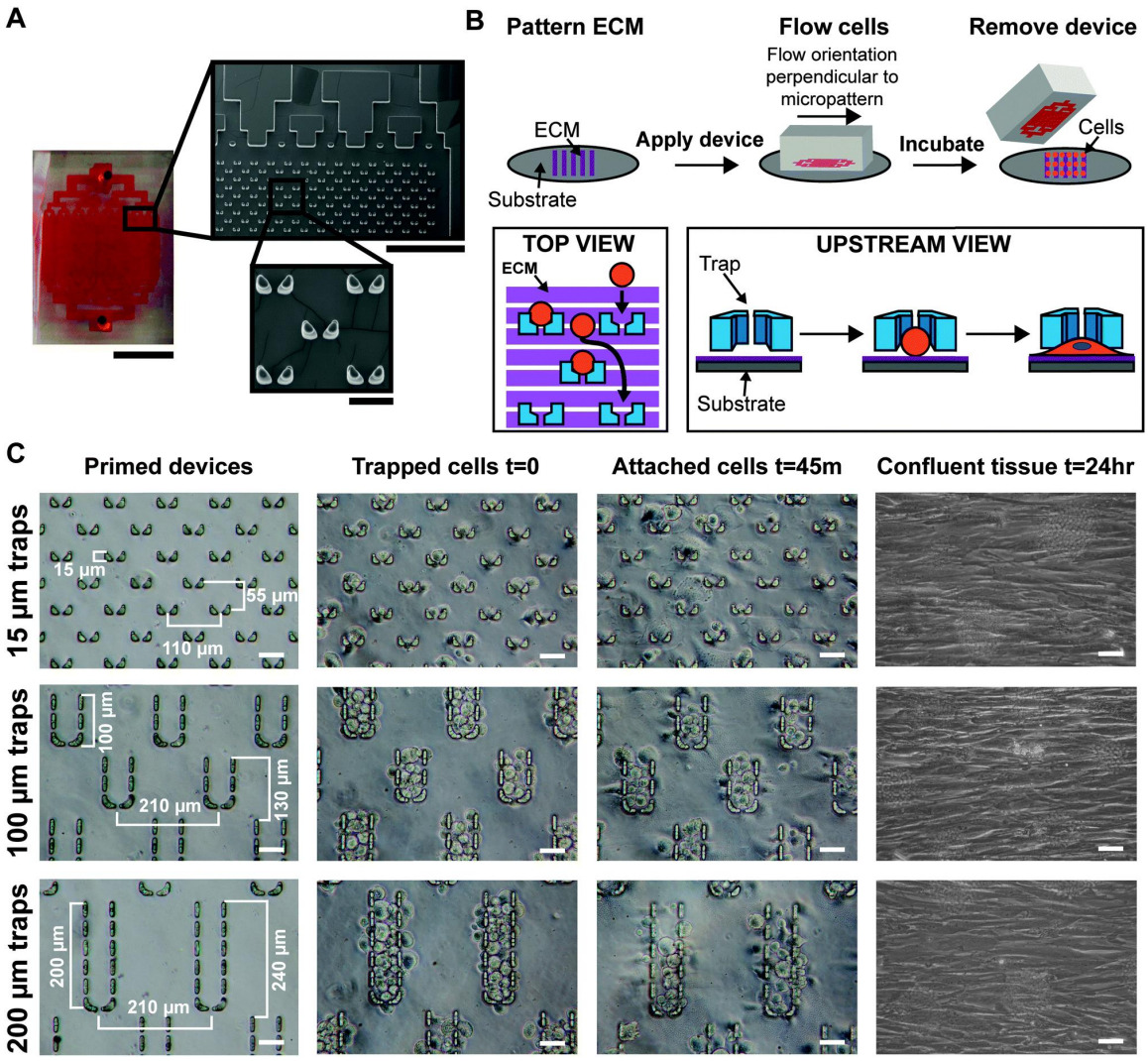

Figure 2.1. Cell seeding using the microfluidic capture array device

(A) Microfluidic capture array device (MCAD). Scale bar: 5 mm. Top inset: 100× SEM image. Branching channels at the inlet are designed to route cells into traps. Scale bar: 500 µm. Bottom inset: 500× SEM image. Each cell trap is designed to trap cells in between the protruding columns. Scale bar: 50 µm. (B) Micropatterning and cell seeding diagram. The substrate is patterned with the ECM prior to application of the device. A cell suspension is flowed through the device to trap cells hydrodynamically. A small gap between the trap columns and the substrate allows for cells to attach and spread on the substrate. (C) Phase contrast images of primed devices and VSMC seeding onto the micropatterned substrate. After traps are filled, the sample is

incubated for 45 min prior to device removal. An aligned and confluent tissue forms after overnight incubation. Scale bars: 50 μm.

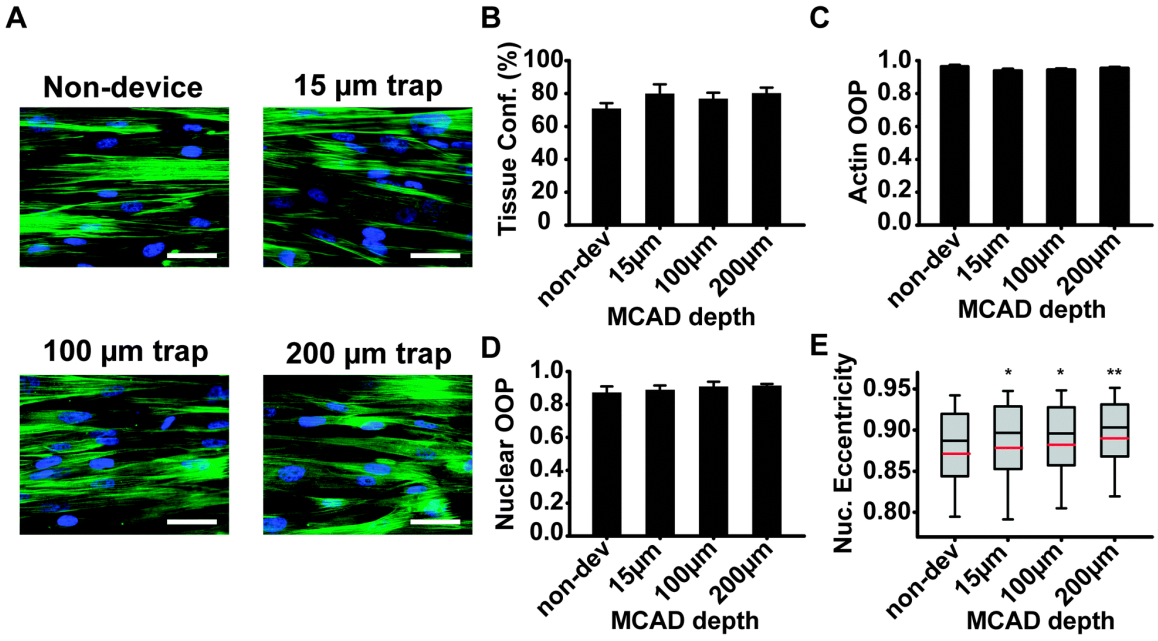

Figure 2.2. Sub-cellular and tissue architectures

(A) Fluorescent images of tissues after overnight incubation. Green: F-actin. Blue: nuclei. Scale bar: 50 µm. (B–E) Quantification of the cellular architecture for each seeding condition. (B) Tissue confluence measured by F-actin percent coverage. (C) Actin orientational order parameter. (D) Nuclear orientational order parameter. (B–D) Error bars = standard deviation. (E) Nuclear eccentricity. (Box = 25–75%, red line = mean, black line = median, error bars = 10–90%) (* = statistically different from non-device and 200 µm tissues, ** = statistically different from all other conditions, $p < 0.05$).

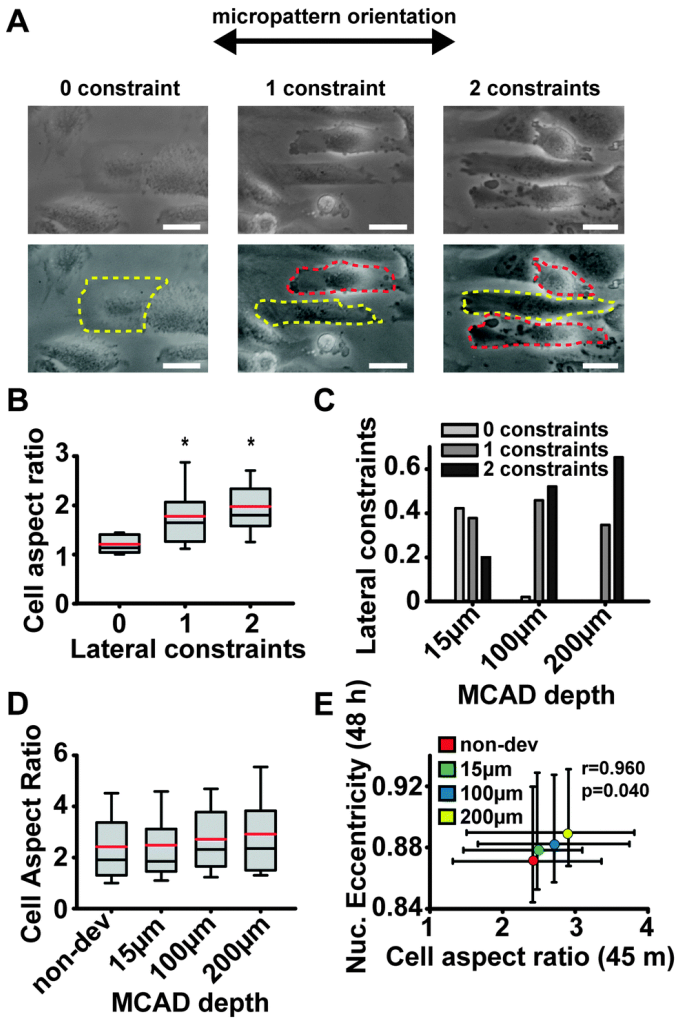

Figure 2.3. Initial seeding condition influences the cellular architecture in engineered tissues

(A) Quantification of cell shape 45 min after seeding. Yellow dashed line = the cell of interest. Red dashed line: cells acting as lateral constraints to the cell of interest. Scale bars: 25 μm. (B) Cell aspect ratio as a function of lateral constraints. (Box = 25–75%, red line = mean, black line = median, error bars = 10–90%) (* = statistically different from 0 cell contact condition, $p < 0.05$). (C) Histogram of lateral constraints from each device seeding. (D) Cell aspect ratio measured immediately after device removal (45 min). (Box = 25–75%, red line = mean, black line = median, error bars = 10–90%). (E) Correlation between mean cell aspect ratio (45 min) and mean nuclear eccentricity in tissues (48 h). Error bars = 25–75%.

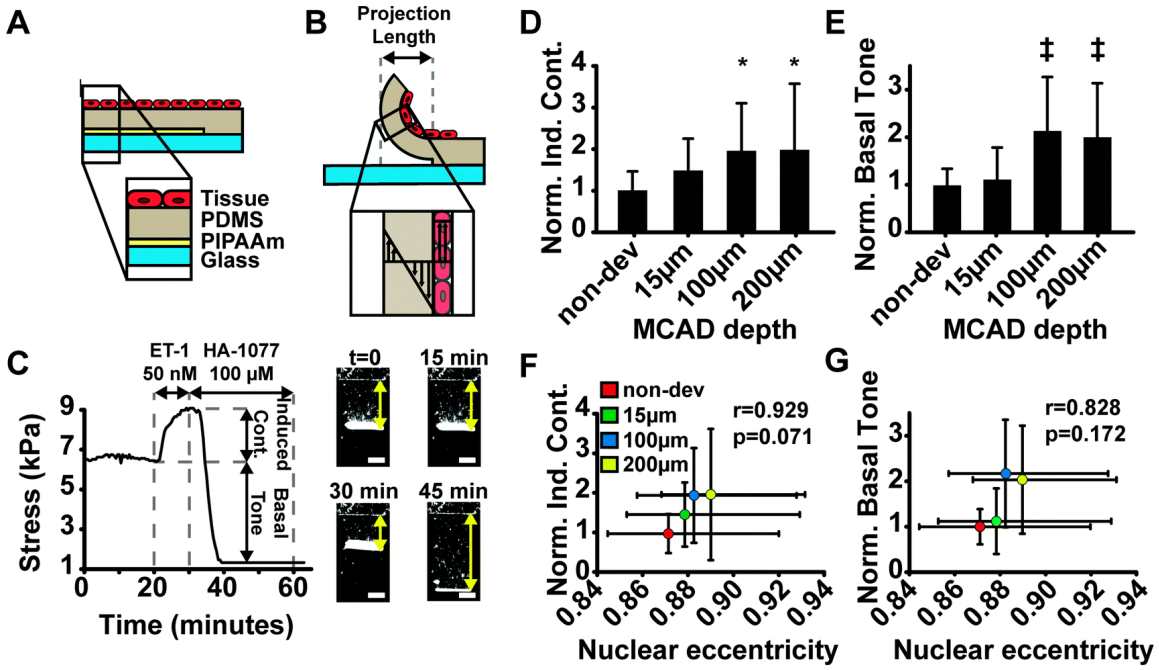

Figure 2.4. Muscular thin film (MTF) assay

(A) Thin film construction. The layers consist of a PDMS layer and an engineered tissue layer of VSMCs. (B) PIPAAm release yields a curved beam due to stress generated by the tissue layer. The projection length is used to calculate the radius of curvature which is used to calculate the stress in the tissue layer. Inset: theoretical transmural circumferential stress distribution. (C) Temporal tissue stress for a single MTF exposed to endothelin-1 generates an induced contraction followed by rho-kinase inhibitor HA-1077 to knock out all active contraction. The overhead view transmitted light images of a single MTF at specified time points show the projection length of MTF. The yellow arrows indicate the projection length of the thin film. Scale bar: 500 μm. (D) Normalized induced contraction stress after tissues are stimulated with 50 nM ET-1. (* = statistically different from non-device samples, $p < 0.05$). (E) Normalized basal tone after tissues were relaxed with HA-1077. (‡ = statistically different from non-device and 15 μm tissues, $p < 0.05$). Error bars = standard deviation. (F) Correlation between mean nuclear eccentricity and mean normalized induced contraction. (G) Correlation between mean nuclear eccentricity and mean normalized basal tone.

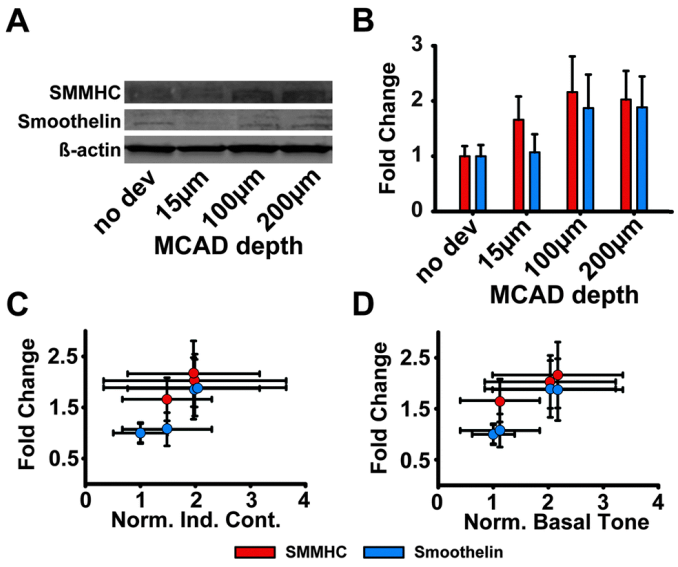

Figure 2.5. VSMC phenotype and function

(A) Western blot quantification of the VSMC phenotype. (B) Fold change expression of contractile markers normalized to control condition. Error bars: standard error. (C) Correlation of normalized induced contraction to fold change protein expression. (Pearson correlation: *r*, *p*). SMMHC: (0.986, 0.014); Smoothelin: (0.931, 0.069). (D) Correlation of normalized basal tone to fold change protein expression. (Pearson correlation: *r*, *p*). SMMHC: (0.894, 0.106); Smoothelin: (0.994, 0.006). (C and D) Error bars: *x*-standard deviation, *y*-standard error.

Chapter 3. Ceullular micro-biaxial stretching to measure a single-cell strain energy density function

This chapter contains material previously published in *Journal of Biomechanical Engineering* and is reproduced with permission. Win Z, Buksa JM, Luxton GWG, Barocas VM, and Alford PW (2017) Cellular micro-biaxial stretching to measure a single-cell strain energy density function.

3.1 Summary

The stress in a cell due to extracellular mechanical stimulus is determined by its mechanical properties, and the structural organization of many adherent cells suggests that their properties are anisotropic. This anisotropy may significantly influence the cells' mechanotransductive response to complex loads, and has important implications for development of accurate models of tissue biomechanics. Standard methods for measuring cellular mechanics report linear moduli that cannot capture large-deformation anisotropic properties, which in a continuum mechanics framework are best described by a strain energy density function (SED). In tissues, the SED is most robustly measured using biaxial testing. Here, we describe a cellular micro-biaxial stretching (CμBS) method that modifies this tissue-scale approach to measure the anisotropic elastic behavior of individual vascular smooth muscle cells (VSMCs) with native-like cytoarchitecture. Using CμBS, we reveal that VSMCs are highly anisotropic under large deformations. We then characterize a Holzapfel-Gasser-Ogden type SED for individual VSMCs and find that architecture-dependent properties of the cells can be robustly described using a formulation solely based on the organization of their actin cytoskeleton. These results suggest that cellular anisotropy should be considered when developing biomechanical models, and could play an important role in cellular mechano-adaptation.

3.2 Introduction

Active mechanical feedback between cells and their environment has important implications for tissue homeostasis and repair as it influences stem cell differentiation (99), tissue self-organization (100, 101), and the ability of tissues to adaptively grow and remodel in response to mechanical forces (102, 103). Many tissues are composed of highly organized fibrous matrices with anisotropic mechanical properties (104, 105), to which cells are highly attuned (106), suggesting an important role for anisotropy in mechanobiology. Cells found in mechanically dynamic tissues, like muscle and arteries, have similarly organized structure (39, 107), likely resulting in tissue-like anisotropic mechanical properties, and potentially influencing mechanotransductive signaling (108-111). However, the general approach using current methods (e.g. bead cytometry (112), micropipette aspiration (113), atomic force microscopy (114) for measuring cellular elastic mechanical properties report linear moduli (115, 116) intended for assessment of small-strain isotropic materials.

A description of the full large-strain anisotropic properties of cells is necessary for developing robust mathematical models of tissue biomechanics. Cells that exist in dynamic mechanical environments must constantly adapt to maintain tissue integrity (117). Growth and remodeling theory often posits that this adaptation is driven by changes in cell stress (118). Theoretical approaches that capture this mechano-adaptation could be used to develop model-aided individualized medicine to, for example, predict aneurysm growth and rupture (119, 120). Modern tissue modeling approaches, like constrained mixture (121-125) and multiscale (126-128) models, require mechanical descriptions of each of the constituents in the tissue. So, for these models to be successful, it is vital that we understand how the complex forces and deformations impact cellular mechanics and mechanotransduction. But, the large-strain anisotropic properties needed for the models have not been empirically determined.

Here, we seek to measure large-strain anisotropic properties of cells which can be used to improve multiscale models of tissues. In continuum mechanics, the full elastic mechanical behavior of a material is described by the strain energy density function (SED) (129). The gold standard method for measuring the SED of tissue samples is biaxial testing (104, 105). While tissue-scale biaxial testing requires samples to be physically clamped or sutured to the testing apparatus, this is not feasible with individual cells. Thus, we have developed cellular micro-biaxial stretching (CμBS) microscopy to measure the large-deformation SED of micropatterned adherent cells by modifying tissue-scale stretching methods and coupling them with traction force microscopy (130). Using this approach, we find that vascular smooth muscle cells (VSMCs) with native-like elongated geometries have highly anisotropic cell-shape dependent mechanical properties, and can be described by a simple SED determined by the organization of the VSMC actin cytoskeleton.

3.3 Methods

3.3.1 Substrate fabrication and cell micropatterning

Micropatterned polyacrylamide-elastomer composites were fabricated by combining the methods of Simmons et al. (131) and Polio et al (132) (Fig. 3.1A). Elastomer membranes (0.01” thick, Specialty Manufacturing, Sagniaw, MI) were clamped into membrane grips and placed under slight tension using custom fabricated grip holders so that the membranes were taut. Glass slides were adhered to the bottom of the membranes to prevent oxygen diffusion into the membrane during subsequent steps. Polydimethylsiloxane (PDMS) rings (30 mm diameter x 3 mm wall thickness) were then bonded to the membrane to retain cell culture media. Ideally, biaxial stretching would be performed using a large number of stretching protocols on a single sample (104, 133). However, cells remodel in response to mechanical load (134), which limits the number of protocols to which a single cell can be exposed. To overcome this limitation, VSMCs were micropatterned with identical architectures, conferring a uniform

geometry for direct comparison between cells exposed to different stretching protocols. Standard photolithography techniques were used to design PDMS stamps with arrays of 4000 μm^2 features, as previously published (135), of varying aspect ratios (AR). Aspect ratios (AR1: 63 µm x 63 µm; AR2: 91 µm x 44 µm; AR4: 127 µm x 32 µm; AR8: 175 µm x 22 µm) were chosen to mimic the ranges of physiological shapes ranging from cobblestone shapes in blood vessel bifurcations and more elongated geometries seen in unbranched blood vessels (39). Stamps were inked with 100 µg/mL of human fibronectin (BD Biosciences) for 1 hr. The stamps were blown dry with air, then placed in conformal contact with an O_2-plasma treated 15 mm glass coverslips for 30 min. Elastomer membranes were functionalized with photoinitiator benzophenone (10% w/v in 35:65 water/acetone) by placing 1 mL of solution onto the center of the membrane within the boundary of the PDMS ring for 1 min. The membranes were then rinsed 3x with methanol and degassed for 30 min to remove oxygen. Pre-polymer gel solution was prepared with 10/0.13/0.005% w/v acrylamide/bis-acrylamide/acrylic acid N-hydroxysuccinimide (Sigma), 0.014% 1 M HCl, 0.01% 0.2 µm red fluorescent beads (Polysciences) and degassed for 15 min, then, 0.002/0.05% w/v of tetramethylethylenediamine/ammonium persulfate (Sigma) was added. Degassed and functionalized membranes were vented to N_2 gas. 10 µL of the prepolymer solution was deposited onto the functionalized elastomer and covered with the micropatterned coverslip (patterned side down). The gels were then exposed to UV illumination using a Jelight 342 UVO Cleaner for 30 min approximately 1 in away from the UV lamp. After polymerization, gels were hydrated in 1x phosphate buffered saline for 15 min and the coverglasses were removed. Gels were then passivated with 4% bovine serum albumin for 1 hr and then incubated in cell growth media for 48 hr at 37 °C to remove residual benzophenone and unreacted pre-polymer constituents. Gel moduli were measured by fabricating dog-bone shaped (~5 mm width, ~5 mm thick, ~50 mm length) gels in a custom mold and performing uniaxial testing using an Instron biaxial stretcher (Tissue Mechanics Lab, University of Minnesota).

3.3.2 Stretcher design

Cellular micro-biaxial stretching (CμBS) was used for simultaneous stretching and imaging of cells. The CμBS device consists of four independent linear actuators (M-111.1DG, M-110.1DG, Physik Instrumente) (Fig. 3.1B) with a total travel range of 20 or 30 mm (50% or 75% strain), controlled by a servo-motor controller (C-863, PI), and mounted on to the microscope stage. Custom stainless steel arms and membrane grips (Fig. 3.1B) mounted to the actuators constrained a cruciform shaped elastomer membrane. CAD plans for all custom-designed parts will be provided on request. Grip strain was calculated by measuring distance between the grips with respect to the initial distance between the grips. Substrate strain to grip strain calibration was performed by tracking bead displacement in the top layer of the gel during cell-free stretch (see Fig. 3.2D) applied by the actuator membrane grips and calculating strain (Fig. 3.1C,D). We define a ~50 μm x 50 μm region centered about the microscope field of view and measure the locations of the beads in the corner of the region. The substrate strains were then calculated by measuring relative displacement of beads with respect to the original locations for each step of grip strain.

3.3.3 Cell culture

Human umbilical artery vascular smooth muscle cells (VSMCs) were purchased from Lonza at passage 3 and cultured at 37 °C and 5% CO_2 in a growth medium consisting of Medium 199 (GenDEPOT, Baker, TX) supplemented with 10% fetal bovine serum (Gibco, Grand Island, NY), 10 mM HEPES (Gibco), 3.5 g L^{-1} glucose (Sigma-Aldrich, St. Louis, MO), 2 mg L^{-1} vitamin B12 (Sigma-Aldrich), 50 U mL^{-1} penicillin–streptomycin (Gibco), 1× MEM non-essential amino acids (Gibco), and 2 mM L-glutamine (Gibco). All experiments were conducted at passages 5–7. Cells were seeded at a density of 5,000-15,0000 cells per gel-membrane construct overnight in growth media to allow cells to adhere to micropatterns. After overnight seeding, cells were serum

starved for a minimum of 24 hrs prior to all experiments to induce a physiological phenotype (136). All experiments were conducted at 37 ˚C in Tyrode's solution.

3.3.4 Cell structure determination

Cells were fixed using 4% paraformaldehyde (Electron Microscope Sciences, Hardfield, PA) for 5 mins then stained for F-actin (Alexa Fluor 488 Phalloidin, Life Technologies), nuclei (DAPI, 4',6-diamiidino-2-phenylindole, Life Technologies) and microtubules (YL ½ hybridoma, Sigma-Aldrich). F-actin and microtubules were imaged using an Olympus X-81 fluorescent microscope at 40x magnification (UPLSAPO40X2, NA 0.95) using a Hamamatsu ORCA-R2 (C10600) CCD camera, and fiber distributions were measured using a custom Matlab code (84, 96). F-actin stacks were obtained using an Olympus FluoView FV1000 BX2 laser-scanning confocal microscope (UPlanFLN, 40X, NA 1.30) at the University Imaging Centers (University of Minnesota). Cell thicknesses and volume were determined using a custom Matlab script (84). Cell cross-sectional area was determined by integrating the cell thickness over the cell width. The axial mid-plane area (A_x) was taken as the mean area over the middle 50% of the cell. The transverse midplane area (A_y) was calculated similarly. Cell architecture was determined using at least 10 cells per micropattern aspect ratio.

3.3.5 Single cell biaxial testing

For the standard experiment, substrates were stretched by applying increments of 5% grip strain up to 25% uniaxial (uniaxial-axial (uniaxial-A), in the direction of cell alignment, or uniaxial-transverse (uniaxial-T), transverse to cell alignment) and 20% equibiaxial strains at 0.1%/s (Fig 3.2A,B). Note: 5% grip strain equated to ~4% substrate strain at the cell/gel interface (see Fig 3.1C). At each increment, brightfield images of the cells and fluorescent images of the beads at the top layer of the gel were obtained at 40x magnification (UPLSAPO40X2, NA 0.95, Olympus X81). The cells were then lysed with 0.1% SDS and the stretching protocol was repeated (Fig. 3.2B). For the repeated

stretch experiments, the stretch was repeated four times prior to cell lysis. To determine the contribution of major cytoskeletal components to the cell properties, cells were treated with nocodazole (20 μM) to inhibit microtubule polymerization or cytochalasin D (0.5 μM) to inhibit f-actin polymerization prior to stretch for 1 hr (137-139). A maximum of five micropatterned cells per substrate were imaged and analyzed in any single stretching experiment, to maintain consistency between experiments. Only cells with single nuclei, confirmed by nuclear staining post-stretch, were analyzed.

Pre and post lysis bead images were compared using particle image velocimetry (PIV) to determine the cell-induced substrate deformation (140). Displacement fields were calculated using 5x5 μm^2 grids interrogated every 2.5 μm. Average experimental displacement maps were generated assuming cell quarter symmetry. The displacement of the substrate about each cell quadrant was averaged for all cells of each aspect ratio.

Individual cell traction stress vectors were determined from bead displacements using an unconstrained Fourier transform traction cytometry (FTTC) algorithm (140) with a regularization factor of 1E-9 and assumed Poisson's ration of 0.5, yielding a grid of n substrate traction stresses vectors given by $\mathbf{T^n} = T_x^n \mathbf{e_x} + T_y^n \mathbf{e_y}$ where $\mathbf{e_i}$ is the unit vector in the i direction. The total traction force components f_x and f_y are given as

$$f_i = \sum_n \left(-T_i^n A^n \frac{r_i^n}{|r_i^n|} \right), \qquad [3.1]$$

where $i = x, y$, A^n is the area (6.25 μm^2) of discrete surface n, and $\mathbf{r^n} = r_x^n \mathbf{e_x} + r_y^n \mathbf{e_y}$ is the vector that described the location of surface n with respect to the center of the cell (135). The First Piola-Kirchhoff stresses (force with respect to undeformed cross-sectional area) P_x and P_y were taken as

$$P_x = \frac{f_x}{2A_x} \text{ and } P_y = \frac{f_y}{2A_y} \qquad [3.2]$$

3.3.6 Planar biaxial strain energy density determination

The cell was treated as an anisotropic incompressible material exposed to planar biaxial deformation (no shear). The deformation tensor $\mathbf{F} = \mathrm{diag}[\lambda_x, \lambda_y, \lambda_z]$ was taken as the observed deformation of the cell, where λ_i are the stretch ratios in the i direction (x: parallel to the long axis of the cell, y: parallel to the short axis of the cell, and the z: perpendicular to the gel surface). The 1st Piola-Kirchhoff stress in the i direction is given by

$$P_i = \frac{\partial W}{\partial \lambda_i} - \frac{\lambda_z}{\lambda_i}\frac{\partial W}{\partial \lambda_z} \qquad [3.3]$$

where W is the SED of the cell, $i = x, y$, and $\lambda_z = (\lambda_x \lambda_y)^{-1}$.

The cell was assumed to be composed of pre-stressed actin fibers within an isotropic matrix. The shear modulus of the matrix is given by μ_m. The actin fiber stiffness is characterized by the parameter C_f, and the stress-free shortening that the fiber would undergo if it was unconstrained is given by λ_a. The fibers were assumed to be oriented as described by the measured whole-cell orientation probability density in the x-y plane and with an assumed Gaussian distribution out of the x-y plane. The fiber orientation was used to determine a structure tensor $\mathbf{H} = \alpha_{ij}\mathbf{e_i}\mathbf{e_j}$, as defined by Gasser et al (141). (α_{ij}values for each AR can be found in Table 3.1.)

Briefly, fiber orientation was described by the unit vector $\mathbf{M}(\Theta, \Phi) = \sin\Theta\cos\Phi\mathbf{e_x} + \sin\Theta\sin\Phi\mathbf{e_y} + \cos\Theta\mathbf{e_z}$ where Θ and Φ are Eulerian angles with respect to the z and x axes, respectively and $\mathbf{e_i}$ is the unit vector in the i direction. The density function $\rho(\mathbf{M})$ was normalized so that

$$\frac{1}{4\pi}\int_\omega \rho\big(\mathbf{M}(\Theta, \Phi)\big)\mathrm{d}\omega = 1 \qquad [3.4]$$

and the structure tensor was given by

$$\mathbf{H} = \alpha_{ij}\mathbf{e_i}\mathbf{e_j} = \frac{1}{4\pi}\int_{\omega} \rho\big(\mathbf{M}(\Theta,\Phi)\big)\mathbf{M}(\Theta,\Phi)\mathbf{M}(\Theta,\Phi)d\omega. \quad [3.5]$$

When the fiber distribution is included, the SED of the cell was given as

$$W = \frac{\mu_m}{2}\left(\lambda_x^2 + \lambda_y^2 + \lambda_z^2 - 3\right) + \frac{C_f}{4}\left(\alpha_{xx}\left(\frac{\lambda_x}{\lambda_a}\right)^2 + \alpha_{yy}\left(\frac{\lambda_y}{\lambda_a}\right)^2 + \alpha_{zz}\left(\frac{\lambda_z}{\lambda_a}\right)^2 - 1\right)^2. \quad [3.6]$$

Parameter optimization was performed by comparing predicted vs experimental stress P_x and P_y at the six uniaxial stretches and five equibiaxial stretches corresponding with the measured substrate deformations (Uniaxial: $\lambda = 1.00, 1.04, 1.08, 1.12, 1.16, 1.20$ in the directions of stretch and $\lambda = 1.00, 0.99, 0.98, 0.97, 0.96, 0.95$ transverse to the stretch. Equibiaxial: $\lambda = 1.00, 1.04, 1.08, 1.12, 1.16$ in both directions). The range of possible parameters was limited to $\mu_m: 0.5 - 10\text{kPa}$, $C_f: 1 - 100\text{kPa}$, and $\lambda_a: 0.8 - 1.0$. This parameter range was determined using both the practical constraints of the model and physical assumptions of the cell. A too large mismatch between μ_m and C_f caused the finite element model used to validate this model (next section) to be unable to converge, limiting the range of μ_m. In previous models, $\lambda_a$was assumed to be 0.9 at homeostasis, with a minimum possible value (during maximum stimulation) of 0.6 (124). Since our cells were not being stimulated, we limited the range of λ_a. The parameter set that best fit the experimental data, as determined by least squares fitting, was determined to be optimal.

3.3.7 Finite element model

To validate the SED determined using planar biaxial assumptions, a quarter symmetry finite element model of the cell and underlying polyacrylamide and elastomer substrates was developed using COMSOL Multiphysics 4.2. The cell was modeled as hyperelastic and nearly incompressible with a SED of

$$W = \frac{\mu_m}{2}(I_1 - 3) + \frac{C_f}{4}(\mathbf{H}: (\mathbf{A^{-T}} \cdot \mathbf{C} \cdot \mathbf{A^{-1}}) - 1)^2 + \frac{\kappa}{2}(J-1)^2 \quad [3.7]$$

where $\mathbf{C} = \mathbf{F^T} \cdot \mathbf{F}$, $I_1 = \mathrm{tr}(\mathbf{C})$, $\mathbf{A} = \mathrm{diag}[\lambda_a, \lambda_a, \lambda_a]$, $J = \det(\mathbf{F})$, and κ is the bulk modulus. The gel and elastomer membrane were modeled as neo-Hookean, with a strain energy density function of

$$W = \frac{\mu}{2}(I_1 - 3) - \mu \ln(J) + \frac{\lambda}{2}(\ln(J))^2 \quad [3.8]$$

where μ is the shear modulus and λ is the first Lamè parameter. Gel parameters were taken from the experimentally determined Young's modulus (E) and assumed Poisson's ratio (ν) based on the relations $\mu = \frac{E}{3(1-2\nu)}$ and $\lambda = \frac{E\nu}{(1+\nu)(1-2\nu)}$. Elastomer parameters were based on standard PDMS values (142, 143).

The model geometry was meshed with tetrahedral elements using COMSOL's physics-controlled meshing sequence. The AR1 model had 21204 elements (cell: 821, gel: 10005, membrane: 10378). The AR2 model had 21265 elements (cell: 850, gel: 9945, membrane: 10470). The AR4 model had 22435 elements (cell: 929, gel: 11173, membrane: 10333). The AR7 model had 23870 elements (cell: 1146, gel: 12205, membrane: 10429). Displacement consistent with experimental strains was applied to the membrane and gel on the non-symmetry x-y planes. The top surface was free and the bottom surface was constrained from displacement in z. The governing equations were solved via quasi-static analysis. Prior to displacing the boundaries, the activation tensor, which is initially $\mathbf{A} = \mathbf{I}$ was incremented linearly with time until $\mathbf{A} = \mathrm{diag}[\lambda_a, \lambda_a, \lambda_a]$. The non-symmetry boundaries were then incremented linearly with time, while $\mathbf{A}$ was not varied. Cell-induced displacement (d) was determined as $d = ((u - u_o)^2 + (v - v_o)^2)^{1/2}$ where u and v are the displacements of the top surface of the gel in x and y and u_o and v_o are the expected displacements due to the prescribed boundary displacement. Model-predicted cell-induced substrate displacements (d) were then compared to the average experimental substrate displacements.

3.3.8 Statistical analyses

Differences in stress as a function of strain were compared by using a One Way Analysis of Variance (ANOVA) and pairwise comparison significance was performed using a Holm-Sidak test. Differences in P_x and P_y as a function of strain were compared by using a Two Way ANOVA and pairwise comparison significance was performed using a Holm-Sidak test. Similarly, nocodazole and cytochalasin D treatment were compared to control stress values for each aspect ratio cell and stretch using a Two Way ANOVA and pairwise comparison significance was performed using a Holm-Sidak test. Computational fits to experimental data were compared by computing $r^2 = 1 - \frac{SS_{res}}{SS_{tot}}$. Sum of squares of residuals and the total sum of squares were computed as $SS_{res} = \sum_i (y_i - f_i)^2$ and $SS_{tot} = \sum_i (y_i - \bar{y})^2$ over n values over i, where y_i are data values, f_i are predicted values, and $\bar{y}$ is the mean of data.

3.4 Results

3.4.1 Single-cell biaxial stretching with CμBS microscopy

To perform single-cell biaxial stretching, we developed the CμBS microscopy method to measure the stress in cells adhered to a deformable elastomer substrate. The CμBS device (Fig. 3.1B) can apply any combination of x-y strains up to 25% grip strain (Fig. 3.2A). Cells were micropatterned on a fluorescent bead-doped layer of polyacrylamide (Young's modulus: 13.5 +/- 2.2 kPa) adhered to an elastomer membrane and stretched by increments of 5% grip strain up to 25%, while the deformation of the substrate beneath the cell was measured using the displacement of the embedded beads. Traction force microscopy methods (130) were used to determine the traction stresses applied to the substrate by the cell at each stretch increment, by comparing substrate deformation during identical stretching protocols with the cells intact and after cell lysis.

3.4.2 VSMCs with native-like architecture exhibit anisotropic material properties

In vivo, VSMCs are normally organized into elongated spindles wrapped circumferentially around blood vessels (39). To mimic this architecture, the cells were micropatterned with an aspect ratio (AR) of 4:1 (AR4) (Fig. 3.3A). When the cells were stretched uniaxially parallel to their long axes (uniaxial axial, uniaxial-A), the cell-induced substrate deformation and traction force increased with increasing applied strain and decreased with decreasing strain (Fig. 3.3A,B). VSMCs were consecutively stretched four times over 110 minutes (Fig. 3.3B), during which we observed hysteresis during unloading, consistent with previous viscoelastic (144-148) or soft glassy (149) descriptions of cells. However, the cellular traction forces during both loading and unloading were consistent over the four stretches (Fig. 3.3C,D). The cycle-independent nature of the force-strain behavior indicates that the VSMCs were not plastically deforming (150) or significantly remodeling (151) during the stretching protocol, allowing their elastic properties to be measured. For the remainder of this work, we focused only on the first extension (increasing strain) of each cell, and did not perform repeated stretch.

Confocal microscopy was used to determine the 3-D geometry of the micropatterned cells. The mean axial and transverse cross-sectional areas were determined to be A_x = 78 μm^2 and A_y = 278 μm^2, respectively. The undeformed geometry was used to calculate the mid-plane first Piola-Kirchhoff stress (129) during stretching. For uniaxial-A stretching (Fig. 3.4A), the stresses in the direction of stretch (P_x) increased with strain, while transverse stresses (P_y) were lower and nearly constant (Fig. 3.4B). However, when the cells were stretched uniaxially parallel to their short axes (uniaxial transverse, uniaxial-T) (Fig. 3.4C) the stresses in both the stretched (P_y) and unstretched (P_x) directions were nearly unchanged over 0%-20% strain (Fig. 3.4D). When equibiaxially stretched (Fig 3.4E), the cells' stress-strain behavior in each direction mimicked that of the uniaxial stretch (Fig. 3.4F). This large-deformation mechanical anisotropy is

consistent with previous small-deformation studies in micropatterned cells (152). Taken together, these data demonstrate that there is significant material anisotropy in VSMCs with native-like elongated architecture (39).

3.4.3 Cellular architecture dictates VSMC material properties

The stereotypical elongated VSMC architecture is dramatically altered near small artery bifurcations (39). It is notable that cerebral aneurysms, which are thought to initiate due to a weakening of the artery wall, occur disproportionately around these bifurcations (153). To determine the effect of cellular architecture on mechanical properties, we performed CμBS microscopy on VSMCs micropatterned with matching adhesive areas, but varying aspect ratios (1:1 (AR1), 2:1 (AR2), 4:1 (AR4), 8:1 (AR8)) (Fig 3.5A). VSMC volume was fairly consistent in the patterned cells (AR1: 7841 +/- 2512 μm^3, AR2: 8954 +/- 3323 μm^3, AR4: 10164 +/- 3452 μm^3 AR1: 8831 +/- 2984 μm^3; only AR1 and AR4 were statistically different). But, the cross-sectional areas were altered by the micropatterning such that larger aspect ratios have decreasing axial cross-section (A_x) and increasing transverse cross section (A_y) (Fig. 3.5B). VSMCs with larger ARs had greater axial pre-stress and were stiffer when stretched parallel to their long axes, compared to VSMCs with smaller ARs (Fig. 3.5C). Conversely, cells with larger aspect ratios had lower transverse pre-stress and were less stiff when stretched transverse to their long axes (Fig. 3.5C). These trends were consistent for equibiaxial stretching (Fig. 3.5C). These results, taken as a whole, indicate that anisotropic pre-stress and resistance to strain depend on cellular architecture (39).

3.4.4 Actin cytoskeleton mediates whole-cell mechanical anisotropy

The actin and microtubule cytoskeletons are critical structural components of cells (116). We asked whether the observed cell shape-dependent mechanical properties were a result of changes in cytoskeletal architecture. To quantify their organization, we stained VSMCs for actin and microtubule filament systems (Fig.

3.6A) and found that both are highly anisotropic in high AR VSMCs (Fig. 3.6B,C), and increasing anisotropic alignment correlates with increasing mechanical anisotropy (Fig. 3.6B-E). To determine the contributions of these filament systems to the mechanical properties of VSMCs, axial and transverse uniaxial stretching was performed in cells treated with nocodazole or cytochalasin D, which act to depolymerize microtubule or actin filaments, respectively (138). While nocodazole treatment hardly altered the mechanical behavior of VSMCs (Fig. 3.6F,G), cytochalasin D treatment significantly reduced VSMC rigidity in comparison to control cells (Fig. 3.6H,I). Thus, these data suggest that the mechanical properties of VSMCs are mediated by the intact actin cytoskeleton.

3.4.5 Actin organization-based SED is sufficient to characterize VSMC mechanical properties

To determine the SED of VSMCs at the single-cell level, we first analyzed the CμBS method as planar biaxial stretching (i.e. no shear), as previously described for tissue-scale biaxial tests (104). We assumed that cellular deformation and material properties were uniform and described by a three-parameter SED using the measured actin orientation to define a distribution of pre-stressed fibers within an isotropic matrix (141) (see Table 3.1). Parameters were optimized so that the model reproduced the experimentally measured AR4 1st Piola-Kirchhoff stresses for all stretching protocols (Fig. 3.7A, Table 3.2). Next, we asked whether the AR4 SED could be generalized for any cellular architecture for which the actin orientation is known. To do this, we simulated planar biaxial tests of VSMCs with varying ARs. All parameters were identical to those determined for the AR4 cell, except the actin orientation, which was based on those measured for VSMCs of each aspect ratio (Table 3.1). For each of the experimental stretching protocols, this simple model was able to capture the stress-strain behavior of VSMCs of most ARs (Fig. 3.7B).

Adhered VSMCs are likely not truly undergoing shear-free planar biaxial deformation. To determine whether our planar biaxial model recapitulates the true dynamics of the cell, we developed a 3-D quarter symmetry finite element

(FE) model of the AR4 cell and its underlying substrate (Fig. 3.8A). When this model was used to replicate the three experimental stretching protocols, the VSMC-induced substrate deformation in the model mirrored the experimentally measured mean displacement throughout each stretching protocol (Fig. 3.8B-D), suggesting that our planar biaxial assumptions do not create excessive error. There was good agreement between FE model-predicted and experimentally measured substrate deformations for most ARs (Fig. 3.9), with AR1 deformations varying the most from the experimental, likely due to greater spatial heterogeneity in actin orientation. Thus, these data demonstrate that a simple SED based solely on the organization of the actin cytoskeleton can be used to describe the elastic properties of VSMCs.

3.5 Discussion

To determine the cellular stress induced by extracellular mechanical stimuli, it is necessary to know the mechanical properties of the cells. Here, we describe the CμBS method for performing biaxial tests on individual cells to determine the SED that fully describes their elastic mechanical properties. Standard methods for measuring cellular elastic properties, such as atomic force microscopy indentation (154), micropipette aspiration (155), magnetic tweezers (145), and magnetic twisting cytometry (156), report isotropic descriptions of the cell's properties, like Young's modulus. While this is sufficient for comparative studies (157), most adherent cells are not well-described by a single modulus due to their structural anisotropy. Our results show that VSMCs patterned with *in vivo* like architecture are highly anisotropic. Elongated cells were markedly stiffer when stretched parallel to their long axes, compared to their short axes. It is also notable that we found limited orthogonal coupling in VSMCs, which is unlike intact arteries, where axial stretch significantly alters pressure-radius behavior in vessel inflation tests (158).

VSMCs in arteries can undergo physiological strains of up to 15-25%, per cardiac cycle (159, 160), and under extreme conditions such as aneurysm

growth, chronic strains may be markedly larger. In this study, we used strains up to 20%, to measure large-deformation anisotropic mechanical properties that are appropriate for these cells. Many tissues, including arteries, have highly nonlinear material properties when exposed to large strains (158, 161). However, we did not find significant nonlinearity in VSMC stress-strain behavior, though it is notable that our strains were not as large as those in many tissue studies

The primary aim of this study was to determine the SED of VSMCs. It is important to know the SED, rather than a simple modulus, when developing computational models of cells and tissues. Cutting edge models of tissue mechanics, like rule-of-mixtures (121-125) and multiscale (126-128) models, consider the contribution of each tissue constituent independently. As a result, the assumed properties of these constituents can significantly alter model predictions (162). Thus, for models that simulate complex loads, the full anisotropic description captured by the SED is necessary. Here, we characterized native-like AR4 VSMCs with a simple three parameter SED that incorporates actin cytoskeletal organization. With only actin alignment altered, this SED was also able to describe cells patterned into other ARs, demonstrating that an architecture-dependent SED can robustly describe VSMCs.

In this study, we found that VSMCs with larger ARs have greater prestress and are stiffer in their long axes, which is consistent with evidence that cells with greater prestress exhibit increased stiffness (163). In a related study, it was found that in highly-aligned confluent engineered tissues, VSMC AR influences tissue prestress, even when actin organization is not significantly altered (36). In those tissues, agonist-induced contractility also increases with increased AR, possibly due to altered phenotype expression (36), suggesting that a model that considers both cytoskeletal organization and expression of a set of key phenotype markers could improve on the one presented here.

The CμBS method requires several assumptions that may affect experimental robustness. We assume that the cell is a continuum body with a

uniform SED throughout, ignoring the contribution of the nucleus (164, 165) and spatial variation of cytoskeletal organization. Thus, we report an average planar cell stress, with no assumptions of the stress distribution in the cell. We ignored viscous behavior and assumed that the cells were purely elastic when determining the SED. However, we observed hysteresis during cell unloading, demonstrating time-dependent mechanical properties that have been previously described with both viscoelastic (144-148) and soft glassy rheology (149) theories. Another shortcoming of this study is that we did not study the range of possible SEDs, only one formulation. In addition, due to constraints in the data range over which the model would converge, we did not sample the entire possible parameter space. This is most notable in our fitting of μ, which is at the bottom of our tested data range and for which there is no physical reason that it could not be lower. Finally, CμBS only truly measures two dimensional properties, and it has been shown that adherent cells exert forces normal to their substrates (166, 167). In the VSMCs studied, the primary orientation of the actin cytoskeleton is in 2-D plane measured, so though there is out-of-plane rigidity, it is likely that it is relatively low. Although beyond the scope of this study where we study mechanical properties of single cells, multi-cellular monolayers have been shown to exhibit complex material properties due to cell-cell contact. In the future, CμBS microscopy can be extended to study mechanical properties of multi-cellular monolayers (168).

Early elasticity-based measurements, like biaxial testing, formed the basis of the field of modern soft-tissue biomechanics (104). These studies not only demonstrated the complex structure-function relations of tissues (169-171), but laid the foundation for the tissue-scale growth and remodeling theory currently used to model how tissue function is affected by mechanical perturbations (172, 173). Today, mechanobiology researchers are making great strides toward understanding how cells transduce mechanical forces (174-176). However, nearly all of these studies describe the properties of the cells and their environment in terms of a modulus or stiffness. Our demonstration that cells, like

tissues, have complex anisotropic properties suggests their mechanotransductive response to applied loads may be similarly anisotropic, which must be taken into consideration.

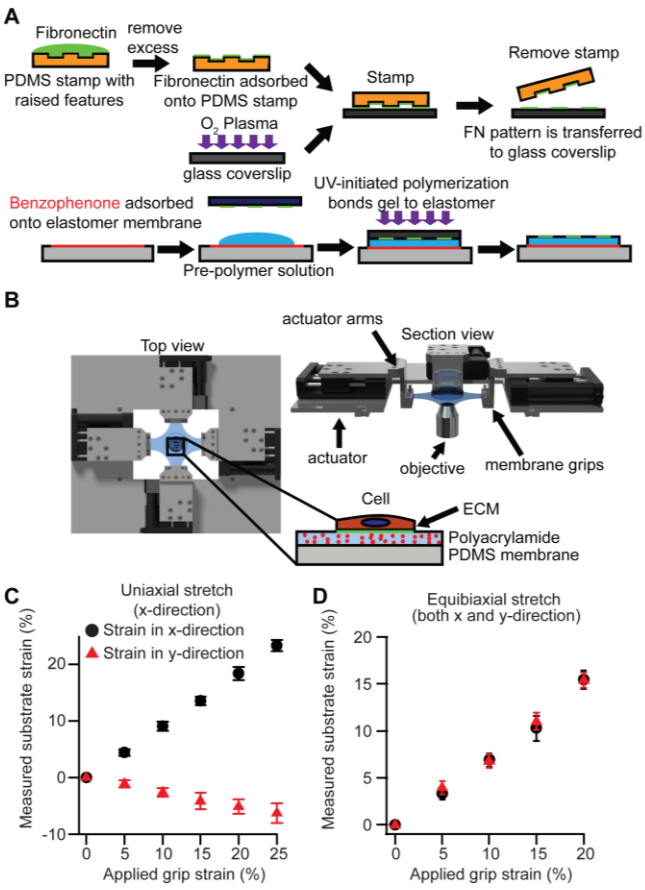

Figure 3.1. Fabrication of substrate and cellular micro-biaxial stretching device.

(A) Schematic representation of substrate fabrication process. (B) Schematic representation of the CμBS device. Inset: cell substrate. (C) Grip strain vs measured substrate strain under applied uniaxial grip strain (n=10). (D) Grip strain vs. measured substrate strain under equibiaxial grip strain. Error bars: standard deviation (n=10).

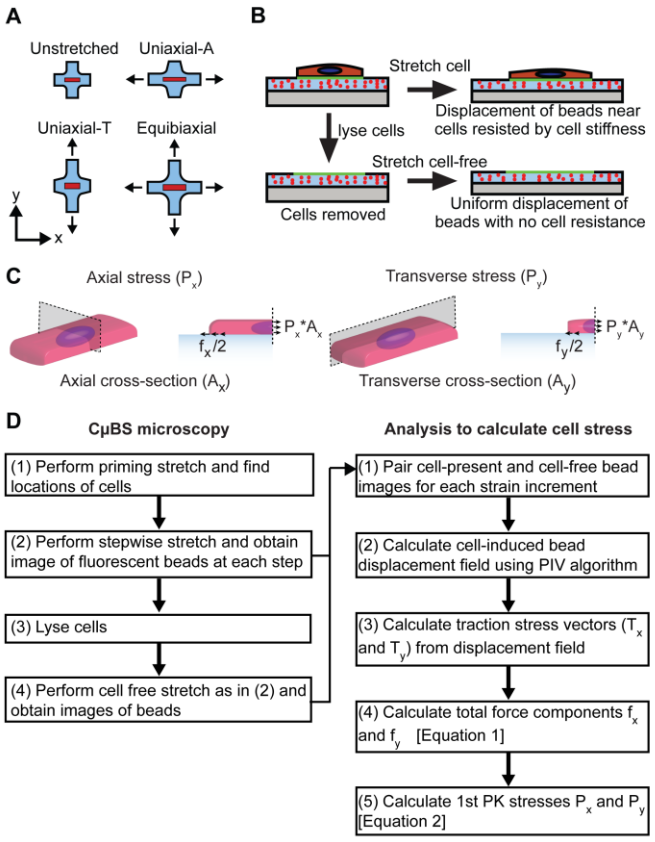

Figure 3.2. Cell stretching and stress measurement.

(A) Uniaxial and biaxial stretching protocols. (B) Protocol to determine substrate displacements used to calculate cell-induced substrate traction force. (C) Schematic for calculating First Piola-Kirchhoff stress from measured substrate traction force. (D) Flowchart describing CμBS microscopy technique and cell stress calculation.

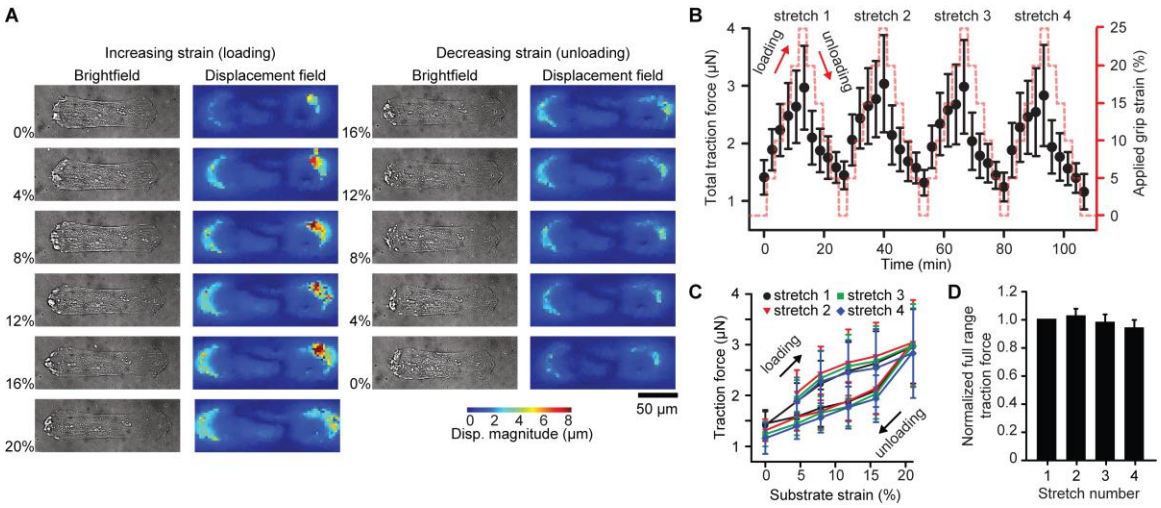

Figure 3.3. Repeated cell stretching and hysteresis.

(A) Representative images of a single AR4 VSMC during one cycle of loading and unloading. Left columns: brightfield image of cell. Right columns: cell-induced bead displacement field. (B) Total traction force (f_x) generated by AR4 cells undergoing loading and unloading cycles during repeated uniaxial-A stretch (n=9). (C) Total traction force (f_x) exerted by AR4 cells during cyclic loading over four sequential stretches (n=5). (D) Normalized cycle-to-cycle in total traction force relative to the first stretching cycle for cells exposed to four sequential uniaxial-A stretches. All error bars: standard deviation.

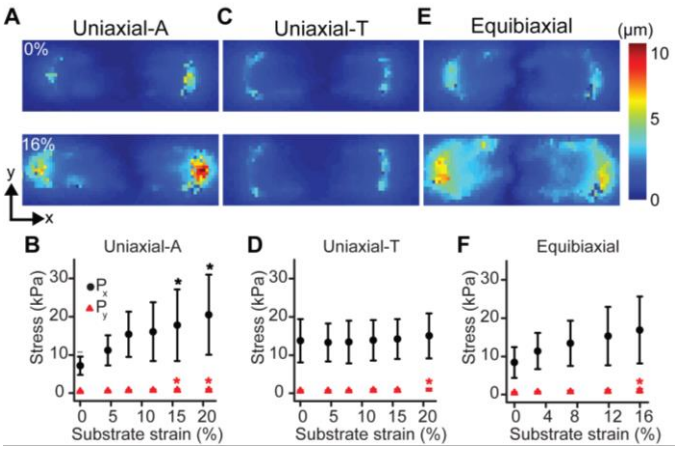

Figure 3.4. Mechanical anisotropy in biaxially stretched micropatterned VSMCs.

(A,C,E) Representative cell-induced displacement fields for unstretched and 16% strain AR4 VSMCs undergoing (A) uniaxial-A (n=10), (C) uniaxial-T (n=13), and (E) equibiaxial stretch (n=9). (B,D,F) First Piola-Kirchhoff stresses in AR4 cells during (B) uniaxial-A (*,*=significant from 0%, $p< 0.05$), (D) uniaxial-T (*=significant from 0, 4, 8%, $p< 0.05$), and (F) equibiaxial stretching (*=significant from 0%, $p< 0.05$). All error bars: standard deviation.

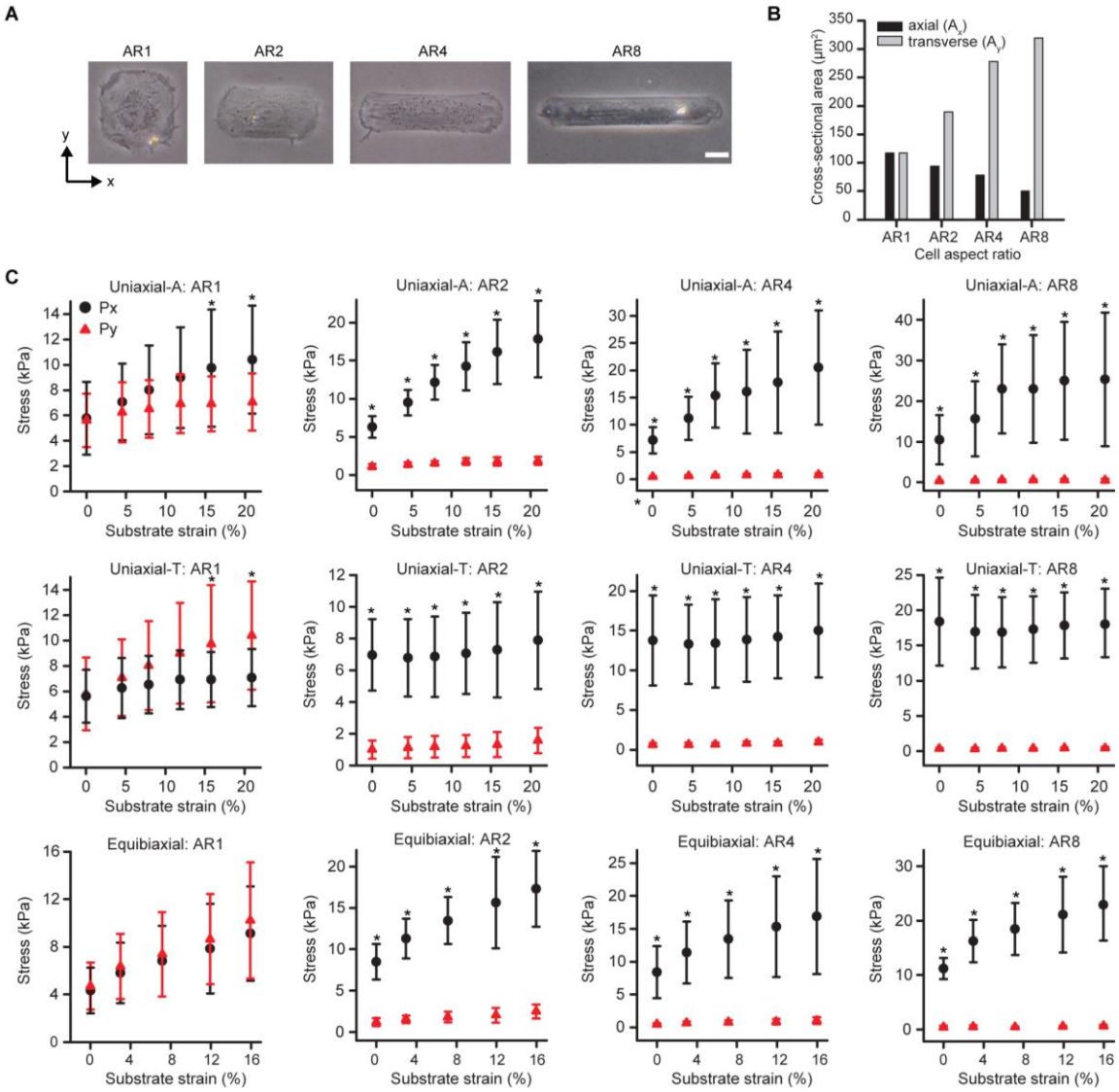

Figure 3.5. Cell shape influences mechanical properties.

(A) Brightfield images of micropatterned cells with identical adhesive area, but varied aspect ratios (1:1 (AR1), 2:1 (AR2), 4:1 (AR4), 8:1 (AR8)). Scale bar: 20 μm. (B) Measured cell cross-sectional areas from average cell thickness maps. (C) First Piola-Kirchhoff stresses for all active cells during uniaxial- A, uniaxial-T, and equibiaxial stretching. Error bars: standard deviation. Uniaxial-A: AR1 (n=10), AR2 (n=10), AR4 (n=10), AR8 (n=9). Uniaxial-T: AR1 (n=10), AR2 (n=11), AR4 (n=13), AR8 (n=9). Equibiaxial: AR1 (n=10), AR2 (n=10), AR4 (n=9), AR8 (n=10). (*=P_x significant from P_y at same strain, $p< 0.05$)

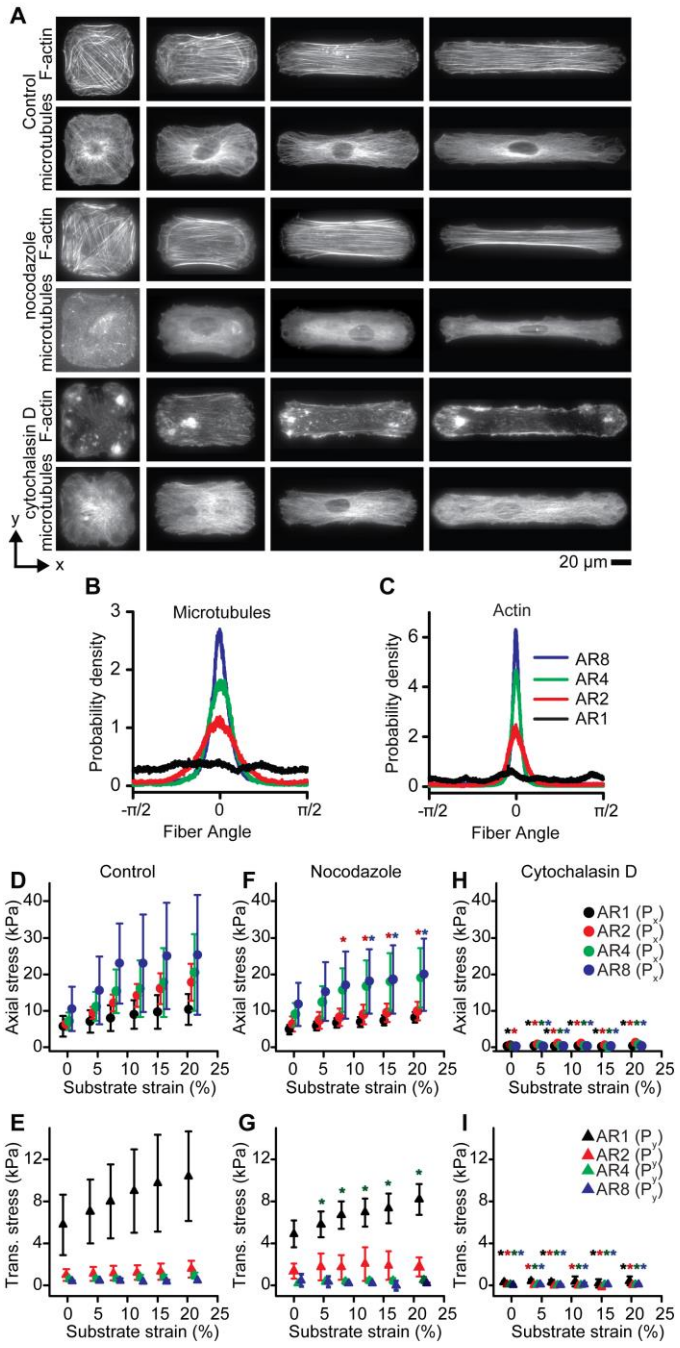

Figure 3.6. Cytoskeletal structure influences mechanical properties.

(A) Representative immunofluorescent images of F-actin and microtubules in representative micropatterned cells for each aspect ratio. Top: DMSO control. Middle: Nocodazole treated. Bottom: Cytochalasin D treated. (B) Microtubule filament orientation. Measured from n=10 cells. (C) Actin filament orientation. Measured from n=10 cells. (D,F,H) Axial First Piola-Kirchhoff stress (P_x) in

VSMCs during uniaxial stretch in axial direction (D) Control cells (n=10). (F) Nocodazole treated (n=10). (H) Cytochalasin D treated (n=6). (E,G, I) Transverse First Piola-Kirchhoff stress (P_y) in VSMCs during uniaxial stretch in the transverse direction (E) Control cells (n=13). (G) Nocodazole treated (n-4). (I) Cytochalasin D treated (n=6). All error bars: standard deviation. Note: Data staggered about strain values to prevent overlapping data. (D, F, H) Y-axis scaled to maximum of P_x. (E, G, I) Y-axis scaled to maximum of P_y. (*,*,*,*=significant from control at same strain with same AR $p < 0.05$ for respective aspect ratios)

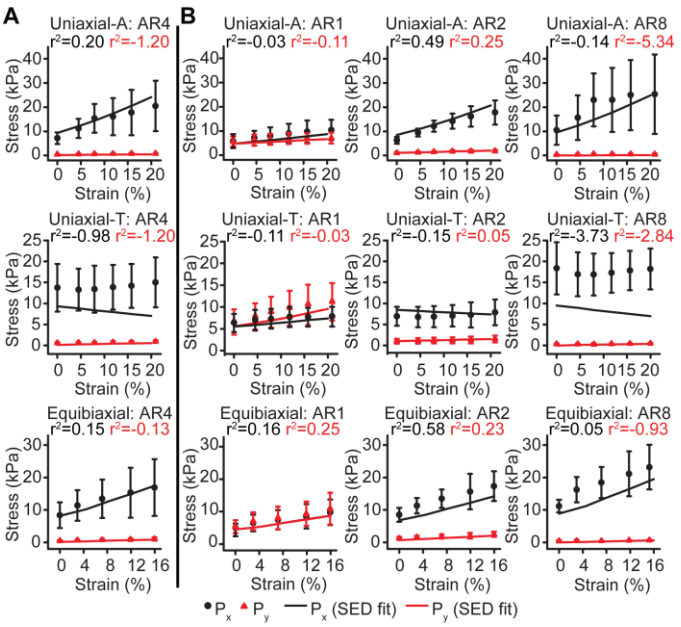

Figure 3.7. Mechanical models using actin organization-based SED recapitulate experimental results.

(A) AR4 experimental data used to determine SED parameters and planar biaxial model fit. (B) AR1, AR2, and AR8 experimental data and planar biaxial model prediction. Error bars: standard deviation.

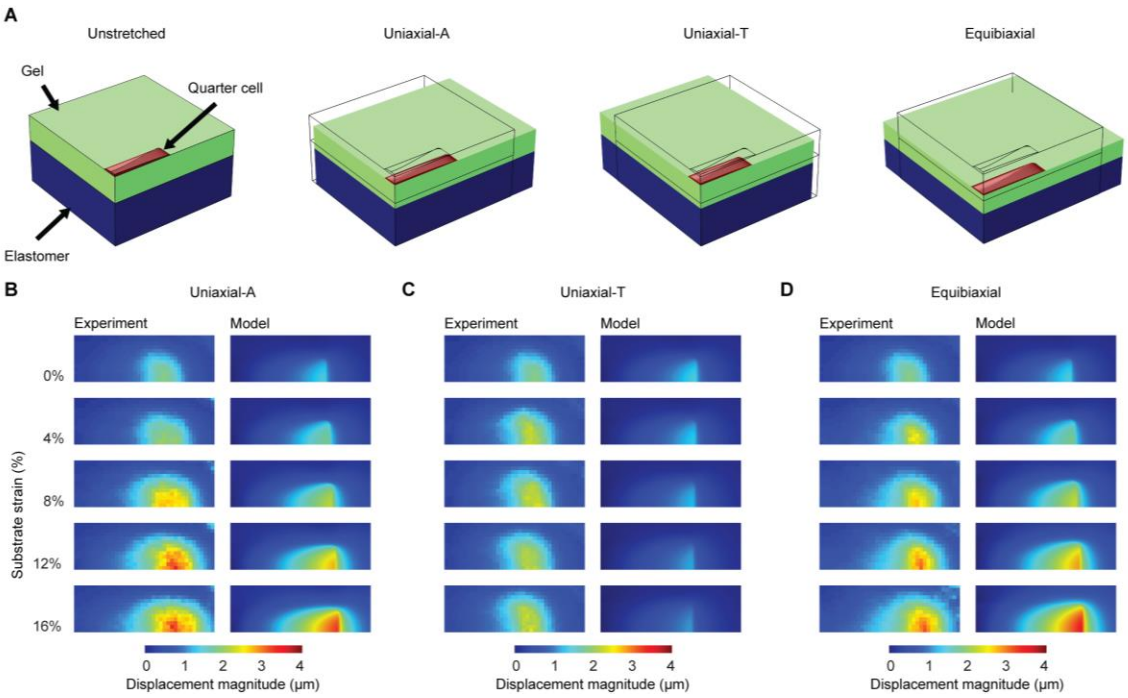

Figure 3.8. Finite element model for validating cell stretching experiment.

(A) Quarter symmetry cell and substrate model generated in COMSOL of AR4 cell undergoing prescribed uniaxial-axial, uniaxial-transverse, and equibiaxial stretch. (B-C) Comparison of model and experimental cell induced substrate displacements during (B) uniaxial-axial, (C) uniaxial-transverse, and (D) equibiaxial stretch.

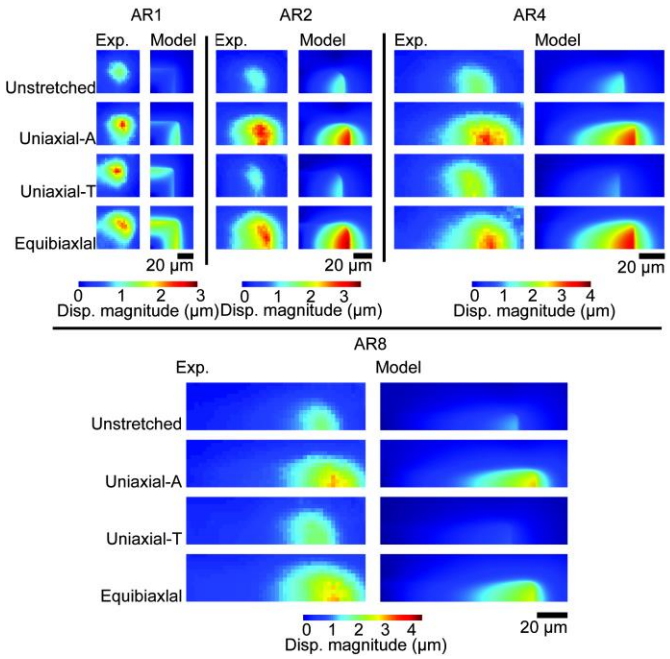

Figure 3.9. Quarter-symmetry finite element model-predicted substrate displacement compared to the mean experimental substrate displacements.

All stretched images represent 16% strain cases.

	α_{xx}	α_{yy}	α_{zz}	α_{xy}	α_{yz}	α_{zx}
AR1	0.486	0.486	0.028	0	0	0
AR2	0.846	0.126	0.028	0.023	0	0
AR4	0.928	0.044	0.028	0.010	0	0
AR8	0.945	0.027	0.028	0.011	0	0

Table 3.1. Actin fiber structure tensor values.

Cell Properties

$\mu = 0.5$ kPa, $C_f = 11.8$ kPa, $\lambda_a = 0.8$, $\kappa = 100$ kPa

Gel Properties

$E = 13.5$ kPa, $\nu = 0.49$

Membrane Properties

$E = 1.0$ MPa, $\nu = 0.49$

Table 3.2. Calculated cell properties and assumed gel and membrane properties in the model.

Chapter 4. Architecture-dependent anisotropic hysteresis in smooth muscle cells

This chapter contains unpublished material in preparation for submission to a journal.

4.1 Introduction

Recent data suggest that a cell's mechanical environment influences its function (177-179). Both static mechanical properties like substrate modulus, and dynamic mechanical load like cyclic stretching have been shown to alter gene expression and cell fate (180-183). Cells in many tissues are exposed to dynamic mechanical loading, with strain rates ranging from ~20-30%/s during cardiac contraction (184) to 10-15%/s during digestion (185) to ~1%/year during aneurysm growth (186). The precise mechanism that connects extracellular mechanical stimuli to functional changes in cell behavior is not known. One hypothesis is that forces on integrins mediate a functional response (187). It has also been hypothesized that mechanical signaling from the extracellular matrix propagates through the cell cytoskeleton from integrins to the nucleus to affect gene expression (188). Mechanosensitive ion channels have also been shown to affect cell signaling and behavior (189-191). In each case, actively adaptive cellular properties could alter mechanotransductive signaling. Previous studies have shown that cells are viscoelastic and actively contractile (192, 193). As a result, cells have time-dependent material properties. Thus, it is important to determine the dynamic material behavior of cells in mechanically responsive tissues.

Cellular viscoelastic properties have been measured using force probes such as atomic force microscopy and magnetic bead twisting microscopy (192, 194-196). The standard model for viscoelasticity assumes that cells are isotropic (195). However, recent data suggest that cells with native-like architecture, like many tissues, have anisotropic material properties (197). In addition, cells in

dynamic tissues often undergo large strains and may have nonlinear material properties (198). In tissues, large-strain viscoelastic properties are often characterized using more complex descriptions like quasi-linear viscoelasticity (QLV) (199). To date, large-strain anisotropic material properties of individual cells have not been measured. Temporal cellular contractility has been measured using many techniques including traction force microscopy (200), muscular thin films (179), and microfabricated post array devices (201), all of which measure nearly isometric tension. However, at the tissue scale, muscle contractile tone is related to the rate of change of muscle length (202). It stands to reason that a similar relationship holds at the cellular level.

In the previous work, we measured the elastic loading mechanics of contractile cells, characterized the anisotropic materials properties, and developed a strain energy density function for single cells using cellular micro-biaxial stretching (CμBS). Here, we utilized CμBS microscopy to determine loading and unloading mechanics of VSMCs over a physiological range for contractile and relaxed cells. We found that VSMCs display anisotropic hysteresis dependent on the actin fiber distribution. Finally, the experimental results were modeled with a QLV and a Hill-type active fiber model and we found that the mechanical hysteresis was better described by a Hill-type active fiber model.

4.2 Methods

4.2.1 Photolithography to fabricate PDMS stamps

Polydimethylsiloxane (PDMS) stamps were fabricated using common soft photolithography methods (95). Photomasks were designed using AutoCAD software (Autodesk, San Rafael, CA) and printed onto a Mylar film (Fineline Imaging, Colorado Springs, CO). To generate isolated single cell islands for micropatterning, features of aspect ratios (AR) 4, 2, and 1 (AR4: 32 μm x 128 μm, AR2: ,91 μm x 44 μm, AR1: 63 μm x 63 μm) were placed in arrays 200 μm

apart from other features to prevent crowding of individual features. Silicon masters were fabricated at the Minnesota Nano Center. Briefly, a clean 3.5 in silicon wafer (Wafer World Inc., West Palm Beach, FL) was primed with HMDS vapor for 3 min. Then AZ-9260 photoresist (AZ Electronic Materials USA Corp., Somerville NJ) was coated onto the wafer at 2000 rpm for 60 s (5000 rpm/s acceleration). The wafer was heated to 110 ºC on a hot plate for 165 s. The photomask and photoresist coated wafer were exposed with UV illumination for 3 cycles of 14 s each with a 10 s gap (42 s total duration) at 12 mW/cm^2 using a Karl Suss MA6 contact aligner. After exposure, the wafer was developed in a 1:4 mixture of H_2O:AZ 400k developer solution with gentle agitation for 2.5 min followed by rinsing in distilled water. Sylgard 184 PDMS was used to mold PDMS stamps from the silicon wafer. PDMS stamps were sonicated in 70% ethanol for 30 min then dried prior to use.

4.2.2 CμBS substrate fabrication

Micropatterned CμBS substrates (Fig. 4.1A) were prepared as previously described (197).

4.2.2.1 Membrane preparation

Elastomer membranes (0.01 in thick, Specialty Manufacturing, Saginaw, MI) were cut into 30 mm x 30 mm cruciform shapes and placed into custom grips (40 mm grip to grip distance) under tension. Glass slides were adhered to the bottom of the membranes to provide structural support and to prevent oxygen diffusion into the membrane. PDMS rings (30 mm diameter x 3 mm wall thickness) were bonded to the top side of the membrane to serve as a reservoir for cell culture media. Membranes were them treated with 10% w/v benzophenone (Sigma-Aldrich, St. Louis, MO) dissolved in a 70:30 solution of acetone:water for 1 min. The membranes were then rinsed with methanol and degassed in a vacuum aspirator for 30 min prior to gel polymerization.

4.2.2.2 Micropatterning

Clean PDMS stamps were incubated with 100 µg/mL of fibronectin (BD Biosciences, San Jose, CA) for 1 h then blown dry with air. O_2 plasma treated glass coverslips were then stamped with fibronectin-coated stamps and held in conformal contact for 30 min at room temperature.

4.2.2.3 Gel polymerization

Pre-polymer solution consisting of 625 µL 40% acrylamide (Sigma-Aldrich), 163 µL 2% bis-acrylamide (Sigma-Aldrich), 25 µL of 5 mg/mL acrylic acid N-hydrosuccimide ester, 35 µL 1 M HCl, and 25 µL fluorescent beads (0.2 µm red beads, 2% solids, Polysciences, Warrington, PA) was prepared and degassed for 30 min. Initiators tetramethylethylenediamine (5 µL) and 12.5 µL 10% w/v ammonium persulfate were added to the pre-polymer solution and 10 µL of the solution was deposited onto a benzophenone-functionalized elastomer substrate. The micropatterned glass coverslip was placed on the pre-polymer solution and exposed to UV illuminator in a Jelight 342 UVO cleaner for 30 min approximately 2.5 cm distance from the lamp to initiate polymerization. After gel polymerization and micropattern transfer from the coverglass to the gel, the constructs were hydrated in water for 15 min. The coverglass was peeled from the top of the gel and the glass slide was removed from the membrane. The gels were incubated in 4% bovine serum albumin in PBS to inactivate unreacted acrylic acid N-hydrosuccinimide ester. After inactivation, CµBS substrates were incubated in PBS for 48-72 h to remove residual benzophenone and unreacted pre-polymer constituents prior to cell seeding.

4.2.3 Cell culture

Human umbilical artery smooth muscle cells (VSMCs) were obtained from Lonza (Walkersville, MD) at passage 3 and only passages 4-7 were used for experiments. VSMCs were cultured at 37 ºC and 5% CO_2 in growth medium consisting of Medium 199 (GenDEPOT, Baker, TX) supplemented with 10% heat-inactivated fetal bovine serum (Gibco, Grand Island, NY), 10 mM HEPES

(Gibco), 3.5 g L^{-1} glucose (Sigma-Aldrich), 2 mg L^{-1} vitamin B12 (Sigma-Aldrich), 50 U mL^{-1} penicillin-streptomycin (Gibco), 1x MEM non-essential amino acids (Gibco), and 2 mM L-glutamine (Gibco). Cells were seeded at 10,000-20,000 cells per construct overnight in growth medium. After overnight adherence, cells were serum starved in serum free media for 24-48 h prior experiments to induce a physiological phenotype (203).

4.2.4 Cell structure measurements

Cells were fixed using 4% paraformaldehyde (Electron Microscopy Sciences, Hatfield, PA) for 5 min then stained for F-actin (Alexa Fluor 488 Phalloidin, Life Technologies, Eugene, OR). F-actin stacks (0.45 μm/slice, 20 slices) were obtained used an Olympus FluoView FV1000 BX2 laser scanning microscope (UPlanFLN, 40X, NA 1.30), at the University Imaging Centers, University of Minnesota. A custom Matlab script was used to determine average cell thicknesses to create cell thickness maps over the adhered area of the cell. Cell cross-section area was determined by integrating the cell thickness where axial cross-sectional area (A_x) was taken as the mean area over the middle 50% of the cell along the length (x-direction) and transverse cross-sectional area (A_y) was taken as the mean area over the middle 50% of the cell along the width (y-direction).

Fiber distributions measured from 2D projections of f-actin confocal stacks were fit to a von Mises distribution function of the form

$$f(\theta;\kappa,\mu) = \frac{1}{\pi I_0(\kappa)}{}^{\kappa\cos[2(\theta-\theta_p)]} \qquad [4.1]$$

where κ is the fiber concentration factor, describing the spread of the fiber distribution around preferred orientation θ_p and $I_0(\kappa)$ is the modified Bessel function of the first kind of order 0 where,

$$I_n(\kappa) = \frac{1}{\pi}\int_0^{\pi} e^{\kappa\cos(\theta)}\cos(n\theta)\,d\theta \qquad [4.2]$$

4.2.5 Cell stretching

Stretching experiments (Fig. 4.1B,C) were conducted inside a temperature controlled environmental chamber at 37 °C on an Olympus X-81 inverted microscope at 40x magnification (UPLSAPO40X2, NA 0.95). The constructs were removed from the incubator immediately prior to stretching experiments and serum free media was replaced with 2 mL of Tyrode's buffer. Cell-seeded CμBS substrates were placed into the CμBS device (Fig. 4.1A) then exposed to either uniaxial or equibiaxial stretching protocols to 25% grip strain for uniaxial or 20% grip strain for equibiaxial stretches. First, a priming stretch identical to the experimental stretch (uniaxial or equibiaxial) was performed. 3-5 cells were identified to be measured. Then cell locations were saved to Metamorph Image Acquisition software. The substrate was stretched in increments up 5% grip strain up to the maximum prescribed strain. Displaced cell positions were tracked manually and saved to the software at each step. Active cell stretch was performed by increments of 5% loading strain (0.1%/s ramp rate) to the substrate with 2 min hold periods where a brightfield image of the cell and fluorescent image of the beads in the top layer of the gel nearest to the cell were taken at each step. After reaching the maximal prescribed loading strain (25% uniaxial, 20% equibiaxial), cells were unloaded by performing -5% unloading strain to the substrate while acquiring images in the same manner as loading strain. After a full cycle of load-unload, cells were passivated with 100 μM of HA-1077 for 1 h. A full load-unload cycle was repeated on the passive cells and data required at each increment of 5% grip strain. NucBlue reagent (ThermoFisher, Waltham, MA) was used to verify micropatterned cells only had one nuclei. Finally, cells were lysed with 0.5% sodium dodecyl sulfate and the stretching protocol was repeated to acquire cell-free deformation of beads. Substrate deformations due to applied grip strains were calibrated by measuring displacement of beads during cell-free deformation of the substrate. Substrate stretch ratios, λ_x and λ_y, were taken as the measured cell-free substrate deformations.

4.2.6 Calculation of traction forces and cell stress

A particle image velocimetry (PIV) algorithm was used to calculate bead displacements at the top surface of the gel by comparing relative bead displacements between cell and cell-free image pairs (Q Tseng et al). Final PIV windows were sampled every 2.5 μm using 5x5 μm^2 grids. Traction stress vectors were determined from bead displacements using an unconstrained Fourier transform traction cytometry algorithm (regularization factor: 1E-9, Poisson's ratio: 0.5), yielding a grid of n substrate traction stress vectors given by $\boldsymbol{T^n} = T_x^n \boldsymbol{e_x} + T_y^n \boldsymbol{e_y}$ where $\boldsymbol{e_i}$ is the unit vector in the i direction. The total traction force components f_x and f_y are given as $f_i = \sum_n - T_x^n A^n \frac{r_i^n}{|r_i^n|}$ where $i = x, y$, A^n = 6.25 μm^2 is the area of discrete surface n, and $\boldsymbol{r^n} = r_x^n \boldsymbol{e_x} + r_y^n \boldsymbol{e_y}$ is the vector that described the location of surface n with respect to the cell center. The first Piola-Kirchhoff (PK1) stresses (Fig. 4.1D) P_x and P_y were calculated as $P_x = \frac{f_x}{2A_x}$ and $P_y = \frac{f_y}{2A_y}$.

4.2.7 Modeling cell hysteresis

Two models were used to describe cell biaxial hysteresis: a quasi-linear viscoelastic model and a Hill-type active fiber model.

4.2.7.1 Deformation and elastic constitutive description

The cell was assumed to undergo isochoric planar biaxial deformation (i.e. no shear). The deformation tensor $\mathbf{F} = \mathrm{diag}[\lambda_x, \lambda_y, \lambda_z]$ was taken as the observed deformation of the cell, where λ_i are stretch ratios in the i direction (Fig. 4.2A, x: parallel to the long of the cell, y: parallel to the short axis of the cell, z: perpendicular to the gel surface). Temporal stretch ratios mimicked those of the experiments. For equibiaxial stretching, both λ_x and λ_y were stretched by strain increments of 4% strain, at a strain rate of 0.5%/s, with a resting period of 2 min at each strain increment. The maximum strain was 16% strain. Uniaxial

stretching was performed by applying 4.5% strain increments in the direction of stretch and -1% off-axis strain, at a strain rate of 0.5%/s, with a resting period of 2 min at each increment. The maximum strain was 22.5% strain. For all deformations, $\lambda_z = (\lambda_x \lambda_y)^{-1}$

In both models, the cell was treated as a distribution of pre-strained discrete acto-myosin fibers within an isotropic bulk matrix. The constitutive equation for the matrix was taken as neo-Hookean and given by

$$W_b = \frac{\mu}{2}(I_1 - 3) \qquad [4.3]$$

where μ is shear modulus and $I_1 = \lambda_x^2 + \lambda_y^2 + \lambda_z^2$ is the first strain invariant. The constitutive equation a fiber was given by

$$W_f = \frac{C_f}{2}\left(\left(\frac{\lambda_f}{\lambda_a}\right)^2 - 1\right)^2 \qquad [4.4]$$

where C_f is a fiber stiffness parameter, λ_f is the fiber stretch ratio, and λ_a is an active stretch ratio that defines the stretch between the actively contracted zero-stress fiber length and passive zero-stress fiber length (46). The deformation of a fiber oriented with an angle θ from the x-axis of the cell was given by

$$\lambda_f^2 = \lambda_x^2 \cos^2\theta + \lambda_y^2 \sin^2\theta$$

The total strain energy density function of a cell with n fibers was then given by

$$W = W_b + \frac{1}{n}\sum_{i=1}^{n} W_{fi} \qquad [4.5]$$

The elastic 1st Piola-Kirchhoff stress in the i direction is given by

$$P_i^e = \frac{\partial W}{\partial \lambda_i} - \frac{\lambda_z}{\lambda_i}\frac{\partial W}{\partial \lambda_z} \qquad [4.6]$$

where $i = x, y$.

4.2.7.2 Quasi-linear viscoelastic model

We modeled cell hysteresis as temporal viscoelastic relaxation using a Fung-type quasi-linear viscoelastic (QLV) model (199). The temporal stress was given as

$$P_i(t) = P_i^e(0)G(t) + \int_0^t G(t-\tau)\frac{\partial P^e[\boldsymbol{F}(\tau)]}{\partial \tau}d\tau \qquad [4.7]$$

where $G(t)$ is the reduced relaxation function. The general form for $G(t)$ is $G(t) = \frac{\sum_i \alpha_i e^{-\beta_i t}}{\sum_i \alpha_i}$. For simplicity, we used a first order function given by

$$G(t) = \alpha + (1-\alpha)e^{-\beta(t)} \qquad [4.8]$$

where α and β are constants.

4.2.7.3 Hill-type active fiber model

We modeled cell hysteresis as active contraction by modeling the acto-myosin fibers with the Hill equation for muscular contraction (202). A standard form of the Hill equation is given by

$$V = \frac{b(F_o - F)}{F + a} \qquad [4.9]$$

where V is velocity of shortening of the muscle fiber, F is the force on the muscle, F_o is the maximum force at which a tetanized muscle neither shortens nor lengthens ($V = 0$), and b and a are constants. Here, we aimed to replace the shortening velocity with the rate of change of the fiber zero-stress configuration, characterized in our framework as λ_a. The stretch ratio of the fiber (λ_f) is decomposed into λ_a and the elastic deformation λ^*, such that

$$\lambda_f = \lambda^* \lambda_a \qquad [4.10]$$

Thus, the fiber shortening velocity is given by

$$V = -\frac{d\lambda_f}{dt} = -\frac{d\lambda_a}{dt}\frac{\lambda_f}{\lambda_a} = -\frac{\dot{\lambda_a}}{\lambda_a}\lambda_f \qquad [4.11]$$

The fiber force is given by

$$F = P_f A \qquad [4.12]$$

where P_f is the First Piola-Kirchhoff stress in the direction of fiber orientation, and A is the undeformed cross-sectional area of the fiber. The fiber stress at the beginning of the experiment, when the cell is maintaining homeostatic stretch, is given by P_o, which is defined by

$$P_o = P(\lambda_{ao}) = \frac{F_o}{A} \qquad [4.13]$$

where λ_{ao} is the initial homeostatic stress-free shortening.

Substituting equations [10-13] into [9] gives

$$\frac{\dot{\lambda}_a}{\lambda_a} = \frac{b(P_f - P_0)}{\lambda_f(P_f + a_0)} \qquad [4.14]$$

where a_o and b are constant parameters.

4.2.7.3. Solution method

In both models, a random family of 2000 fibers, matching the measured von Mises distribution measured of an average cell, was generated. Time was discretized into 0.01 min increments over 18 min for equibiaxial stretch and 22 min for uniaxial stretch. Initially, $\lambda_x = \lambda_y = \lambda_z = \lambda_f = 1$. Parameters were fit to the equibiaxial data via least-squares fitting of the experimentally-measured stresses (both P_x and P_y) and the mean model-predicted stresses during each stretch hold period at each of the measured substrate deformations $\lambda = [1.00, 1.04, 1.08, 1.12, 1.16]$. The parameter range that was considered was: $\mu = 0.5 - 4\ kPa,\ C_f = 1 - 5\ kPa,\ \lambda_{a0} = 0.6 - 0.75,\ \alpha = 0.8 - 0.95,\ \beta = 0.1 - 0.4,$

$a_0 = 1 - 10\ kPa$, and $b = 0.005 - 0.05$. After parameter optimization, uniaxial stresses for corresponding uniaxial-axial or uniaxial-transverse stretches were then computed using the fitted parameters by applying experimental measured substrate deformations $\lambda = [1.00, 1.045, 1.09, 1.135, 1.18, 1.225]$ in the direction of stretch and $\lambda = [1.00, 0.99, 0.98, 0.97, 0.96, 0.95]$ in the off-axis direction.

4.2.8. Statistics

All results are expressed as means ± standard deviation. Differences in loading and unloading stresses for at each strain for all stretching experiments were compared using paired t-tests in SigmaPlot (Systat Software Inc, San Jose, CA). A value of $p<0.05$ was considered to indicate statistical significance.

4.3 Results

4.3.1. Micropatterned vascular smooth muscle cells display anisotropic hysteresis

We utilized CμBS microscopy to apply physiological strains (~20-25% strain) to individual adherent VSMCs (Fig. 4.1) and measure the resulting stresses. VSMCs were micropatterned into a physiological aspect ratio of 4 to mimic an *in vivo*-like spindle geometry on an elastomer membrane. Next, we applied planar strains in increments of 5% grip strain up to 20% or 25% then incrementally returned to 0% strain. When exposed to stretch, cell geometry in the x-y plane, increased with applied load then decreased with unloading as expected (Fig. 4.2A), consistent with membrane deformations. Traction stress was measured using the displacement of the substrate during stretching and traction force microscopy methods. Traction stress magnitudes increased accordingly with applied equibiaxial stretch and decreased with stretch (Fig. 4.2A). Axial stress (P_x) (parallel to the long axis of the cell) and transverse stress (P_y) (parallel to the short axis of the cell) were calculated from traction forces exerted by the cell on the substrate (Fig. 4.1D) and the cellular architecture

determined from confocal microscopy (197). In a typical cell, axial stresses were an order of magnitude higher than transverse stresses (Fig. 4.2B, C), consistent with previous findings (197). In addition, stresses were dissimilar during loading and unloading, demonstrating stress is not only a function of strain.

Under equibiaxial loading, P_x and P_y increased linearly when loaded and decreased when unloaded (Fig. 4.3C, D) with unloading stresses lower than loading stresses. These data are consistent with hysteresis loops traditionally associated with viscous loss. There is significant cell-to-cell variability in baseline stress, but if the data are normalized to the stress at maximum strain and examined individually, the consistency of the hysteresis is clearer (see supplemental Fig. 4.1). Next, the same cells were treated with HA-1077, a ROCK inhibitor that inhibits acto-myosin contractility. Following treatment, the stresses decreased by >10 fold (Fig. 4.3E, F) and the degree of hysteresis decreased (see supplemental Fig. 4.1).

Next, we applied uniaxial deformation, stretching either parallel to the cell's long axis (uniaxial-axial) (Fig. 4.4A) or parallel to the cell's short axis (uniaxial-transverse). Notably, the deformation is not purely uniaxial. When we applied uniaxial-axial deformation (λ_x), we observed some compression in the transverse direction (λ_y) (Fig. 4.4B). For uniaxial-axial stretching, P_x (stress in the direction of stretch) and P_y (stress in the off-axis direction) increased with strain (Fig. 4.4C, D) and unloading stresses were lower than loading stresses for each increment of strain, suggesting energy loss, similar to our equibiaxial stretch experiments. Inhibiting acto-myosin contractility decreased stresses by almost 10-fold (Fig. 4.4E, F) and decreased the degree of hysteresis. When we performed uniaxial-transverse stretching (Fig. 4.5A), we observed a slight compression in the x direction (λ_x) with applied loading in the transverse direction (λ_y) (Fig. 4.5B). For uniaxial-transverse stretching, P_y (stress in the direction stretch), increased during loading and decreased with unloading (Fig. 4.5D). This trend is quite clear in normalized individual cell data (see supplemental Fig. 4.1). Surprisingly, unloading stresses were greater than loading stresses, suggesting

energy gain. Stresses perpendicular to the direction of stretch, P_x, were nearly unchanged during loading but increased during unloading (Fig. 4.5C). When contraction was inhibited, passive stresses were markedly lower than contractile stresses (Fig. 4.5E, F) but we observe significant differences in loading and unloading stresses for both P_x and P_y. Notably, the hysteresis in P_x (Fig. 4.5E) is reversed in the passive state, compared to the active, with unloading stresses lower than loading stresses.

4.3.2. Quasilinear viscoelastic and Hill-type active fiber modeling of equibiaxial and uniaxial stretch

To better understand the dynamics of the observed anisotropic hysteresis, we developed two theoretical models: a QLV (Eqn. 4.7) and Hill-type active fiber model (Eqn. 4.14). The apparent hysteresis observed in the cells was first modeled with a quasilinear viscoelastic model. For the elastic properties, we used a strain energy density function we previously characterized. For the viscous behavior we used a reduced relaxation function with an exponential decay (Eqns. 4.8). The parameters were fit to the equibiaxial stretching data (see Fig. 4.3C, D) (see Table 4.1). After fitting, the model results (Fig. 4.6A) were consistent with the experimentally observed hysteresis for P_x and P_y in equibiaxial stretching. Next, the model was applied to the uniaxial-axial and uniaxial-transverse stretch cases. For uniaxial-axial stretching, the model (Fig. 4.6B) captured the hysteresis behavior from the experiment, where unloading stresses are lower than loading stresses for each point of strain for P_x and P_y. In the case of the uniaxial-transverse stretch, however, the model failed to predict the observed reverse hysteresis (see Fig. 4.5C, D), instead predicting unloading stresses lower than loading stresses for P_x and P_y (Fig. 4.6C).

Next, the cell was modeled with an active contraction model that assumes a Hill-type relationship between acto-myosin fiber stress and contraction velocity. Equibiaxial experimental data (see Fig. 4.3C, D) were used to optimize the parameters (see Table 4.2). The model stress-strain behavior (Fig. 4.6D) was

consistent with the experimentally observed hysteresis for P_x and P_y in equibiaxial stretching. The model was then applied to uniaxial-axial or uniaxial-transverse stretch. For uniaxial-axial stretch, the model hysteresis (Fig. 4.6E) was consistent with the experimentally observed behavior (see Fig. 4.4C, D). Additionally, for uniaxial-transverse stretch, the model predicted reverse hysteresis, where unloading stresses are higher than loading stresses (Fig. 4.6F), seen experimentally (see Fig. 4.5C, D). Given this result, our subsequent work focused on our Hill-type active fiber model.

4.3.3. Fiber orientation influences hysteresis anisotropy

VSMCs normally have a highly aligned acto-myosin cytoskeleton (39). However, in vessels with complex geometries, and in aneurysms, they can lose their characteristic spindle shape and, as a result, their cytoskeletal alignment (204). Using our Hill-type active fiber model, we tested how cytoskeletal alignment alters the dynamic mechanics of the cells. We assumed that acto-myosin fiber alignment could be fit to a von Mises distribution and we performed a parameter study for fiber alignment characterized by the fiber concentration factor (κ) over a range of κ values from an isotropic (κ =0) value to a highly anisotropic value (κ =50). Uniaxial-axial and uniaxial-transverse stretch were simulated. For uniaxial-axial stretch, higher stresses in the direction of stretch, P_x, were observed with increasing fiber alignment (increasing κ) (Fig. 4.7A). Notably, the degree of hysteresis increased (i.e. larger loops) with increasing fiber alignment. Stresses transverse to cell alignment, P_y, decreased with increasing anisotropy (Fig. 4.7A) due to lower fiber alignment in that direction. For uniaxial-transverse stretch, increasing anisotropy led to lower stresses in the stretch direction (P_y) (Fig. 4.7B). Interestingly, below values of $\kappa < 4$, the hysteresis loop displayed a normal dissipative behavior, but for $\kappa > 4$, the reverse hysteresis we observed experimentally was predicted. In the direction of cell alignment, higher stresses and a higher degree of hysteresis were observed with increasing anisotropy (Fig. 4.7B). For a completely isotropic fiber distribution (κ = 0), stretch direction does not affect the hysteresis direction (Fig. 4.7A, B).

However, for values of $\kappa > 0.05$, the reverse hysteresis behavior was observed in the axial stresses during transverse stretch (Fig. 4.7B), suggesting cytoskeletal anisotropy plays an important role in the stress hysteresis of VSMCs.

Finally, cells were micropatterned with smaller aspect ratios (AR2, AR1) but similar spread areas, which has been previously shown to result in more isotropic cytoskeletal alignment. F-actin fiber distributions were measured from confocal imaging (Fig. 4.8A) and fit with von Mises distributions. The fiber concentration factors were: κ = 7.65 and κ = 0.15 for AR2 and AR1, respectively (Fig. 4.8B). AR2 cells were stretched using the previously described uniaxial-axial and uniaxial-transverse protocols and showed results consistent with the AR4 cells and the model predictions, where axial stretch parallel to fiber alignment displays normal hysteresis (Fig. 4.9A), while transverse stretch perpendicular to fiber alignment displays reverse hysteresis (Fig. 4.9B). Uniaxial stretching performed on the AR1 cell (Fig. 4.9C), mimicking an isotropic fiber distribution (κ = 0.15), showed normal hysteresis independent of stretch direction consistent with model predictions.

4.4 Discussion

It is increasingly clear that mechanical stresses play an important role in regulation of cellular function. Thus, it is important to understand how cell stresses relate to cell deformations, particularly in mechanically dynamic tissues. Here, using the CμBS method, we investigated loading and unloading dynamics of individual VSMCs exposed to large-strain biaxial stretching. We found that AR4 VSMCs exhibit hysteresis behavior during loading and unloading when stretched in the direction of primary fiber alignment, suggestive of viscous energy loss. Interestingly, when stretched transverse to fiber alignment, AR4 VSMCs exhibited reverse hysteresis with unloading stresses greater than loading stresses, suggestive of energy gain. We also found that this phenomenon was particular to anisotropic cells. In cells with more isotropic cytoskeletal organization, reverse hysteresis was not observed. We found that a standard

QLV model was not able to describe the reverse hysteresis we observed in AR4 cells undergoing transverse stretch, but our Hill-type active fiber model was able to characterize the anisotropic hysteresis behavior observed in the experiment. These results suggest that viscoelastic models are insufficient for modeling highly structured cells, like muscle cells, under multidirectional loading.

In the Hill-type active fiber model, we assume that all fibers are at a homeostatic stress (P_0), or stall force, prior to stretch. When a fiber is stretched, its stress rises above P_0 and, by Eqn. 4.14, the fiber relaxes by lengthening its zero-stress configuration (λ_a). Conversely, when a fiber is compressed, the fiber contracts, raising fiber tension. In highly anisotropic cells, the fibers that provide tension in the cells' short axis are still primarily aligned with the cell's long axis. Thus, when the cell is stretched transversely and shortens somewhat axially, the fibers contract. In smooth muscle, contraction and relaxation are slow, so when the cell is unloaded the fiber tension remains elevated. This phenomenon can be captured with the simple model presented here. However, to our knowledge, this reverse hysteresis has not been measured previously.

There are several limitations in our measurement of viscoelastic properties in our experiment. Primarily, *in vivo* strain rates for arteries and aortas occur on the scale of 0.25-3%/s (205, 206) while in the experiment we perform a slower global stretch, taking into account stretching and imaging time, at <0.1%/s (or 0.5%/s during actual stretch) due to temporal limitations during imaging which limits the temporal resolution of strain application and of cell stress measurement. In addition, cells are exposed to continuous cyclic stretch and *in vitro* studies have shown dynamic mechanical strain application of cells and tissues are prone to mechanical conditioning (207-209). We perform, effectively two conditioning stretches in the processes of a priming stretch and identification of cells for study, but did not investigate the ability of the cells to adapt to cyclic stretch or further conditioning stretches. In the model, we treat the cell as a bulk neo-Hookean matrix with discrete actin fibers oriented with a defined distribution. We neglect other cellular components such as the nucleus and mechanical

properties of other cytoskeletal filaments such as microtubules and intermediate filaments. However, our drug studies inhibiting acto-myosin contractility eliminates nearly all tension in the cell, so it is likely assuming actin fibers are the primary cytoskeletal filament is valid. Nevertheless, it has been shown that the nucleus displays viscoelastic properties (176, 210) as well as microtubules (211, 212). Coupling of actin fibers to the nucleus and other cytoskeletal filaments could also play a role in the viscoelastic properties of the cell. We model the observed hysteresis in the cell using either a passive relaxation QLV model or a Hill-type active fiber model. Both models rely on empirical observations of mechanical behavior of tissues. QLV theory describes passive relaxation of tissues dependent on time. Hill observed the velocity of shortening of muscle varies with applied load on the muscle. Applied to our case, the rate of stress-free shortening of the fibers vary with load. In reality, a model coupling passive relaxation and active contraction remodeling is necessary to truly mimic the dynamics of the cell.

Modern biomechanical models such as constrained mixture models (7, 213) require a firm understanding of the mechanical properties of each component of tissues. Vascular tissues, whole arteries and isolated decellularized ECM components (collagen, elastin, etc.) are well studied and their mechanics under large strain loading and unloading conditions are well-characterized (214, 215). Mechanics of individual cells have been studied using a variety of tools including but not limited to micropipette aspiration, microrheology, magnetic bead twisting, atomic force microscopy, optical tweezers, and microfluidics (26). These measurements normally yield parameters for isotropic linear materials. Our results suggest linear isotropic properties and simple viscoelastic models are insufficient for describing cells under biaxial loads. This finding is particularly notable in the development of mixture models of vascular mechano-adaptations, which have potential clinical applications predicting, for example, aneurysm growth and rupture. Cells in bifurcations or in aneurysms are necessarily exposed to complex loads and models that cannot capture the

anisotropic time-dependent and architecture-dependent material behavior of the cells will be less accurate.

The field of mechanotransduction, how cells sense and integrate external mechanical stimuli to alter cell behavior, has appreciated in recent years. Current efforts are ongoing towards the exact mechanisms that underlie mechanotransduction processes. Many studies are performed in static culture or at small strains but cells are exposed to complex dynamic loading *in vivo* and can take on varieties of architectures the 3D environment. In efforts to dissect mechanotransductive mechanisms, micropatterning approaches have been used to yield consistent cell geometries for direct cell comparison and to enforce architecture control to study cell behavior response. To study the effects of adaptive responses of cells to complex loads, it is necessary to use appropriate measurement tools and to precisely control strain. By applying uniaxial strains up to 10% to single cells, reports show cells respond to mechanical loads and respond accordingly. In their response, the cell's time-dependent mechanical properties are dependent on both strain magnitude (148) and strain rate (216). Not only that, Bonakdar et al (217) have shown that the cell cytoskeleton undergoes both elastic and plastic deformation in response to mechanical stretch. In addition, Weng et al (201) suggest focal adhesion dynamics drive cellular homeostasis after strain application. While, these studies have been performed on isolated single cells, Canovic et al. (200) further suggest tensional homeostasis of static cells is a multi-cellular phenomenon where mechanical coupling of adjacent cells can affect cluster force measurements, suggesting cells' interactions with neighbor cells can also affect their mechanical response. With varying reports of cellular response to loads, many of these studies are based on empirical observations of cells mechanical responses and outputs. While precise mechanisms of cellular adaptation to mechanical loads are not known and a more comprehensive view is still lacking, it is clear that contractile mechanisms play a critical role and models incorporating acto-myosin contraction will be vital in characterizing cell mechanics (218). In this paper, we utilized

CμBS microscopy, to apply precise multi-directional physiological large strains to *in vivo*-like cells to investigate their mechanical response to stretch. We show that cell shape and resulting fiber architecture plays a role in its mechanical response to stretching. We report, to our knowledge, the first case of hysteresis anisotropy of a single cell. Our results and models provide insight into a possible mechanism of active cellular adaptation of vascular smooth muscle cells in response to complex strains.

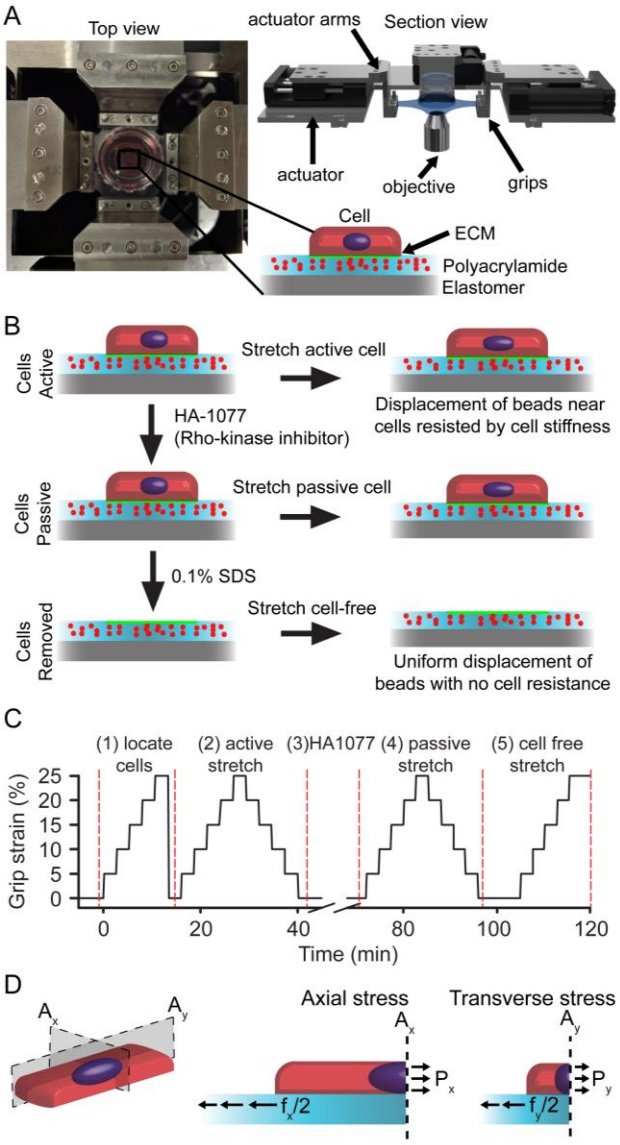

Figure 4.1. Cellular micro-biaxial stretching (CμBS) method to measure active and passive cell stress

(A) Schematic of CμBS device and substrate. Top view: photograph of substrate mounted in device. Inset: Micropatterned cell polyacrylamide-elastomer substrate. Side view: Rendered image of device. (B) Stretch protocol to measure substrate bead displacements in active and passive cells. (C) Time course of stretch protocol to stretch active and passive cells. (D) Cell axial and transverse stress calculation from substrate traction forces.

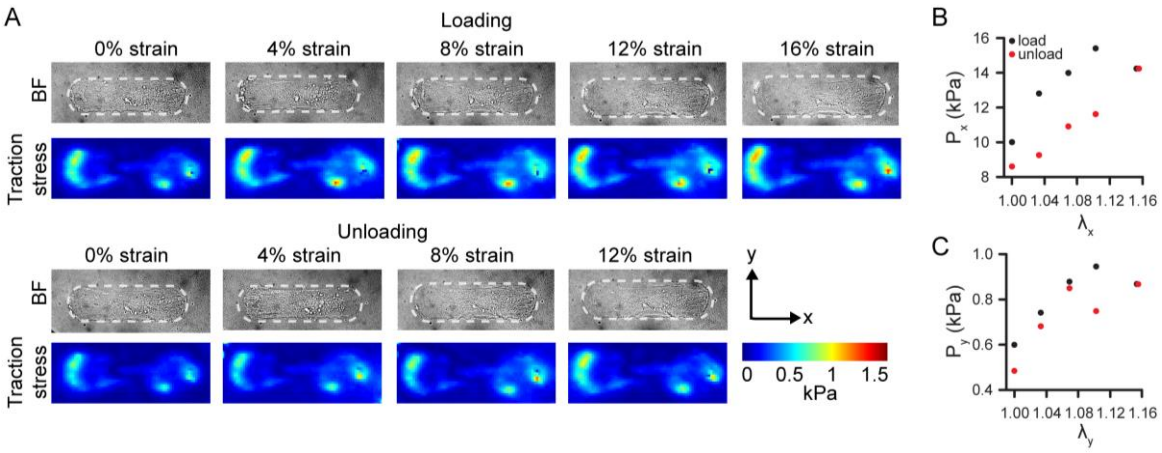

Figure 4.2. Equibiaxial stretch of a micropatterned VSMC

(A) Brightfield images and traction stress fields of a stretch cycle (0% → 16% → 0%). Cell outlined in white.(B) Axial cell stress (P_x) during equibiaxial stretch. (C) Transverse cell stress (P_y) during equibiaxial stretch.

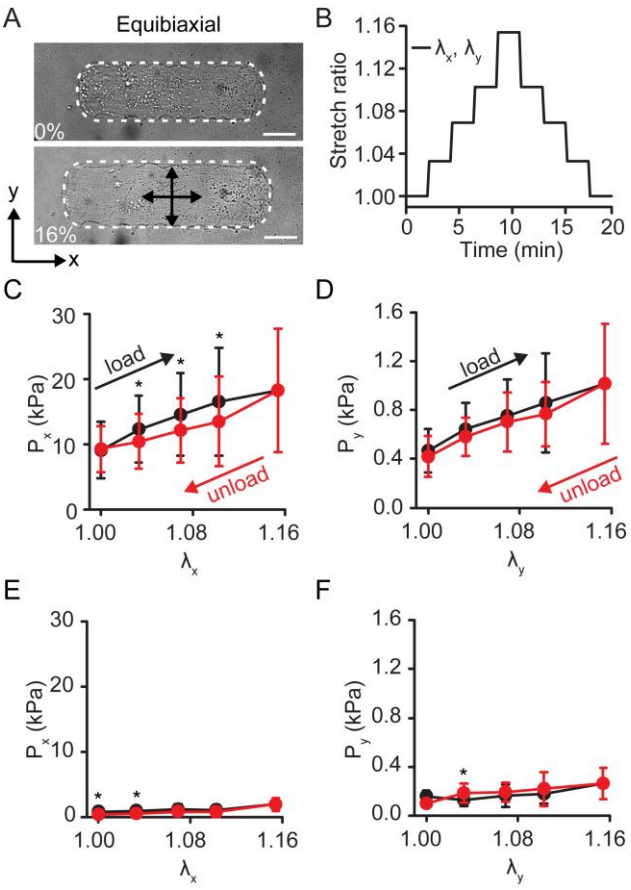

Figure 4.3. Active and passive loading and unloading stresses of a vascular smooth muscle cell undergoing equibiaxial stretch

(A) Brightfield image of cell before and after 16% stretch (x,y-equibiaxial stretch, $\lambda_x=\lambda_y$). Cell outlined in white. Scale bars: 20 μm. (B) Cell stretch ratio (λ_x, λ_y) during equibiaxial stretch cycle. (C) Axial active cell stresses (P_x) during equibiaxial stretch. (D) Transverse active cell stresses (P_y) during equibiaxial stretch. (E) Axial passive cell stresses (P_x) during equibiaxial stretch. (F) Transverse passive cell stresses (P_y) during equibiaxial stretch. (C-F) (mean ± stdev) n=10. *=p<0.05. Black: loading. Red: unloading.

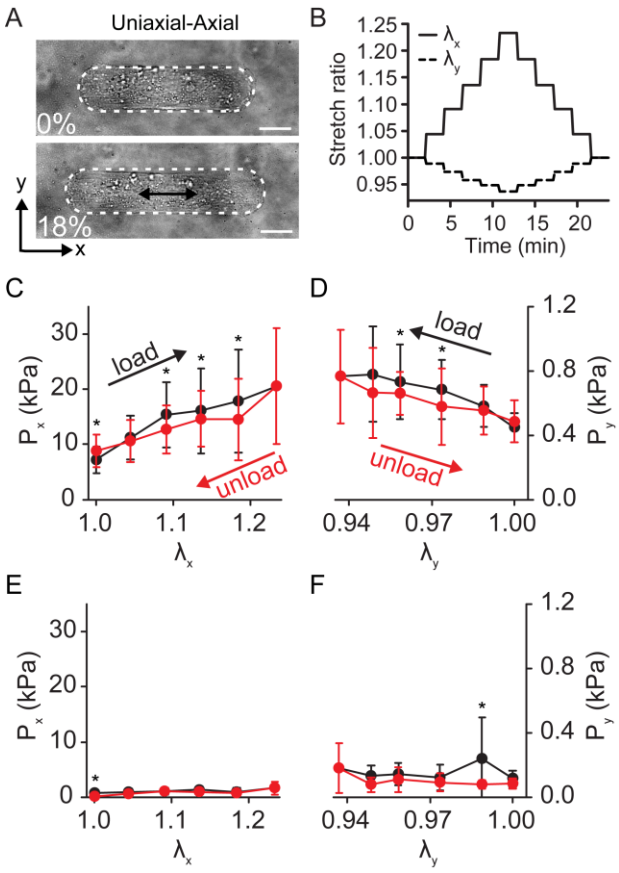

Figure 4.4. Active and passive loading and unloading stresses of a vascular smooth muscle cell undergoing uniaxial-axial stretch

(A) Brightfield image of cell before and after 16% stretch (x-direction of stretch, λ_x). Cell outlined in white. Scale bars: 20 μm. (B) Cell stretch ratio (λ_x, λ_y) during uniaxial-axial stretch cycle. (C) Axial active cell stresses (P_x) during uniaxial-axial stretch. (D) Transverse active cell stresses (P_y) during uniaxial-axial stretch. (E) Axial passive cell stresses (P_x) during uniaxial-axial stretch. (F) Transverse passive cell stresses (P_y) during uniaxial-axial stretch. (C-F) (mean ± stdev) n=10. *=$p<0.05$. Black: loading. Red: unloading.

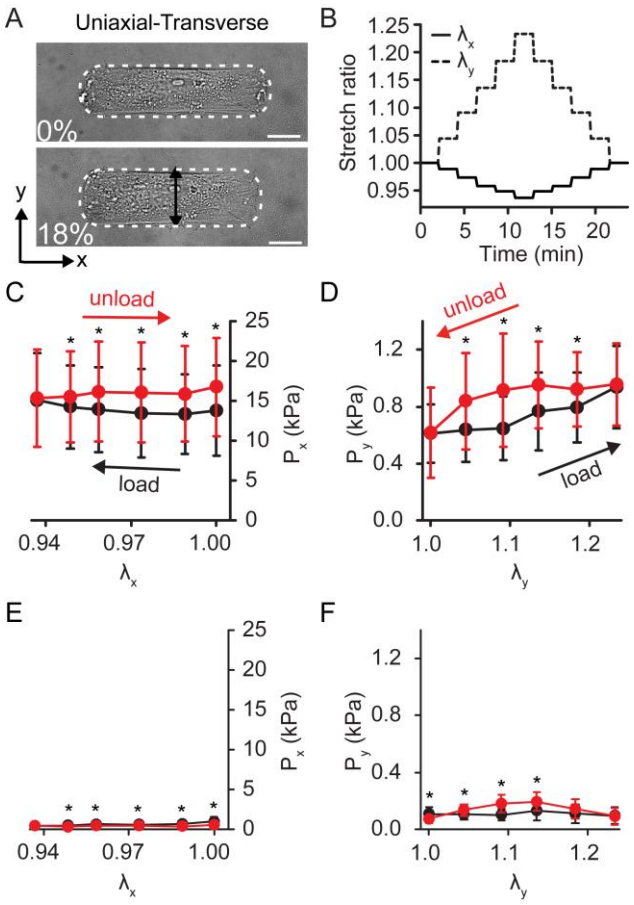

Figure 4.5. Active and passive loading and unloading stresses of a vascular smooth muscle cell undergoing uniaxial-transverse stretch

(A) Brightfield image of cell before and after 16% stretch (y-direction of stretch, λ_y). Cell outlined in white. Scale bars: 20 μm. (B) Cell stretch ratio (λ_x, λ_y) during uniaxial-transverse stretch cycle. (C) Axial active cell stresses (P_x) during uniaxial-transverse stretch. (D) Transverse active cell stresses (P_y) during uniaxial-transverse stretch. (E) Axial passive cell stresses (P_x) during uniaxial-transverse stretch. (F) Transverse passive cell stresses (P_y) during uniaxial-transverse stretch. (C-F) (mean ± stdev) n=10. *=p<0.05. Black: loading. Red: unloading.

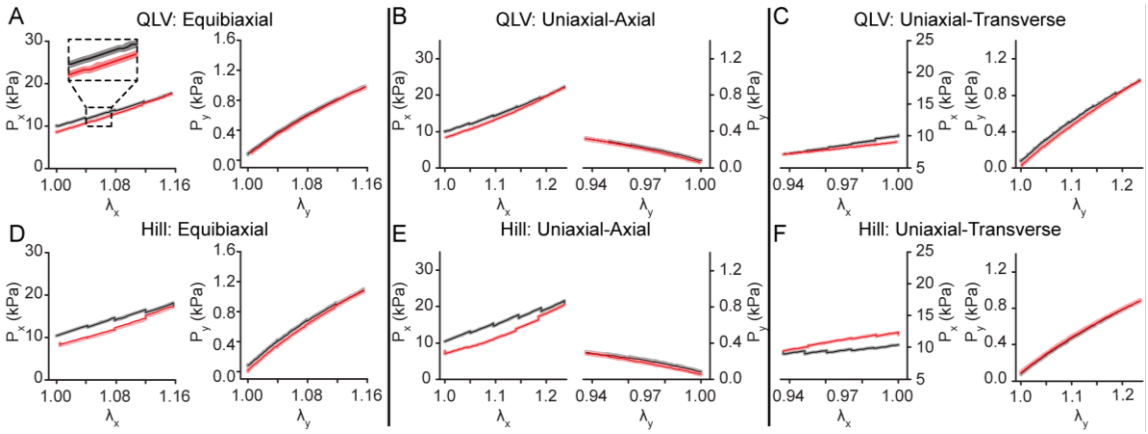

Figure 4.6. Modeling hysteresis in vascular smooth muscle cells

(A) QLV model fits to experimental data. Inset: zoomed image of plot showing average stresses and all model computed values. (B) QLV model predictions for uniaxial-axial stretch. (C) QLV model predictions for uniaxial-transverse stretch. (D) Hill-type active fiber model fits to experimental data. (E) Hill-type active fiber model predictions for uniaxial-axial stretch. (F) Hill-type active fiber model predictions for uniaxial-transverse stretch. Black solid lines: average loading stresses over 100 runs. Red solid lines: unloading stresses over 100 runs. Shaded regions indicate all model computed values.

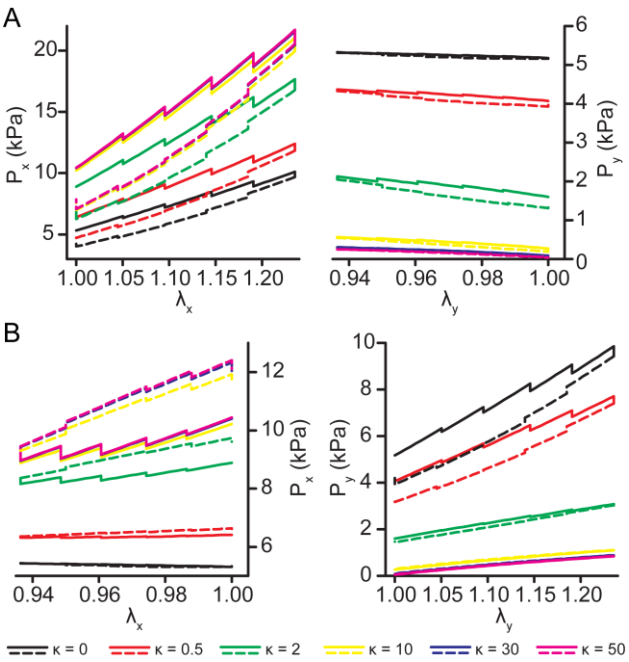

Figure 4.7. Hill-type active fiber model fiber concentration parameter study for uniaxial stretch

(A) Uniaxial-axial stretch model predictions for fiber concentration factor values $\kappa = 0, 0.5, 2, 10, 30, 50$. Left: axial stresses ($P_x$) due to applied axial strain (λ_x). Right: Transverse stresses (P_y) due to off-axis strain (λ_y). Solid lines: loading stresses. Dashed lines: unloading stresses. (B) Uniaxial-axial stretch model predictions for fiber concentration factor values $\kappa = 0, 0.5, 2, 10, 30, 50$. Left: transverse stresses (P_y) due to applied axial strain (λ_y). Right: axial stresses (P_x) due to off-axis strain (λ_x). Solid lines: loading stresses. Dashed lines: unloading stresses.

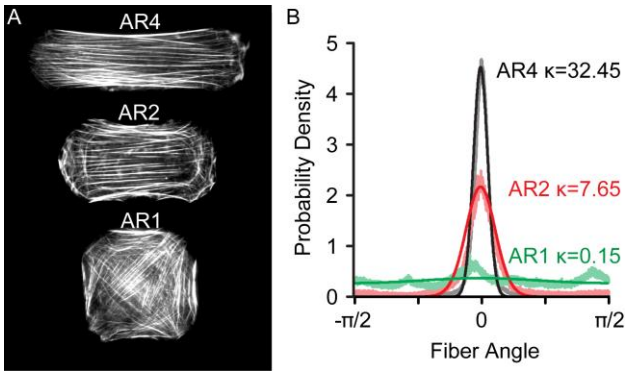

Figure 4.8. Cell micropatterning and measured von Mises fiber distributions

(A) F-actin immunofluorescent images of cells micropatterned with aspect ratios of 4, 2, and 1. (B) Measured fiber distribution (translucent lines) and von Mises distribution fits (solid lines).

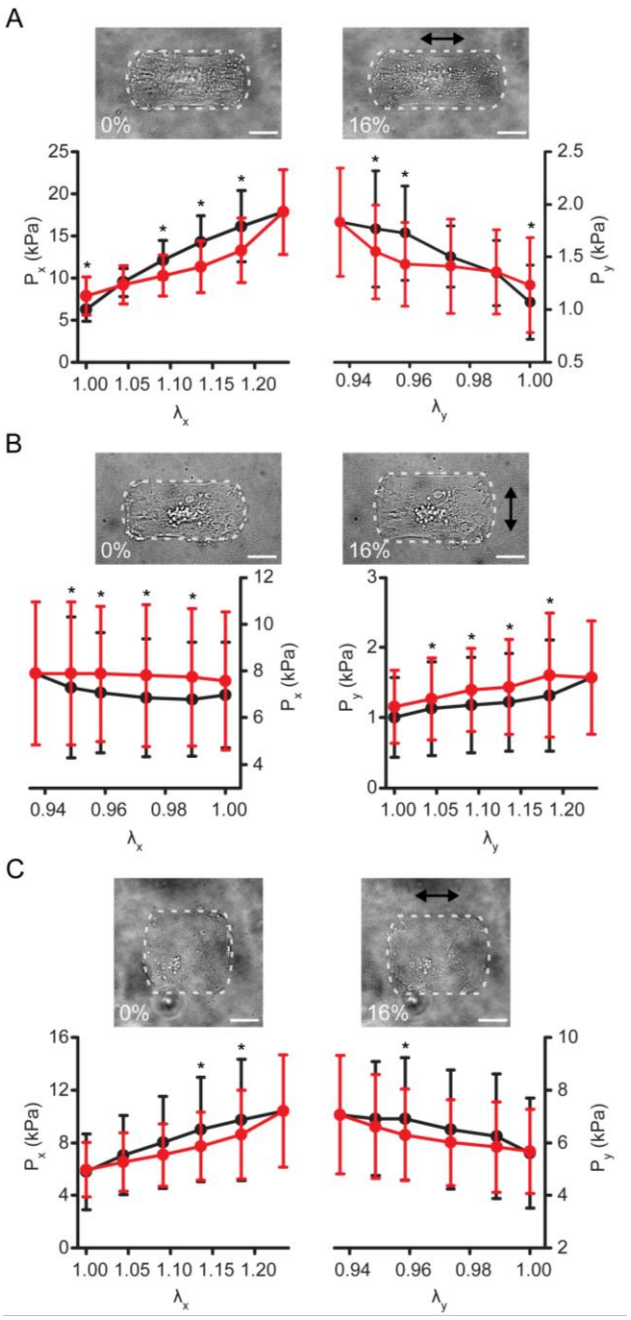

Figure 4.9. Cell shape mediates hysteresis anisotropy

(A) Axial (P_x) and transverse (P_y) stresses for an aspect ratio 2 cell ($\kappa = 7.65$) stretched uniaxial-axially. (B) Axial (P_x) and transverse (P_y) stresses for an aspect ratio 2 cell ($\kappa = 7.65$) stretched uniaxial-transversely. (C) Axial (P_x) and transverse (P_y) stresses for an aspect ratio 1 cell ($\kappa = 0.15$) stretch uniaxially. (A-C) Scale bars: 20 μm.

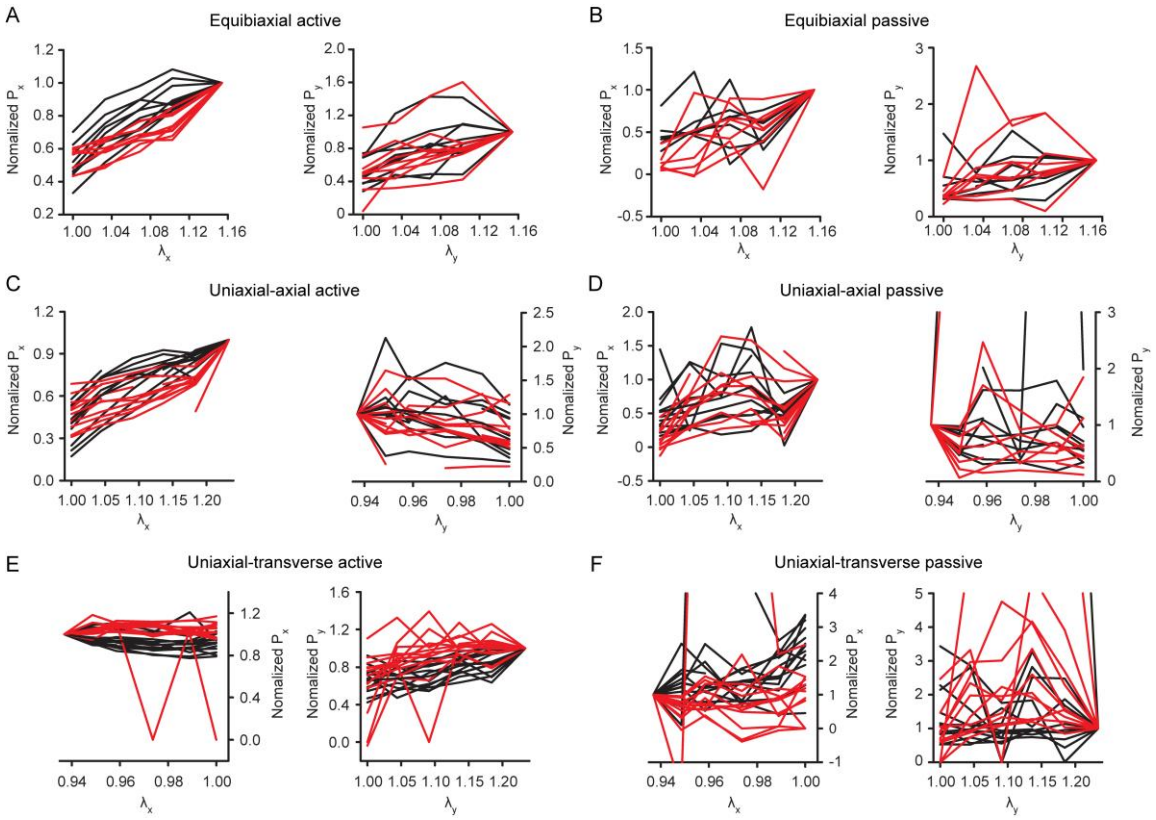

Supplemental figure 4.1. Normalized individual cell stresses for AR4 cell

(A) Axial and transverse active stresses during equibiaxial stretch. (B) Axial and transverse passive stresses during equibiaxial stretch. (C) Axial and transverse active stresses during uniaxial-axial stretch. (D) Axial and transverse passive stresses during uniaxial-axial stretch. (E) Axial and transverse active stresses during uniaxial-transverse stretch. (F) Axial and transverse passive stresses during uniaxial-transverse stretch. All stresses normalized to the value at maximal loading strain. (A-F) Black: loading stresses. Red: unloading stresses.

Table 4.1. QLV model parameter values

Parameter	Value
μ	1.5 kPa
C_f	2.25 kPa
λ_{a0}	0.61
α	0.875
β	0.125

Table 4.2. Hill-type active fiber model parameter values

Parameter	Value
μ	1.25 kPa
C_f	4 kPa
λ_{a0}	0.68
a_0	4 kPa
b	0.001

References

1. Wallace, R., J. Karis, S. Partovi, and D. Fiorella. 2007. Noninvasive imaging of treated cerebral aneurysms, Part I: MR angiographic follow-up of coiled aneurysms. American Journal of Neuroradiology 28:1001-1008.
2. Wallace, R., J. Karis, S. Partovi, and D. Fiorella. 2007. Noninvasive imaging of treated cerebral aneurysms, Part II: CT angiographic follow-up of surgically clipped aneurysms. American Journal of Neuroradiology 28:1207-1212.
3. Kim, H., I. Vignon-Clementel, J. Coogan, C. Figueroa, K. Jansen, and C. Taylor. 2010. Patient-Specific Modeling of Blood Flow and Pressure in Human Coronary Arteries. Annals of Biomedical Engineering 38:3195-3209.
4. Torii, R., M. Oshima, T. Kobayashi, K. Takagi, and T. Tezduyar. 2008. Fluid-structure interaction modeling of a patient-specific cerebral aneurysm: influence of structural modeling. Computational Mechanics 43:151-159.
5. Taylor, C. A., and C. A. Figueroa. 2009. Patient-Specific Modeling of Cardiovascular Mechanics. Annu Rev Biomed Eng 11:109-134.
6. Alford, P., and L. Taber. 2008. Computational study of growth and remodelling in the aortic arch. Computer Methods in Biomechanics and Biomedical Engineering 11:525-538.
7. Alford, P., J. Humphrey, and L. Taber. 2008. Growth and remodeling in a thick-walled artery model: effects of spatial variations in wall constituents. Biomechanics and Modeling in Mechanobiology 7:245-262.
8. Gosline, J., M. Lillie, E. Carrington, P. Guerette, C. Ortlepp, and K. Savage. 2002. Elastic proteins: biological roles and mechanical properties. Philos Trans R Soc Lond B Biol Sci 357:121-132.
9. Fratzl, P., K. Misof, I. Zizak, G. Rapp, H. Amenitsch, and S. Bernstorff. 1998. Fibrillar structure and mechanical properties of collagen. J Struct Biol 122:119-122.
10. Ruiz, S. A., and C. S. Chen. 2007. Microcontact printing: A tool to pattern. Soft Matter 3:168-177.
11. Alford, P. W., A. P. Nesmith, J. N. Seywerd, A. Grosberg, and K. K. Parker. 2011. Vascular smooth muscle contractility depends on cell shape. Integrative Biology 3:1063-1070.
12. Williams, C., X. Q. Brown, E. Bartolak-Suki, H. Ma, A. Chilkoti, and J. Y. Wong. 2011. The use of micropatterning to control smooth muscle myosin heavy chain expression and limit the response to transforming growth factor beta1 in vascular smooth muscle cells. Biomaterials 32:410-418.
13. McCain, M. L., H. Lee, Y. Aratyn-Schaus, A. G. Kleber, and K. K. Parker. 2012. Cooperative coupling of cell-matrix and cell-cell adhesions in cardiac muscle. Proc Natl Acad Sci U S A 109:9881-9886.
14. Rhodon, J. A. G. 1980. Architecture of the Vessel Wall. American Physiological Society.
15. Ingber, D. E. 2006. Cellular mechanotransduction: putting all the pieces together again.
16. Chen, C., M. Mrksich, S. Huang, G. Whitesides, and D. Ingber. 1997. Geometric control of cell life and death. Science 276:1425-1428.
17. Parker, K. K., A. L. Brock, C. Brangwynne, R. J. Mannix, N. Wang, E. Ostuni, N. A. Geisse, J. C. Adams, G. M. Whitesides, and D. E. Ingber. 2002. Directional control of lamellipodia extension by constraining cell shape and orienting cell tractional forces. Faseb j 16:1195-1204.

18. Bray, M.-A., S. P. Sheehy, and K. K. Parker. 2008. Sarcomere alignment is regulated by myocyte shape. Cell Motility and the Cytoskeleton 65:641-651.
19. Alberts, B., A. Johnson, J. Lewis, M. Raff, K. Roberts, and P. Walter. 2002. Molecular Biology of the Cell. Garland Science.
20. Hochmuth, R. 2000. Micropipette aspiration of living cells. Journal of Biomechanics 33:15-22.
21. Kasza, K. E., D. Vader, S. Köster, N. Wang, and D. A. Weitz. 2011. Magnetic Twisting Cytometry. Cold Spring Harbor Protocols.
22. Wang, N., J. P. Butler, and D. E. Ingber. 1993. Mechanotransduction across the cell surface and through the cytoskeleton. Science 260:1124-1127.
23. Li, Q., G. Lee, C. Ong, and C. Lim. 2008. AFM indentation study of breast cancer cells. Biochemical and Biophysical Research Communications 374:609-613.
24. Sen, S., S. Subramanian, and D. Discher. 2005. Indentation and adhesive probing of a cell membrane with AFM: Theoretical model and experiments. Biophysical Journal 89:3203-3213.
25. Evans, E. A. 1983. Bending elastic modulus of red blood cell membrane derived from buckling instability in micropipet aspiration tests. Biophys J 43:27-30.
26. Bao, G., and S. Suresh. 2003. Cell and molecular mechanics of biological materials. Nature Materials 2:715-725.
27. Jimenez-Garcia, L. F., and R. Fragoso-Soriano. 2000. Atomic force microscopy of the cell nucleus. J Struct Biol 129:218-222.
28. Park, S., D. Koch, R. Cardenas, J. Kas, and C. K. Shih. 2005. Cell Motility and Local Viscoelasticity of Fibroblasts. Biophys J 89:4330-4342.
29. Sacks, M. S. 2013. Biaxial Mechanical Evaluation of Planar Biological Materials. Journal of elasticity and the physical science of solids 61:199-246.
30. Waldman, S. D., and J. M. Lee. 2002. Boundary conditions during biaxial testing of planar connective tissues. Part 1: Dynamic Behavior. Journal of Materials Science: Materials in Medicine 13:933-938.
31. Hersen, P., and B. Ladoux. 2011. Biophysics: Push it, pull it. Nature 470:340-341.
32. Harris, A., P. Wild, and D. Stopak. 1980. Silicone rubber substrata: a new wrinkle in the study of cell locomotion.
33. Dembo, M., and Y. L. Wang. 1999. Stresses at the cell-to-substrate interface during locomotion of fibroblasts. Biophys J 76:2307-2316.
34. Munevar, S., Y. Wang, and M. Dembo. 2001. Traction force microscopy of migrating normal and H-ras transformed 3T3 fibroblasts. Biophys J 80:1744-1757.
35. Shiu, Y. T., S. Li, W. A. Marganski, S. Usami, M. A. Schwartz, Y. L. Wang, M. Dembo, and S. Chien. 2004. Rho mediates the shear-enhancement of endothelial cell migration and traction force generation. Biophys J 86:2558-2565.
36. Win, Z., G. D. Vrla, K. E. Steucke, E. N. Sevcik, E. S. Hald, and P. W. Alford. 2014. Smooth muscle architecture within cell-dense vascular tissues influences functional contractility. Integr Biol (Camb) 6:1201-1210.
37. Furchgott, R. F., and J. V. Zawadzki. 1980. The obligatory role of endothelial cells in the relaxation of arterial smooth muscle by acetylcholine. Nature 288:373-376.
38. Peterson, L. H., R. E. Jensen, and J. Parnell. 1960. Mechanical Properties of Arteries in Vivo. Circulation Research 8:622-639.
39. Ushiwata, I., and T. Ushiki. 1990. Cytoarchitecture of the smooth muscles and pericytes of rat cerebral blood vessels. A scanning electron microscopic study. Journal of Neurosurgery 73:82-90.

40. Meng, H., Z. Wang, Y. Hoi, L. Gao, E. Metaxa, D. D. Swartz, and J. Kolega. 2007. Complex hemodynamics at the apex of an arterial bifurcation induces vascular remodeling resembling cerebral aneurysm initiation. Stroke 38:1924-1931.
41. Foutrakis, G. N., H. Yonas, and R. J. Sclabassi. 1999. Saccular aneurysm formation in curved and bifurcating arteries. American Journal of Neuroradiology 20:1309-1317.
42. Krex, D., H. K. Schackert, and G. Schackert. 2001. Genesis of cerebral aneurysms--an update. Acta Neurochirurgica 143:429-448.
43. Lacolley, P., V. Regnault, A. Nicoletti, Z. Li, and J.-B. Michel. 2012. The vascular smooth muscle cell in arterial pathology: a cell that can take on multiple roles. Cardiovascular Research 95:194-204.
44. Rzucidlo, E. M., K. A. Martin, and R. J. Powell. 2007. Regulation of vascular smooth muscle cell differentiation. Journal of Vascular Surgery 45:A25–A32.
45. Rensen, S. S. M., P. A. F. M. Doevendans, and G. J. J. M. v. Eys. 2007. Regulation and characteristics of vascular smooth muscle cell phenotypic diversity. Netherlands Heart Journal 15:100-108.
46. Alford, P., B. Dabiri, J. Goss, M. Hemphill, M. Brigham, and K. Parker. 2011. Blast-induced phenotypic switching in cerebral vasospasm. Proceedings of the National Academy of Sciences 108:12705-12710.
47. Worth, N. F., B. E. Rolfe, J. Song, and G. R. Campbell. 2001. Vascular smooth muscle cell phenotypic modulation in culture is associated with reorganisation of contractile and cytoskeletal proteins. Cell Motility and the Cytoskeleton 49:130-145.
48. McWhorter, F. Y., T. Wang, P. Nguyen, T. Chung, and W. F. Liu. 2013. Modulation of macrophage phenotype by cell shape. Proceedings of the National Academy of Sciences 110:17253-17258.
49. Wolinsky, H., and S. Glagov. 1967. A Lamellar Unit of Aortic Medial Structure and Function in Mammals. Circulation Research 20:99-111.
50. Clark, J. M., and S. Glagov. 1985. Transmural organization of the arterial media. The lamellar unit revisited. Arteriosclerosis, Thrombosis and Vascular Biololgy 5:19-34.
51. Cao, Y., Y. F. Poon, J. Fung, S. Rayatpisheh, V. Chan, and M. B. Chan-Park. 2010. Regulating orientation and phenotype of primary vascular smooth muscle cells by biodegradable films patterned with arrays of microchannels and discontinuous microwalls. Biomaterials 31:6228-6238.
52. Williams, C., X. Q. Brown, E. Bartolak-Suki, H. Ma, A. Chilkoti, and J. Y. Wong. 2011. The use of micropatterning to control smooth muscle myosin heavy chain expression and limit the response to transforming growth factor ?1 in vascular smooth muscle cells. Biomaterials 32:410-418.
53. Meyle, J., K. Gultig, and W. Nisch. 1995. Variation in contact guidance by human cells on a microstructured surface. Journal of Biomedical Materials Research 29:81-88.
54. Teixeira, A. I., G. A. Abrams, P. J. Bertics, C. J. Murphy, and P. F. Nealey. 2003. Epithelial contact guidance on well-defined micro- and nanostructured substrates. Journal of Cell Science 116:1881-1892.
55. Braber, E. T. d., J. E. d. Ruijter, L. A. Ginsel, A. F. v. Recum, and J. A. Jansen. 1996. Quantitative analysis of fibroblast morphology on microgrooved surfaces with various groove and ridge dimensions. Biomaterials 17:2037-2044.
56. Hui, E. E., and S. N. Bhatia. 2007. Micromechanical control of cell–cell interactions. Proceedings of the National Academy of Sciences 104:5722-5726.

57. Hoehme, S., M. Brulport, A. Bauer, E. Bedawy, W. Schormann, M. Hermes, V. Puppe, R. Gebhardt, S. Zellmer, M. Schwarz, E. Bockamp, T. Timmel, J. G. Hengstler, and D. Drasdo. 2010. Prediction and validation of cell alignment along microvessels as order principle to restore tissue architecture in liver regeneration. Proceedings of the National Academy of Sciences 107:10371-10376.
58. Jian Tang, R. P., Jiandong Ding. 2010. The regulation of stem cell differentiation by cell-cell contact on micropatterned material surfaces. Biomaterials 31:2470–2476.
59. Wang, Y., P. Shah, C. Phillips, C. E. Sims, and N. L. Allbritton. 2012. Trapping cells on a stretchable microwell array for single-cell analysis. Analytical and Bioanalytical Chemistry 402:1065-1072.
60. Edd, J. F., D. D. Carlo, K. J. Humphry, S. Koster, D. Irimia, D. A. Weitz, and M. Toner. 2008. Controlled encapsulation of single-cells into monodisperse picolitre drops. Lab on a Chip:1262-1264.
61. Carlo, D. D., L. Y. Wu, and L. P. Lee. 2006. Dynamic single cell culture array. Lab on a Chip 6:1445-1449.
62. Lin, L., Y.-S. Chu, J. P. Thiery, C. T. Lim, and I. Rodriguez. 2013. Microfluidic cell trap array for controlled positioning of single cells on adhesive micropatterns. Lab on a Chip 13:714-721.
63. Lecault, V., M. VanInsberghe, S. Sekulovic, D. J. H. F. Knapp, S. Wohrer, W. Bowden, F. Viel, T. McLaughlin, A. Jarandehei, M. Miller, D. Falconnet, A. K. White, D. G. Kent, M. R. Copley, F. Taghipour, C. J. Eaves, R. K. Humphries, J. M. Piret, and C. L. Hansen. 2011. High-throughput analysis of single hematopoietic stem cell proliferation in microfluidic cell culture arrays. Nature Methods 8:581-586.
64. Skelley, A. M., O. Kirak, H. Suh, R. Jaenisch, and J. Voldman. 2009. Microfluidic control of cell pairing and fusion. Nature Methods 6:147-152.
65. Wu, M., M. Piccini, C.-Y. Koh, K. S. Lam, and A. K. Singh. 2013. Single cell microRNA analysis using microfluidic flow cytometry. PLoS One 8:e55044.
66. Cooksey, G. A., J. T. Elliott, and A. L. Plant. 2011. Reproducibility and Robustness of a Real-Time Microfluidic Cell Toxicity Assay. Analytical Chemistry 83:3890-3896.
67. Hosokawa, M., T. Hayashi, T. Mori, T. Yoshino, S. Nakasono, and T. Matsunaga. 2011. Microfluidic Device with Chemical Gradient for Single-Cell Cytotoxicity Assays. Analytical Chemistry 83:3648-3654
68. Ye, G. J. C., Y. Aratyn-Schaus, A. P. Nesmith, F. S. Pasqualini, P. W. Alford, and K. K. Parker. 2014. The contractile strength of vascular smooth muscle myocytes is shape dependent. Integrative Biology 6:152-163.
69. Bray, M.-A. P., W. J. Adams, N. A. Geisse, A. W. Feinberg, S. P. Sheehy, and K. K. Parker. 2010. Nuclear morphology and deformation in engineered cardiac myocytes and tissues. Biomaterials 31:5143-5150.
70. Thyberg, J., U. Hedin, M. Sjolund, L. Palmberg, and B. A. Bottger. 1990. Regulation of differentiated properties and proliferation of arterial smooth muscle cells. Arteriosclerosis, Thrombosis, and Vascular Biology 10:966-990.
71. Gospodarowicz, D., K. Hirabayashi, L. Giguere, and J. P. Tauber. 1981. Factors controlling the proliferative rate, final cell density, and life span of bovine vascular smooth muscle cells in culture. Journal of Cell Biology 89:568-578.
72. Mrksich, M., C. S. Chen, Y. Xia, L. E. Dike, D. E. Ingber, and G. M. Whitesides. 1996. Controlling cell attachment on contoured surfaces with self-assembled

monolayers of alkanethiolates on gold. Proceedings of the National Academy of Sciences 93:10775-10778.
73. Brunette, D. M. 1986. Fibroblasts on micromachined substrata orient hierarchically to grooves of different dimensions. Experimental Cell Research 164:11-26.
74. Nikkhah, M., F. Edalat, S. Manoucheri, and A. Khademhosseini. 2012. Engineering microscale topographies to control the cell-substrate interface. Biomaterials 33:5230-5246.
75. Han, M., J.-K. Wen, B. Zheng, Y. Cheng, and C. Zhang. 2006. Serum deprivation results in redifferentiation of human umbilical vascular smooth muscle cells. Cell Physiology 291:C50-C58.
76. Nelson, C. M., and C. S. Chen. 2002. Cell-cell signaling by direct contact increases cell proliferation via a PI3K-dependent signal. FEBS Letters 514:238-242.
77. Liu, S. Q., and Y. C. Fung. 1988. Zero-Stress States of Arteries. Journal of Biomechanical Engineering 110:82-84.
78. Cox, R. H. 1978. Passive mechanics and connective tissue composition of canine arteries. American Journal opf Physiology 234:H533-541.
79. Aoki, T., H. Kataoka, M. Morimoto, K. Nozaki, and N. Hashimoto. 2007. Macrophage-derived matrix metalloproteinase-2 and -9 promote the progression of cerebral aneurysms in rats. Stroke 38:162-169.
80. Zempo, N., N. Koyama, R. D. Kenagy, H. J. Lea, and A. W. Clowes. 1996. Regulation of vascular smooth muscle cell migration and proliferation in vitro and in injured rat arteries by a synthetic matrix metalloproteinase inhibitor. Arteriosclerosis, Thrombosis, and Vascular Biology 16:28-33.
81. Stegemann, J. P., and R. M. Nerem. 2003. Phenotype Modulation in Vascular Tissue Engineering Using Biochemical. Annals of Biomedical Engineering 31:391-402.
82. Gott, M., M. Ast, L. B. Lane, J. A. Schwartz, A. Catanzano, P. Razzano, and D. A. Grande. 2011. Tendon phenotype should dictate tissue engineering modality in tendon repair: a review. Discovery Medicine 12:75-84.
83. Kim, B.-S., J. Nikolovski, J. Bonadio, and D. J. M. Elizabeth Smiley. 1999. Engineered Smooth Muscle Tissues: Regulating Cell Phenotype with the Scaffold. Experimental Cell Research 251:318–328.
84. Alford, P. W., A. P. Nesmith, J. N. Seywerd, A. Grosberg, and K. K. Parker. 2011. Vascular smooth muscle contractility depends on cell shape. Integr Biol (Camb) 3:1063-1070.
85. Isenberg, B. C., C. Williams, and R. T. Tranquillo. 2006. Small-Diameter Artificial Arteries Engineered In Vitro. Circulation Research 98:25-35.
86. Edelman, E. R. 1999. Vascular Tissue Engineering. Circulation Research 85.
87. Niklason, L. E., J. Gao, W. M. Abbott, K. K. Hirschi, S. Houser, R. Marini, and R. Langer. 1999. Functional Arteries Grown in Vitro. Science 284:489-493.
88. Norotte, C., F. S. Marga, L. E. Niklason, and G. Forgacs. 2009. Scaffold-free vascular tissue engineering using bioprinting. Biomaterials 30:5910–5917.
89. Ratcliffe, A. 2000. Tissue engineering of vascular grafts. Matrix Biology 19:353–357.
90. Nerem, R. M. 2006. Tissue Engineering of Blood Vessels. John Wiley & Sons, Inc.
91. Schmidt, C. E., and J. M. Baier. 2000. Acellular vascular tissues: natural biomaterials for tissue repair and tissue engineering. Biomaterials 21:2215–2231.

92. Teebken, O. E., A. Bader, G. Steinhoff, and A. Haverich. 2000. Tissue Engineering of Vascular Grafts: Human Cell Seeding of Decellularised Porcine Matrix. European Journal of Vascular and Endovascular Surgery 19:381–386.
93. Kim, B.-S., J. Nikolovski, J. Bonadio, and D. J. Mooney. 1999. Cyclic mechanical strain regulates the development of engineered smooth muscle tissue. Nature Biotechnology 17:979-983.
94. Jeong, S. I., J. H. Kwon, J. I. Lim, S.-W. Cho, Y. Jung, W. J. Sung, S. H. Kim, Y. H. Kim, Y. M. Lee, B.-S. Kim, C. y. Choi, and S.-J. Kim. 2005. Mechano-active tissue engineering of vascular smooth muscle using pulsatile perfusion bioreactors and elastic PLCL scaffolds. Biomaterials 26:1405–1411.
95. Xia, Y., and G. M. Whitesides. 2003. Soft Lithography. Angewandte Chemie 37:550-575.
96. Feinberg, A. W., P. W. Alford, H. Jin, C. M. Ripplinger, A. A. Werdich, S. P. Sheehy, A. Grosberg, and K. K. Parker. 2012. Controlling the contractile strength of engineered cardiac muscle by hierarchal tissue architecture. Biomaterials 33:5732-5741.
97. Grosberg, A., P. W. Alford, M. L. McCain, and K. K. Parker. 2011. Ensembles of engineered cardiac tissues for physiological and pharmacological study: heart on a chip. Lab on a Chip 11:4165-4173.
98. Alford, P. W., A. W. Feinberg, S. P. Sheehy, and K. K. Parker. 2010. Biohybrid thin films for measuring contractility in engineered cardiovascular muscle. Biomaterials 31:3613-3621.
99. Engler, A. J., S. Sen, H. L. Sweeney, and D. E. Discher. 2006. Matrix Elasticity Directs Stem Cell Lineage Specification. Cell 126:677-689.
100. Trepat, X., M. R. Wasserman, T. E. Angelini, E. Millet, D. A. Weitz, J. P. Butler, and J. J. Fredberg. 2009. Physical forces during collective cell migration. Nat Phys 5:426-430.
101. Shyer, A. E., T. Tallinen, N. L. Nerurkar, Z. Y. Wei, E. S. Gil, D. L. Kaplan, C. J. Tabin, and L. Mahadevan. 2013. Villification: How the Gut Gets Its Villi. Science 342:212-218.
102. Humphrey, J. D., J. F. Eberth, W. W. Dye, and R. L. Gleason. 2009. Fundamental role of axial stress in compensatory adaptations by arteries. J Biomech 42:1-8.
103. Alford, P. W., B. E. Dabiri, J. A. Goss, M. A. Hemphill, M. D. Brigham, and K. K. Parker. 2011. Blast-induced phenotypic switching in cerebral vasospasm. Proceedings of the National Academy of Sciences of the United States of America 108:12705-12710.
104. Sacks, M. S., and W. Sun. 2003. Multiaxial mechanical behavior of biological materials. Annual review of biomedical engineering 5:251-284.
105. Humphrey, J. D., R. K. Strumpf, and F. C. Yin. 1990. Determination of a constitutive relation for passive myocardium: I. A new functional form. Journal of biomechanical engineering 112:333-339.
106. Kim, D. H., E. A. Lipke, P. Kim, R. Cheong, S. Thompson, M. Delannoy, K. Y. Suh, L. Tung, and A. Levchenko. 2010. Nanoscale cues regulate the structure and function of macroscopic cardiac tissue constructs. Proceedings of the National Academy of Sciences of the United States of America 107:565-570.
107. Gerdes, A. M., S. E. Kellerman, J. A. Moore, K. E. Muffly, L. C. Clark, P. Y. Reaves, K. B. Malec, P. P. McKeown, and D. D. Schocken. 1992. Structural remodeling of cardiac myocytes in patients with ischemic cardiomyopathy. Circulation 86:426-430.

108. Makhija, E., D. S. Jokhun, and G. V. Shivashankar. 2016. Nuclear deformability and telomere dynamics are regulated by cell geometric constraints. Proceedings of the National Academy of Sciences of the United States of America 113:E32-40.
109. Rothenberg, K. E., S. S. Neibart, A. S. LaCroix, and B. D. Hoffman. 2015. Controlling Cell Geometry Affects the Spatial Distribution of Load Across Vinculin. Cell Mol Bioeng 8:364-382.
110. Versaevel, M., T. Grevesse, and S. Gabriele. 2012. Spatial coordination between cell and nuclear shape within micropatterned endothelial cells. Nat Commun 3.
111. Versaevel, M., J. B. Braquenier, M. Riaz, T. Grevesse, J. Lantoine, and S. Gabriele. 2014. Super-resolution microscopy reveals LINC complex recruitment at nuclear indentation sites. Sci Rep-Uk 4.
112. Wang, N., K. Naruse, D. Stamenovic, J. J. Fredberg, S. M. Mijailovich, I. M. Toric-Norrelykke, T. Polte, R. Mannix, and D. E. Ingber. 2001. Mechanical behavior in living cells consistent with the tensegrity model. Proceedings of the National Academy of Sciences of the United States of America 98:7765-7770.
113. Diez-Silva, M., M. Dao, J. Y. Han, C. T. Lim, and S. Suresh. 2010. Shape and Biomechanical Characteristics of Human Red Blood Cells in Health and Disease. Mrs Bull 35:382-388.
114. Kuznetsova, T. G., M. N. Starodubtseva, N. I. Yegorenkov, S. A. Chizhik, and R. I. Zhdanov. 2007. Atomic force microscopy probing of cell elasticity. Micron 38:824-833.
115. Janmey, P. A., and C. A. McCulloch. 2007. Cell mechanics: integrating cell responses to mechanical stimuli. Annual review of biomedical engineering 9:1-34.
116. Rodriguez, M. L., P. J. McGarry, and N. J. Sniadecki. 2013. Review on Cell Mechanics: Experimental and Modeling Approaches. Appl Mech Rev 65.
117. Taber, L. A. 1995. Biomechanics of Growth, Remodeling, and Morphogenesis. Appl Mech Rev 48:487-545.
118. Taber, L. A. 1998. Biomechanical growth laws for muscle tissue. Journal of theoretical biology 193:201-213.
119. Malkawi, A. H., R. J. Hinchliffe, Y. Xu, P. J. Holt, I. M. Loftus, and M. M. Thompson. 2010. Patient-specific biomechanical profiling in abdominal aortic aneurysm development and rupture. Journal of vascular surgery 52:480-488.
120. Doyle, B. J., A. J. Cloonan, M. T. Walsh, D. A. Vorp, and T. M. McGloughlin. 2010. Identification of rupture locations in patient-specific abdominal aortic aneurysms using experimental and computational techniques. J Biomech 43:1408-1416.
121. Humphrey, J. D., and K. R. Rajagopal. 2003. A constrained mixture model for arterial adaptations to a sustained step change in blood flow. Biomechanics and modeling in mechanobiology 2:109-126.
122. Gleason, R. L., and J. D. Humphrey. 2004. A mixture model of arterial growth and remodeling in hypertension: Altered muscle tone and tissue turnover. Journal of Vascular Research 41:352-363.
123. Wagenseil, J. E. 2011. A constrained mixture model for developing mouse aorta. Biomechanics and modeling in mechanobiology 10:671-687.
124. Alford, P. W., J. D. Humphrey, and L. A. Taber. 2008. Growth and remodeling in a thick-walled artery model: effects of spatial variations in wall constituents. Biomechanics and modeling in mechanobiology 7:245-262.

125. Soares, J. S., and M. S. Sacks. 2016. A triphasic constrained mixture model of engineered tissue formation under in vitro dynamic mechanical conditioning. Biomechanics and modeling in mechanobiology 15:293-316.
126. Sander, E. A., T. Stylianopoulos, R. T. Tranquillo, and V. H. Barocas. 2009. Image-based multiscale modeling predicts tissue-level and network-level fiber reorganization in stretched cell-compacted collagen gels. Proceedings of the National Academy of Sciences of the United States of America 106:17675-17680.
127. Shah, S. B., C. Witzenburg, M. F. Hadi, H. P. Wagner, J. M. Goodrich, P. W. Alford, and V. H. Barocas. 2014. Prefailure and Failure Mechanics of the Porcine Ascending Thoracic Aorta: Experiments and a Multiscale Model. J Biomech Eng-T Asme 136.
128. Edgar, L. T., S. A. Maas, J. E. Guilkey, and J. A. Weiss. 2015. A coupled model of neovessel growth and matrix mechanics describes and predicts angiogenesis in vitro. Biomechanics and modeling in mechanobiology 14:767-782.
129. Taber, L. A. 2004. Nonlinear Theory of Elasticity: Applications in Biomechancis. World Scientific Publishing, Singapore.
130. Butler, J. P., I. M. Tolic-Norrelykke, B. Fabry, and J. J. Fredberg. 2002. Traction fields, moments, and strain energy that cells exert on their surroundings. American journal of physiology. Cell physiology 282:C595-605.
131. Simmons, C. S., A. J. Ribeiro, and B. L. Pruitt. 2013. Formation of composite polyacrylamide and silicone substrates for independent control of stiffness and strain. Lab on a chip 13:646-649.
132. Polio, S. R., K. E. Rothenberg, D. Stamenovic, and M. L. Smith. 2012. A micropatterning and image processing approach to simplify measurement of cellular traction forces. Acta biomaterialia 8:82-88.
133. Vande Geest, J. P., M. S. Sacks, and D. A. Vorp. 2006. The effects of aneurysm on the biaxial mechanical behavior of human abdominal aorta. J Biomech 39:1324-1334.
134. Kaunas, R., and H. J. Hsu. 2009. A kinematic model of stretch-induced stress fiber turnover and reorientation. Journal of theoretical biology 257:320-330.
135. Ye, G. J. C., Y. Aratyn-Schaus, A. P. Nesmith, F. S. Pasqualini, P. W. Alford, and K. K. Parker. 2014. The contractile strength of vascular smooth muscle myocytes is shape dependent. Integrative Biology 6:152-163.
136. Han, M., J.-K. Wen, B. Zheng, Y. Cheng, and C. Zhang. 2006. Serum deprivation results in redifferentiation of human umbilical vascular smooth muscle cells. American journal of physiology. Cell physiology 291:C50-58.
137. Ingber, D. E., D. Prusty, Z. Q. Sun, H. Betensky, and N. Wang. 1995. Cell shape, cytoskeletal mechanics, and cell cycle control in angiogenesis. Journal of Biomechanics 28:1471-1484.
138. Luxton, G. W., J. I. Lee, S. Haverlock-Moyns, J. M. Schober, and G. A. Smith. 2006. The pseudorabies virus VP1/2 tegument protein is required for intracellular capsid transport. Journal of virology 80:201-209.
139. Fletcher, D. A., and R. D. Mullins. 2010. Cell mechanics and the cytoskeleton. Nature 463:485-492.
140. Tseng, Q., E. Duchemin-Pelletier, A. Deshiere, M. Balland, H. Guillou, O. Filhol, and M. Thery. 2012. Spatial organization of the extracellular matrix regulates cell-cell junction positioning. Proceedings of the National Academy of Sciences of the United States of America 109:1506-1511.

141. Gasser, T. C., R. W. Ogden, and G. A. Holzapfel. 2006. Hyperelastic modelling of arterial layers with distributed collagen fibre orientations. Journal of the Royal Society, Interface / the Royal Society 3:15-35.
142. Steucke, K. E., P. V. Tracy, E. S. Hald, J. L. Hall, and P. W. Alford. 2015. Vascular smooth muscle cell functional contractility depends on extracellular mechanical properties. J Biomech 48:3044-3051.
143. Palchesko, R. N., L. Zhang, Y. Sun, and A. W. Feinberg. 2012. Development of polydimethylsiloxane substrates with tunable elastic modulus to study cell mechanobiology in muscle and nerve. PloS one 7:e51499.
144. Puig-de-Morales-Marinkovic, M., K. T. Turner, J. P. Butler, J. J. Fredberg, and S. Suresh. 2007. Viscoelasticity of the human red blood cell. American Journal of Physiology - Cell Physiology 293:C597-C605.
145. Bausch, A. R., F. Ziemann, A. A. Boulbitch, K. Jacobson, and E. Sackmann. 1998. Local measurements of viscoelastic parameters of adherent cell surfaces by magnetic bead microrheometry. Biophys J 75:2038-2049.
146. Bausch, A. R., W. Moller, and E. Sackmann. 1999. Measurement of local viscoelasticity and forces in living cells by magnetic tweezers. Biophys J 76:573-579.
147. Putman, C. A., K. O. van der Werf, B. G. de Grooth, N. F. van Hulst, and J. Greve. 1994. Viscoelasticity of living cells allows high resolution imaging by tapping mode atomic force microscopy. Biophys J 67:1749-1753.
148. Trepat, X., M. Grabulosa, F. Puig, G. N. Maksym, D. Navajas, and R. Farre. 2004. Viscoelasticity of human alveolar epithelial cells subjected to stretch. Am J Physiol Lung Cell Mol Physiol 287:L1025-1034.
149. Trepat, X., L. Deng, S. S. An, D. Navajas, D. J. Tschumperlin, W. T. Gerthoffer, J. P. Butler, and J. J. Fredberg. 2007. Universal physical responses to stretch in the living cell. Nature 447:592-595.
150. Bonakdar, N., R. Gerum, M. Kuhn, M. Sporrer, A. Lippert, W. Schneider, K. E. Aifantis, and B. Fabry. 2016. Mechanical plasticity of cells. Nat Mater 15:1090-1094.
151. Weng, S., Y. Shao, W. Chen, and J. Fu. 2016. Mechanosensitive subcellular rheostasis drives emergent single-cell mechanical homeostasis. Nat Mater 15:961-967.
152. Hu, S., L. Eberhard, J. Chen, J. C. Love, J. P. Butler, J. J. Fredberg, G. M. Whitesides, and N. Wang. 2004. Mechanical anisotropy of adherent cells probed by a three-dimensional magnetic twisting device. American journal of physiology. Cell physiology 287:C1184-1191.
153. Schievink, W. I. 1997. Intracranial aneurysms. N Engl J Med 336:28-40.
154. Radmacher, M., R. W. Tillmann, M. Fritz, and H. E. Gaub. 1992. From Molecules to Cells - Imaging Soft Samples with the Atomic Force Microscope. Science 257:1900-1905.
155. Schmidschonbein, G. W., K. L. P. Sung, H. Tozeren, R. Skalak, and S. Chien. 1981. Passive Mechanical-Properties of Human-Leukocytes. Biophys J 36:243-256.
156. Wang, N., and D. E. Ingber. 1995. Probing transmembrane mechanical coupling and cytomechanics using magnetic twisting cytometry. Biochem Cell Biol 73:327-335.
157. Qiu, H., Y. Zhu, Z. Sun, J. P. Trzeciakowski, M. Gansner, C. Depre, R. R. Resuello, F. F. Natividad, W. C. Hunter, G. M. Genin, E. L. Elson, D. E. Vatner, G. A. Meininger, and S. F. Vatner. 2010. Short communication: vascular smooth

muscle cell stiffness as a mechanism for increased aortic stiffness with aging. Circ Res 107:615-619.
158. Matsumoto, T., and K. Hayashi. 1996. Stress and strain distribution in hypertensive and normotensive rat aorta considering residual strain. Journal of biomechanical engineering 118:62-73.
159. Zhou, J., and Y. C. Fung. 1997. The degree of nonlinearity and anisotropy of blood vessel elasticity. Proceedings of the National Academy of Sciences of the United States of America 94:14255-14260.
160. Bell, V., W. A. Mitchell, S. Sigurethsson, J. J. Westenberg, J. D. Gotal, A. A. Torjesen, T. Aspelund, L. J. Launer, A. de Roos, V. Gudnason, T. B. Harris, and G. F. Mitchell. 2014. Longitudinal and circumferential strain of the proximal aorta. Journal of the American Heart Association 3:e001536.
161. Bonifasi-Lista, C., S. P. Lake, M. S. Small, and J. A. Weiss. 2005. Viscoelastic properties of the human medial collateral ligament under longitudinal, transverse and shear loading. J Orthop Res 23:67-76.
162. Lai, V. K., M. F. Hadi, R. T. Tranquillo, and V. H. Barocas. 2013. A Multiscale Approach to Modeling the Passive Mechanical Contribution of Cells in Tissues. J Biomech Eng-T Asme 135.
163. Kollmannsberger, P., and B. Fabry. 2011. Linear and Nonlinear Rheology of Living Cells. Annu Rev Mater Res 41:75-97.
164. Caille, N., O. Thoumine, Y. Tardy, and J. J. Meister. 2002. Contribution of the nucleus to the mechanical properties of endothelial cells. Journal of Biomechanics 35:177-187.
165. Isermann, P., and J. Lammerding. 2013. Nuclear Mechanics and Mechanotransduction in Health and Disease. Curr Biol 23:R1113-R1121.
166. Maskarinec, S. A., C. Franck, D. A. Tirrell, and G. Ravichandran. 2009. Quantifying cellular traction forces in three dimensions. Proceedings of the National Academy of Sciences of the United States of America 106:22108-22113.
167. Legant, W. R., C. K. Choi, J. S. Miller, L. Shao, L. Gao, E. Betzig, and C. S. Chen. 2013. Multidimensional traction force microscopy reveals out-of-plane rotational moments about focal adhesions. Proceedings of the National Academy of Sciences of the United States of America 110:881-886.
168. Harris, A. R., L. Peter, J. Bellis, B. Baum, A. J. Kabla, and G. T. Charras. 2012. Characterizing the mechanics of cultured cell monolayers. Proceedings of the National Academy of Sciences of the United States of America 109:16449-16454.
169. Tong, P., and Y. C. Fung. 1976. The stress-strain relationship for the skin. J Biomech 9:649-657.
170. Choi, H. S., and R. P. Vito. 1990. Two-dimensional stress-strain relationship for canine pericardium. Journal of biomechanical engineering 112:153-159.
171. Billiar, K. L., and M. S. Sacks. 2000. Biaxial mechanical properties of the natural and glutaraldehyde treated aortic valve cusp--Part I: Experimental results. Journal of biomechanical engineering 122:23-30.
172. Fung, Y. C. 1991. What are the residual stresses doing in our blood vessels? Annals of biomedical engineering 19:237-249.
173. Taber, L. A. 1998. A model for aortic growth based on fluid shear and fiber stresses. J Biomech Eng-T Asme 120:348-354.
174. Chan, C. E., and D. J. Odde. 2008. Traction Dynamics of Filopodia on Compliant Substrates. Science 322:1687-1691.

175. Dupont, S., L. Morsut, M. Aragona, E. Enzo, S. Giulitti, M. Cordenonsi, F. Zanconato, J. Le Digabel, M. Forcato, S. Bicciato, N. Elvassore, and S. Piccolo. 2011. Role of YAP/TAZ in mechanotransduction. Nature 474:179-U212.
176. Guilluy, C., L. D. Osborne, L. Van Landeghem, L. Sharek, R. Superfine, R. Garcia-Mata, and K. Burridge. 2014. Isolated nuclei adapt to force and reveal a mechanotransduction pathway in the nucleus. Nat Cell Biol 16:376-+.
177. Williams, B. 1998. Mechanical influences on vascular smooth muscle cell function. J Hypertens 16:1921-1929.
178. Brown, X. Q., E. Bartolak-Suki, C. Williams, M. L. Walker, V. M. Weaver, and J. Y. Wong. 2010. Effect of substrate stiffness and PDGF on the behavior of vascular smooth muscle cells: implications for atherosclerosis. J Cell Physiol 225:115-122.
179. Steucke, K. E., P. V. Tracy, E. S. Hald, J. L. Hall, and P. W. Alford. 2015. Vascular smooth muscle cell functional contractility depends on extracellular mechanical properties. J Biomech 48:3044-3051.
180. Du, J., Y. Zu, J. Li, S. Du, Y. Xu, L. Zhang, L. Jiang, Z. Wang, S. Chien, and C. Yang. 2016. Extracellular matrix stiffness dictates Wnt expression through integrin pathway. In Sci Rep.
181. Alam, S. G., Q. Zhang, N. Prasad, Y. Li, S. Chamala, R. Kuchibhotla, B. Kc, V. Aggarwal, S. Shrestha, A. L. Jones, S. E. Levy, K. J. Roux, J. A. Nickerson, and T. P. Lele. 2016. The mammalian LINC complex regulates genome transcriptional responses to substrate rigidity. In Sci Rep.
182. Yerrapureddy, A., J. Tobias, and S. S. Margulies. 2009. Cyclic Stretch Magnitude and Duration Affect Rat Alveolar Epithelial Gene Expression. In Cell Physiol Biochem. 113-122.
183. Chiu, C. Z., B. W. Wang, and K. G. Shyu. 2013. Effects of cyclic stretch on the molecular regulation of myocardin in rat aortic vascular smooth muscle cells. In J Biomed Sci. 50.
184. Marwick, T. H. 2006. Measurement of strain and strain rate by echocardiography: ready for prime time? J Am Coll Cardiol 47:1313-1327.
185. Havre, R., and O. H. Gilja. 2014. Elastography and strain rate imaging of the gastrointestinal tract. Eur J Radiol 83:438-441.
186. Villablanca, J. P., G. R. Duckwiler, R. Jahan, S. Tateshima, N. A. Martin, J. Frazee, N. R. Gonzalez, J. Sayre, and F. V. Vinuela. 2013. Natural history of asymptomatic unruptured cerebral aneurysms evaluated at CT angiography: growth and rupture incidence and correlation with epidemiologic risk factors. Radiology 269:258-265.
187. Sun, Z., S. S. Guo, and R. Fässler. 2016. Integrin-mediated mechanotransduction.
188. Lombardi, M. L., and J. Lammerding. 2011. Keeping the LINC: the importance of nucleo-cytoskeletal coupling in intracellular force transmission and cellular function. Biochem Soc Trans 39:1729-1734.
189. Spassova, M. A., T. Hewavitharana, W. Xu, J. Soboloff, and D. L. Gill. 2006. A common mechanism underlies stretch activation and receptor activation of TRPC6 channels. Proc Natl Acad Sci U S A 103:16586-16591.
190. Lee, J., A. Ishihara, G. Oxford, B. Johnson, and K. Jacobson. 1999. Regulation of cell movement is mediated by stretch-activated calcium channels. Nature 400:382-386.
191. Naruse, K., and M. Sokabe. 1993. Involvement of stretch-activated ion channels in Ca2+ mobilization to mechanical stretch in endothelial cells. Am J Physiol 264:C1037-1044.

192. Bausch, A. R., W. Möller, and E. Sackmann. 1999. Measurement of local viscoelasticity and forces in living cells by magnetic tweezers. Biophys J 76:573-579.
193. Puig-de-Morales-Marinkovic, M., K. T. Turner, J. P. Butler, J. J. Fredberg, and S. Suresh. 2007. Viscoelasticity of the human red blood cell. Am J Physiol Cell Physiol 293:C597-605.
194. Hecht, F. M., J. Rheinlaender, N. Schierbaum, W. H. Goldmann, B. Fabry, and T. E. Schaffer. 2015. Imaging viscoelastic properties of live cells by AFM: power-law rheology on the nanoscale. Soft Matter 11:4584-4591.
195. Karcher, H., J. Lammerding, H. Huang, R. T. Lee, R. D. Kamm, and M. R. Kaazempur-Mofrad. 2003. A three-dimensional viscoelastic model for cell deformation with experimental verification. Biophys J 85:3336-3349.
196. Puig-De-Morales, M., M. Grabulosa, J. Alcaraz, J. Mullol, G. N. Maksym, J. J. Fredberg, and D. Navajas. 2001. Measurement of cell microrheology by magnetic twisting cytometry with frequency domain demodulation. J Appl Physiol (1985) 91:1152-1159.
197. Win, Z., J. M. Buksa, K. E. Steucke, G. W. Gant Luxton, V. H. Barocas, and P. W. Alford. 2017. Cellular Microbiaxial Stretching to Measure a Single-Cell Strain Energy Density Function. J Biomech Eng 139.
198. Kollmannsberger, P., and B. Fabry. 2011. Linear and Nonlinear Rheology of Living Cells. Annual Review of Mateirals Reserach 41:75-97.
199. Fung, Y. C. 1993. Biomechanics : mechanical properties of living tissues. Springer-Verlag, New York.
200. Canovic, E. P., A. J. Zollinger, S. N. Tam, M. L. Smith, and D. Stamenovic. 2016. Tensional homeostasis in endothelial cells is a multicellular phenomenon. Am J Physiol Cell Physiol 311:C528-535.
201. Weng, S., Y. Shao, W. Chen, and J. Fu. 2016. Mechanosensitive subcellular rheostasis drives emergent single-cell mechanical homeostasis. Nat Mater 15:961-967.
202. Hill, A. V. 1938. The Heat of Shortening and the Dynamic Constants of Muscle. Proceedings of the Royal Society B 126:136-195.
203. Han, M., J. K. Wen, B. Zheng, Y. Cheng, and C. Zhang. 2006. Serum deprivation results in redifferentiation of human umbilical vascular smooth muscle cells. American Journal of Cell Physiology 291:C50-58.
204. Krizmanich, W. J., and R. M. Lee. 1987. Scanning electron microscopy of vascular smooth muscle cells from rat muscular arteries. Scanning Microsc 1:1749-1758.
205. Wan, J., F. He, Y. Zhao, H. Zhang, X. Zhou, and M. Wan. 2014. Non-invasive vascular radial/circumferential strain imaging and wall shear rate estimation using video images of diagnostic ultrasound. Ultrasound Med Biol 40:622-636.
206. Teixeira, R., R. Monteiro, R. Baptista, A. Barbosa, L. Leite, M. Ribeiro, R. Martins, N. Cardim, and L. Goncalves. 2015. Circumferential vascular strain rate to estimate vascular load in aortic stenosis: a speckle tracking echocardiography study. Int J Cardiovasc Imaging 31:681-689.
207. Carew, E. O., J. E. Barber, and I. Vesely. 2000. Role of preconditioning and recovery time in repeated testing of aortic valve tissues: validation through quasilinear viscoelastic theory. Ann Biomed Eng 28:1093-1100.
208. Schatzmann, L., P. Brunner, and H. U. Staubli. 1998. Effect of cyclic preconditioning on the tensile properties of human quadriceps tendons and patellar ligaments. Knee Surg Sports Traumatol Arthrosc 6 Suppl 1:S56-61.

209. Miller, K. S., L. Edelstein, B. K. Connizzo, and L. J. Soslowsky. 2012. Effect of Preconditioning and Stress Relaxation on Local Collagen Fiber Re-Alignment: Inhomogeneous Properties of Rat Supraspinatus Tendon. In J Biomech Eng. 31007-NaN.
210. Guilak, F., J. R. Tedrow, and R. Burgkart. 2000. Viscoelastic properties of the cell nucleus. Biochem Biophys Res Commun 269:781-786.
211. Yamamoto, S., H. Tsutsui, M. Takahashi, Y. Ishibashi, H. Tagawa, K. Imanaka-Yoshida, Y. Saeki, and A. Takeshita. 1998. Role of microtubules in the viscoelastic properties of isolated cardiac muscle. J Mol Cell Cardiol 30:1841-1853.
212. Yi-Chia Lin, Gijsje H. Koenderink, a. Frederick, C. MacKintosh, and David A. Weitz. 2007. Viscoelastic Properties of Microtubule Networks. Macromolecules 40:7714-7720.
213. HUMPHREY, J. D., and K. R. RAJAGOPAL. 2011. A CONSTRAINED MIXTURE MODEL FOR GROWTH AND REMODELING OF SOFT TISSUES. Mathematical Models and Methods in Applied Sciences.
214. Goto, M., and Y. Kimoto. 1966. Hysteresis and stress-relaxation of the blood vessels studied by a universal tensile testing instrument. Jpn J Physiol 16:169-184.
215. Wagenseil, J. E., and R. P. Mecham. 2009. Vascular Extracellular Matrix and Arterial Mechanics. Physiol Rev 89:957-989.
216. Webster, K. D., W. P. Ng, and D. A. Fletcher. 2014. Tensional homeostasis in single fibroblasts. Biophys J 107:146-155.
217. Bonakdar, N., R. Gerum, M. Kuhn, M. Sporrer, A. Lippert, W. Schneider, K. E. Aifantis, and B. Fabry. 2016. Mechanical plasticity of cells. Nat Mater 15:1090-1094.
218. Deshpande, V. S., R. M. McMeeking, and A. G. Evans. 2006. A bio-chemo-mechanical model for cell contractility. In Proc Natl Acad Sci U S A. 14015-14020.